



Figure 1: Copyright–Blayer Pablo

1998 GEMINI SITE TESTING CAMPAIGN

Cerro Pachón and Cerro Tololo

VERNIN Jean, AGABI Abdelkrim, AVILA Remy
AZOUIT Max, CONAN Rodolphe, MARTIN Francis
MASCIADRI Elena, SANCHEZ Leonardo, ZIAD Aziz

January 21, 2000

¹Thanks to Pablo BLAYER and to Bernhard LOPEZ who launched many balloons and help us in many circumstances.

Contents

INTRODUCTION	1
1 INSTRUMENTAL METHODS	3
1.1 Review	3
1.2 Definition of atmospheric slabs	5
1.3 Scidar	6
1.3.1 Principle of the Generalized Scidar (GS)	6
1.3.2 Simultaneous measurement of $C_N^2(h)$ and $\mathbf{V}(h)$ from double star scintillation	7
1.3.3 Simultaneous measurement of $C_N^2(h)$ and $\mathbf{V}(h)$ from single star scintillation	11
1.4 Generalized Seeing Monitor (GSM)	11
1.4.1 GSM instrument	11
1.4.2 Data acquisition and reduction	12
1.5 Instrumented Balloons and Mast	16
1.5.1 Balloon sounding	16
1.5.2 Instrumented meteorological mast	17
2 OBSERVING CAMPAIGN	18
2.1 Geographical installation	18
2.2 Time schedule	18
3 INDIVIDUAL RESULTS	21
3.1 G-Scidar	21
3.1.1 Nightly observation	22
3.1.2 Statistics over each one-week run	33
3.1.3 All run statistics	50
3.2 GSM	54
3.2.1 Data Analysis	54
3.2.2 Night-by-night results	54
3.3 Balloon	56
3.3.1 Nightly observation	60
3.3.2 Statistics over each one-week run	61
3.3.3 All year statistics	66
3.4 Mast	67
3.4.1 Nightly observations	67

4	DISCUSSION	71
4.1	G–Scidar results	71
4.2	G–Scidar/Balloon for $C_N^2(h)$ profiles	74
4.2.1	Detailed Run 1. January 98	74
4.2.2	Detailed run 2. April 98	79
4.2.3	Detailed run 3. July 98	81
4.2.4	Detailed run 4. October 98	84
4.2.5	Summary of each run and whole year	88
4.3	G–Scidar/Balloon integrated parameters: θ, τ	93
4.4	G–Scidar/GSM/Balloon comparison during last run, October 1998 . .	95
5	CONCLUSION	97
5.1	Instruments: methods, coherence, reliability	97
5.2	Scientific conclusions	98
5.3	Acknowledgments	101
6	BIBLIOGRAPHY	102
7	ANNEX	104
7.1	SCIDAR	104
7.1.1	RUN 1	104
7.1.2	RUN 2	131
7.1.3	RUN 3	139
7.1.4	RUN 4	162
7.2	BALLOONS	192
7.3	GSM	245
7.3.1	Night of 03/04 October 1998	245
7.3.2	Night of 04/05 October 1998	246
7.3.3	Night of 05/06 October 1998	247
7.3.4	Night of 06/07 October 1998	248
7.3.5	Night of 07/08 October 1998	249
7.3.6	Night of 08/09 October 1998	250
7.3.7	Night of 09/10 October 1998	251

INTRODUCTION

In 1998, a site testing campaign took place at Cerro Tololo and Cerro Pachón in the framework of the Gemini program to implement Adaptive Optics (AO) at the focus of their large 8.1m telescope. This site testing campaign was performed by the Département d'Astrophysique of the Nice–Sophia Antipolis University, under the responsibility of Jean Vernin, after being elected from a Request to Proposal issued by Gemini organization.

In order to optimize the design of AO instrumentation, the knowledge of atmospheric parameters, such as vertical profiles of optical turbulence, wind speed and outer scale, are needed. Now, few instruments have been developed to fulfill the requirements of measuring quantitatively those parameters: Generalized Scidar, instrumented balloons, Grating Scale Monitor, Differential Image Motion Monitor, Scintillometers, instrumented mast, which are generally cumbersome to manage. In the past many short campaigns, lasting only few weeks, have shown that those techniques are now reliable, and give new insight on the behaviour of the optical turbulence. As will be explained later, one is now not only able to know the relative contribution of each slab of the atmosphere, i.e the surface layer, the boundary layer, the troposphere and the stratosphere, but also the contribution of the dome and mirror seeing to astronomical image degradation.

For the first time, such a knowledge has been extended over a whole year, giving access to seasonal variability of the site.

More, doing a five dimensional analysis of moving atmospheric speckle patterns on a double star, we are able to present in this report the temporal evolution of important integrated variables such as the coherence time of the light wave-front.

The management of such a long campaign was made possible with the help of various people belonging to many organizations and with the financing of AURA.

In Fig. 2 appears most of the actors of this campaign.



FIGURE 2: With participation of: Ann, Leonardo, Jean, Quique, Karim, Aziz, Francis, Remy, Max and Mark.

Chapter 1

INSTRUMENTAL METHODS

Here we sketch the basic formulae which define most of the important parameters and describe the principle of each of the experiments used during the 1998 site testing campaign. For a more detailed explanation one could see two articles from Vernin and Muñoz-Tuñón, 1992 and 1994, in A&A, and Avila et al., 1997 and 1998.

1.1 Review

Since the early theory given by Tatarski (1961) on wave propagation in turbulent media and following the recent contributions of Roddier (1981) and Coulman (1985), which are more specifically relevant to astronomical applications, it is known that the full width at half the maximum of the image point spread function obtained at the focus of a "large" telescope, is given by:

$$\varepsilon_{fwhm} = 0.98 \frac{\lambda}{r_0} \quad (1.1)$$

where λ is the optical wavelength and r_0 is the so-called Fried's parameter (Fried, 1966). As will be shown later, r_0 takes into account all the different turbulent layers encountered by the light beam before reaching the ground. In order to give the reader a feeling for the magnitude of the above quantities, a typical value of $r_0 = 10cm$ would produce a point spread function of about one arcsecond at visible wavelengths.

Temperature inhomogeneities which are generated in turbulent layers are responsible for local variations in the refractive index which perturbs the otherwise homogeneous propagation of incident lightwaves. The parameter which gives a measure of the optical turbulence intensity related to the inhomogeneities is the refractive index structure constant $C_N^2(h)$. The relationship between geophysical and optical magnitudes was given by Fried (1966) via the expression:

$$r_0 = (16.7 \lambda^{-2} \int_0^\infty C_N^2(h) dh)^{-3/5}. \quad (1.2)$$

Using the above expressions it is possible to write:

$$\varepsilon_{fwhm} = 5.25 \lambda^{-1/5} \left(\int_0^\infty C_N^2(h) dh \right)^{3/5}. \quad (1.3)$$

One might wonder why is it important to know the vertical behaviour of $C_N^2(h)$ since from the above formulae, its integral is sufficient. For adaptive optics or interferometry, the following expressions will tell us that not only $C_N^2(h)$ profiles are needed but also wind profiles.

From many theoretical and experimental works which have been summarized in Vernin et al., 1991, and from the simultaneous knowledge of the $C_N^2(h)$ and wind velocity profiles it is possible to deduce the speckle lifetime τ and the isoplanatic angle θ . The relevance of these parameters in modern astronomy is well known. The speckle lifetime is a measure of the optimal exposure time in order to record interferograms with the maximum flux compatible with the speckle motion. The isoplanatic angle represents the maximum angular extent on the sky for spatial coherence of the wave front, allowing the same image reconstruction technique to be applied on different stellar sources. These quantities can be assessed for two different purposes, i.e. speckle inteferometry and adaptive optics. In each case the formal expressions are slightly different and the parameters, noted as τ_{SI}, θ_{SI} and τ_{AO}, θ_{AO} , can be obtained as follows (see Roddier et al., 1982a, 1982b and references therein):

$$\tau_{SI} = 0.36 \frac{r_0}{v_{SI}} \quad (1.4)$$

$$\tau_{AO} = 0.31 \frac{r_0}{v_{AO}} \quad (1.5)$$

$$\theta_{SI} = 0.36 \frac{r_0}{h_{SI}} \quad (1.6)$$

$$\theta_{AO} = 0.31 \frac{r_0}{h_{AO}} \quad (1.7)$$

where the values $v_{SI}, v_{AO}, h_{SI}, h_{AO}$ are velocities and altitudes given by:

$$v_{SI} = \left[\frac{\int_0^\infty |V(h)|^2 C_n^2(h) dh}{\int_0^\infty C_n^2(h) dh} - \left| \frac{\int_0^\infty \mathbf{V}(h) C_n^2(h) dh}{\int_0^\infty C_n^2(h) dh} \right|^2 \right]^{1/2} \quad (1.8)$$

$$v_{AO} = \left[\frac{\int_0^\infty |V(h)|^{5/3} C_n^2(h) dh}{\int_0^\infty C_n^2(h) dh} \right]^{3/5} \quad (1.9)$$

$$h_{SI} = \left[\frac{\int_0^\infty h^2 C_n^2(h) dh}{\int_0^\infty C_n^2(h) dh} - \left(\frac{\int_0^\infty h C_n^2(h) dh}{\int_0^\infty C_n^2(h) dh} \right)^2 \right]^{1/2} \quad (1.10)$$

$$h_{AO} = \left[\frac{\int_0^\infty h^{5/3} C_n^2(h) dh}{\int_0^\infty C_n^2(h) dh} \right]^{3/5} \quad (1.11)$$

Then we give the d_0 parameter, known as “cone effect” valid when piston and tilt have been removed. The following expression can be found in Avila et al., 1998, derived from Lloyd–Hart et al., 1995:

$$d_0 = r_0 \left(\frac{1.18}{H_{ls}^{5/3}} \frac{\int dh h^{5/3} C_n^2(h)}{\int dh C_n^2(h)} - \frac{1.06}{H_{ls}^2} \frac{\int dh h^2 C_n^2(h)}{\int dh C_n^2(h)} \right)^{-3/5} \quad (1.12)$$

where H_{ls} is the altitude at which the laser star is illuminated. Hereafter $H_{ls} = 90km$ will be used for numerical application.

Here we introduce an optimum altitude h_{opt} which optimizes the isoplanatic angle if one were putting the deformable mirror at this altitude, instead of right into the entrance pupil of the telescope (see Avila et al., 1998). It is the altitude h_{dm} which minimizes the following integral

$$\int dh(h - h_{dm})^2 C_n^2(h). \quad (1.13)$$

We then define the optimal isoplanatic angle θ_{opt} , and the expected gain θ_{opt}/θ . The equivalent altitude of the turbulent layers, when the deformable conjugated mirror is at the altitude h_{opt} , is expressed by:

$$h_{dm} = \frac{\int dh C_n^2(h)(h - h_{opt})^2}{\int dh C_n^2(h)} \quad (1.14)$$

and finally the equivalent altitude of the turbulent layers above the pupil:

$$h_{eq} = \frac{\int dh C_n^2(h)(h - h_{obs})^2}{\int dh C_n^2(h)} \quad (1.15)$$

where h_{obs} is the altitude of the observatory.

For each balloon launching the profiles of $C_n^2(h)$ and $V(h)$ are obtained and it is possible to work out θ and τ using the above expressions.

It will be explained later that the G-Scidar is also able to give the velocity and the optical turbulence strength in each detected turbulent layer, and thus, one can infer θ and τ . The main difference between those two techniques is that the G-Scidar delivers hundreds of measurements each night, but the balloon only one.

1.2 Definition of atmospheric slabs

Hereafter we adopt different words which refers to different atmospheric slabs which contribute to image degradation. The first kilometer of atmosphere is called the boundary layer (BL), in which takes place turbulence triggered by orographycal local effects. The rest of the atmosphere is called free atmosphere (FA). Local orography does not play an important role in this slab. But one needs to bear in mind that large scale steep montaneous structure can affect the air flow up to altitudes as high as 20km (Masciadri et al., 1999 a and b). In the BL, the first few tens of meters adds a large turbulent contribution, due to rugosity effects, it is the so-called surface layer (SL).

We call dome seeing the turbulent contribution originating inside the dome. The mirror seeing corresponds to turbulent motion very close to the main mirror. With our experiment it is not possible to separate the respective contribution of dome and mirror, and we adopt **“Dome seeing” for the sum of these perturbations**.

No one of our deployed experiments is sensitive to mirror aberrations.

1.3 Scidar

1.3.1 Principle of the Generalized Scidar (GS)

The scidar technique has been extensively explained elsewhere, Rocca et al. 1974, Caccia et al. 1987, Vernin 1992). Avila et al. (1997) presented the first experimental implementation and results of the GS, the concept of which was introduced by Fuchs (1995). For completeness, we give here a brief overview of the GS technique.

This technique consists in computing the spatial autocorrelation function of short exposure-time images of the scintillation pattern produced by a double star. In the classical scidar, images of the telescope pupil are taken, which makes it insensitive to turbulence close to the ground because the scintillation variance is proportional to $h^{5/6}$, Roddier (1981), where h is the altitude above the ground of the turbulent layer (acting as a phase screen). In the GS the plane of the detector is made the conjugate to a plane (analysis plane) at a distance h_{gs} , of the order of a few kilometers, below the telescope pupil ($h_{gs} < 0$). In this case the turbulence at ground level (including the telescope dome) becomes detectable because the distance relevant for scintillation produced by a turbulent layer at an altitude h is now $|h - h_{gs}|$.

The autocorrelation of the scintillation produced by a turbulent layer consists of three components: one is centered at the origin, and the two others are separated by $\vec{\rho}H$ and $-\vec{\rho}H$, respectively, where $\vec{\rho}$ is the angular separation of the double star, and $H = |h - h_{gs}|$, which is equal to $h - h_{gs}$ for the case of interest $h_{gs} < 0$. As the different turbulent layers are statistically independent, the contribution of each one is added, and the total theoretical autocorrelation function can be written as:

$$C^{**}(\mathbf{r}) = \int_0^\infty dh C_N^2(h) \{ a\mathcal{C}(\mathbf{r}, h) + b[\mathcal{C}(\mathbf{r} - \vec{\rho}h, h) + \mathcal{C}(\mathbf{r} + \vec{\rho}h, h)] \}, \quad (1.16)$$

where $\mathcal{C}(\vec{r}, h)$ represents the autocorrelation of the scintillation of a single star produced by a layer of unit C_N^2 , at an altitude h . The factors a and b are given by

$$a = \frac{1 + \alpha^2}{(1 + \alpha)^2}, \quad b = \frac{\alpha}{(1 + \alpha)^2}, \quad \alpha = 10^{-0,4\Delta m}, \quad (1.17)$$

Δm being the magnitude difference of the double star.

Equation (1.16) shows that all the information needed to retrieve $C_N^2(h)$ is contained in a radial section of $C^{**}(\vec{r})$ along the double star separation. Furthermore, we wish to eliminate the central peak where the contribution of each layer is undistinguishable from that of the others, as they are added, and it contains the uncorrelated noise. For this purpose is calculated the difference of the sections of the measured autocorrelation function parallel and perpendicular to the stars separation, C_{\parallel}^{**} and C_{\perp}^{**} respectively, which can be written as (Avila 1997) :

$$\begin{aligned} B_{gs**}(x) &\equiv C_{\parallel}^{**} - C_{\perp}^{**} \\ &= \int_{-h_{gs}}^{+\infty} dh K(x, h) C_N^2(h - h_{gs}) + N(x). \end{aligned} \quad (1.18)$$

$N(x)$ is the noise, and the kernel $K(x, h)$ is a radial section of $b\mathcal{C}(\vec{r} - \vec{\rho}H, H) * S(\vec{r})$ (see Eq. [1.16]) along the direction $\vec{r} \parallel \vec{\rho}$, where $S(\vec{r})$ is the autocorrelation of the impulse response of the detector. By measuring $B_{gs**}(x)$, calculating theoretically $K(x, h)$ and knowing h_{gs} as well as an estimation of the noise variance, Eq. (1.18) (of Fredholm type) is inverted to retrieve $C_N^2(h)$ using a maximum entropy algorithm. The inversion is simplified by the diagonal elements in $K(x, h)$ along the line $x = \rho(h - h_{gs})$.

Important features of the GS should be noted: The space between the telescope pupil and the analysis plane is turbulence-free because it is virtual. The $C_N^2(h)$ measurements are independent to static optical aberrations, as they are canceled out in the data analysis. The vertical resolution of the retrieved $C_N^2(h)$ profiles (Vernin 1983) is given by

$$\Delta H = \frac{\mathcal{L}(h - h_{gs})}{\rho} = \frac{0.5}{\rho} \sqrt{\lambda(h - h_{gs})}, \quad (1.19)$$

where $\mathcal{L}(h - h_{gs})$ is the equivalent width of the scintillation spatial autocorrelation function, related to the first Fresnel zone, and λ is the wavelength. As an example, the resolution achieved at ground level ($h = 0$) when observing the double star 95 Herculis ($\rho = 6, 2$ arcsec), with the analysis plane at $h_{gs} = -4$ km, is $\Delta H = 740$ m.

1.3.2 Simultaneous measurement of $C_N^2(h)$ and $\mathbf{V}(h)$ from double star scintillation

Principle

The Taylor's hypothesis of "frozen turbulence" states that the turbulence is carried by the wind without deformation, which is valid during short enough times. The scintillation pattern produced by a layer where the wind velocity is \mathbf{V} , will move, on the analysis plane, a distance $\mathbf{V}\Delta t$ in a lapse Δt . The wind velocity can be determined by measuring the displacement $\mathbf{V}\Delta t$, which can be achieved by computing the cross-correlation of scintillation images taken at times separated by a known constant delay Δt . When the source is a double star, the cross-correlation will result in three peaks (that we call a triplet), like in the case of the autocorrelation, but the central peak will no longer be situated at the origin but at the location $\mathbf{r} = \mathbf{V}\Delta t$. As in the autocorrelation, the separation between the central and the lateral peaks is $\vec{\rho}H$ and $-\vec{\rho}H$, respectively (see Section 1.3.1). In the realistic case of multiple layers, by analogy to Eq. (1.16), the cross-correlation is written as:

$$IC^{**}(\mathbf{r}, \Delta t) = \int_0^\infty dh C_N^2(h) \{ a\mathcal{C}(\mathbf{r} - \mathbf{V}(h)\Delta t, h) + b[\mathcal{C}(\mathbf{r} - \mathbf{V}(h)\Delta t - \vec{\rho}h, h) + \mathcal{C}(\mathbf{r} - \mathbf{V}(h)\Delta t + \vec{\rho}h, h)] \}. \quad (1.20)$$

The cross-correlation contains all the information needed to retrieve $C_N^2(h)$ and $\mathbf{V}(h)$. An example is given in Fig. 1.1, where 3 triplets can easily be identified, corresponding to altitudes of 2400, 6500 and 19500 m above sea level.

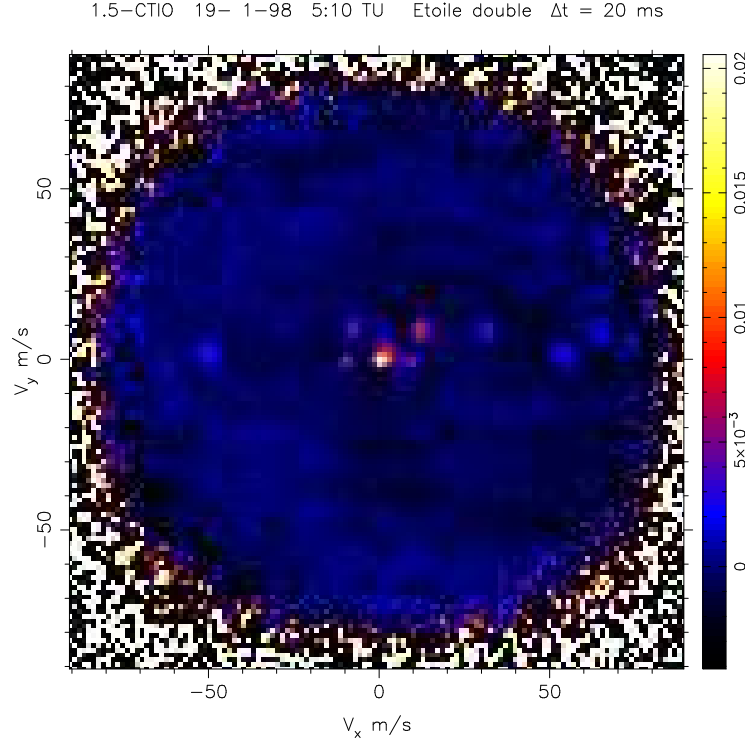


FIGURE 1.1: Cross-correlation of scintillation images separated by $\Delta t = 20ms$, obtained with the double star $\kappa Pups$, of angular separation $\rho = 9.9$ arcsec. The coordinates of the central peak of each of the 3 triplets give the wind velocity of the corresponding layer.

Experimental method

The GS measures simultaneously the autocorrelation $C^{**}(\mathbf{r})$ of the scintillation images (of 1 to 2 ms exposure time), and two cross-correlations, $IC^{**}(\mathbf{r}, 20ms)$ and $IC^{**}(\mathbf{r}, 40ms)$, one of images separated by a lapse $\Delta t = 20$ ms, and the other of images separated by $\Delta t = 40$ ms. The number of images used for these calculations vary from 1000 to 2000, depending on the star magnitudes, and the computations are made in quasi-real time, using a Matrox Genesis board equipped with a C80 Digital Signal Processor. One set of correlations is obtained every 45 to 90 sec, depending on the number of images processed. Each detector pixel covers a square area on the pupil, of side $dx = 2.8$ cm.

An interactive algorithm has been developed for the determination of \mathbf{V} , h and the turbulence intensity of the different turbulent layers. The input data are the cross-correlations $IC^{**}(\mathbf{r}, 20ms)$ and $IC^{**}(\mathbf{r}, 40ms)$, as well as the corresponding $C_N^2(h)$ profile which must have been retrieved previously from the autocorrelation, using the method presented in Section 1.3.1. For a given triplet (as in Fig. 1.1), the user identifies, with the mouse, the position of the central peak and that of either of the lateral peaks. The central peak position gives \mathbf{V} , and the distance between the central and the lateral peaks gives a preliminar altitude h_p . The turbulence intensity associated with that triplet, and the final altitude, are found from the $C_N^2(h)$ profile, as follows. The triplet is associated an uncertainty δh_p in the altitude

determination, which depends on several parameters: the altitude resolution ΔH , given by Eq. (1.19), an estimated enlargement of the peaks due to wind velocity fluctuations, the pixel size, and the peak amplitudes. The actual altitude h selected for the layer is that corresponding to the maximum C_N^2 value between $h_p - \delta h_p/2$ and $h_p + \delta h_p/2$. Finally, the turbulence intensity $I_{C_N^2}$ associated to this layer is equal to the integral of the $C_N^2(h)$ profile between the altitudes $h - \Delta H/2$ and $h + \Delta H/2$. Once a triplet has been analyzed, it is *cleaned* from the cross-correlations, by subtracting a theoretical triplet calculated using the retrieved parameters \mathbf{V} , h , and $I_{C_N^2}$.

Usually there are several layers apparently at the same altitude, with different velocities. Our interpretation is that they are actually situated at slightly different altitudes, that cannot be resolved in the $C_N^2(h)$ profile. The measured C_N^2 at the altitude of these layers is in fact the sum of the real C_N^2 of each layer. From this measured C_N^2 , a turbulence intensity $I_{C_N^2}$ is calculated as explained above, and it is distributed to the layers at the same altitude, with weights proportional to the peak amplitudes in each of the corresponding triplets, obtaining the final $I_{C_N^2}$ values for each layer.

All the analysis presented so far in Section 1.3 has been developed for observations at the zenith. When the source has a zenith angle z , h and h_{gs} must be replaced by $h \sec(z)$ and $h_{gs} \sec(z)$. The altitude axis in each turbulence profile and wind profile is corrected by the factor $\sec(z)$, by h_{gs} , and by the altitude of the observatory, obtaining the altitude above sea level.

The wind velocity vector \mathbf{V} , obtained with the method explained above, is in fact the projection of the actual horizontal wind vector, on the wavefront plane. So far, the de-projection has not been calculated, which has little consequence on the results, as the observations were carried out at low zenith angles ($z \leq 30^\circ$). The direction of \mathbf{V} is strongly affected by the alignment of the X axis of the detector pixels with the position angle of the double star, carried out before the observations. To obtain \mathbf{V} in the cardinal reference system, a correction must be applied, which will be done in a post-processing phase. For the calculation of the temporal parameters relevant for adaptive optics, the orientation of \mathbf{V} is not important.

Dome seeing detection

Inside the telescope dome, the mean wind velocity is zero. Thus, the turbulence inside the dome will produce a triplet located at the center of the cross-correlations. However, we cannot be sure that the central triplet corresponds exclusively to the dome turbulence, unless we detect at least another triplet, at the same altitude (that of the observatory $h = 0$), and with a non-zero velocity. In this case, the triplet(s) with non-zero velocity will be associated to turbulence close to the ground but outside of the dome, and the triplet with zero velocity (or less than the velocity resolution $dV = dx/\Delta t$) will be associated to dome turbulence. The algorithm gives one of three possible attributes to the dome seeing detection:

- *Detected*: One layer with $V \leq dV$ and $h = 0 \pm \Delta H/2$, and at least one layer with $V > dV$ and $h = 0 \pm \Delta H/2$ were detected.

- *Ambiguity*: One layer with $V \leq dV$ and $h = 0 \pm \Delta H/2$, but no layer with $V > dV$ and $h = 0 \pm \Delta H/2$ were detected.
- *Not detected*: No layer with $V \leq dV$ and $h = 0 \pm \Delta H/2$ was detected.

If the dome seeing is detected, the values of $I_{C_N^2}$ associated to the turbulence inside and outside the dome, respectively, are calculated as in the case, explained above, of several turbulent layers at apparently the same altitude. The only difference consists of an additional precaution, that accounts for the slower temporal decorrelation of the turbulence inside the dome than outside.

New $C_N^2(h)$ processing excluding Dome seeing

Let us imagine that dome seeing has been detected using the previous method and let us define its contribution to scintillation throughout the knowledge of the Kernel, as expressed in Eq. 1.18:

$$\begin{aligned} B_{Dome-gs**}(x) &\equiv C_{||}^{**} - C_{\perp}^{**} \\ &= \int_{-h_{gs}}^{+\infty} dh K(x, h) (C_N^2 \Delta h)_{Dome} \delta(h), \end{aligned} \quad (1.21)$$

where we have written $(C_N^2 \Delta h)_{Dome}$ instead of the turbulence intensity $I_{C_N^2}$ in the dome, to maintain the analogy with Eq. 1.18, and $\delta(h)$ means that the integral is restrained to $h = 0$, the altitude of the observatory. In other words, the scintillation due to dome seeing is given by the line in the kernel which coincides with the observatory altitude, weightened with the optical turbulence which is derived from the previous multiple layer detection.

Then, instead of processing Eq. 1.18, we process the difference $B_{gs**} - B_{Dome-gs**}$, using exactly the same maximum entropy method.

When the detection of the dome seeing is *ambiguous*, as explained above, what value should we give to $(C_N^2 \Delta h)_{Dome}$? There are two opposite choices: to associate the *ambiguous* triplet exclusively to turbulence inside the dome or exclusively to turbulence outside the dome. In the first case, $(C_N^2 \Delta h)_{Dome}$ takes the value of the $I_{C_N^2}$ associated to the *ambiguous* triplet, and in the second case, $(C_N^2 \Delta h)_{Dome}$ takes the value of zero.

We have performed 3 different data reductions for the calculation of $C_N^2(h)$:

1. Without removing dome turbulence. This is exactly the data reduction that was performed before the development of the algorithm for the dome seeing detection.
2. Removing dome turbulence, and in case of *ambiguity*, the turbulence intensity corresponding to the *ambiguous* triplet is entirely associated to the dome, thus it is removed.
3. Removing dome turbulence, and in case of *ambiguity*, the turbulence intensity corresponding to the *ambiguous* triplet is entirely associated to outside the dome, thus it is not removed.

1.3.3 Simultaneous measurement of $C_N^2(h)$ and $V(h)$ from single star scintillation

In principle, it has been shown by Caccia et al., 1987, and Caccia and Vernin, 1990, that optical turbulence $C_N^2(h)dh$ and $V(h)$ can be assessed from single star scintillation. This data processing has not been implemented yet.

1.4 Generalized Seeing Monitor (GSM)

1.4.1 GSM instrument

The GSM experiment has been developed at the Département d'Astrophysique de l'Université de Nice, in the framework of Atmospheric Turbulence team conducted by F.Martin, J.Borgnino and A.Ziad, in collaboration with A.Tokovinin from the Sternberg Astronomical Institute of the Moscow University.

The GSM instrument which it was mainly built for measuring the wavefront outer scale \mathcal{L}_0 , can also give estimations of seeing ε_0 (or Fried parameter r_0), isoplanatic angle θ_0 and wind (speed and direction) of atmospheric turbulence layers. To estimate those parameters, GSM uses its basic tool which is angle of arrival (AA) measurement and its statistical analysis. Indeed, the dependence of AA covariance to wavefront outer \mathcal{L}_0 in the case of two pupils of diameter D separated by a baseline B and using the Von Karman model is given by Avila et al. (1997b):

$$\begin{aligned} \mathcal{C}_\alpha(B, \gamma, D, \mathcal{L}_0) = & 0.0716 \lambda^2 r_0^{-5/3} \int_0^{+\infty} df f^3 \left(f^2 + \frac{1}{\mathcal{L}_0^2} \right)^{-11/6} \\ & \times [J_0(2\pi f B) - \cos(2\gamma) J_2(2\pi f B)] \left[2 \frac{J_1(\pi D f)}{\pi D f} \right]^2 \end{aligned} \quad (1.22)$$

where γ is the angle between the x-axis and baseline, f is the spatial frequency and λ the wavelength. In order to avoid the Fried parameter r_0 dependence, this expression is normalized by a differential variance which less sensitive to \mathcal{L}_0 (Ziad 1993). The expression of this differential variance can be deduced from the covariance one by putting $B = 0$.

The GSM instrument consists of 4 identical modules observing the same star. Each module is equipped with 10-cm Maksutov telescope, an optical device and connected by an electronic interface to a computer managing simultaneously the 4 instruments. The AA are measured by means of flux modulation obtained by star displacement over Ronchi grating. The modulated flux for the 4 modules are detected simultaneously by photomultipliers and transmitted to the computer. Three equatorial mounts are used to compensate the star diurnal motion, as shown in the Fig. 1.2.

GSM was installed on three piers (Fig. 1.2). The central pier held a mounting with two modules (1 and 2) working as DIMM instrument with 25cm baseline. At a distance of 0.8 m to the south the second pier with a mounting and module 3

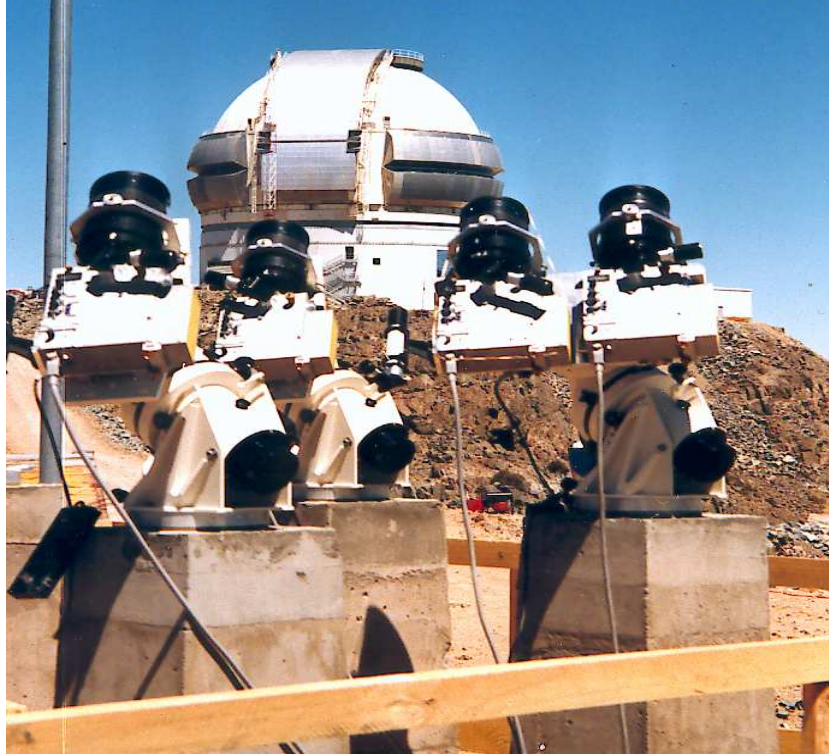


FIGURE 1.2: The GSM instrument at Cerro Pachon.

was located. Third pier with module 4 was at 1.0 m to the east of the central one. Thus the instrument had a compact L-shaped configuration (Fig. 1.3). The distances between piers were chosen for optimal sensitivity of the angle of arrival (AA) covariance to outer scale. Telescope objectives were located 3 m above the ground level. The wind-induced telescope vibrations present a potential problem in AA measurements. To reduce their effect, the instrument was surrounded by a protective net (30 % wind transparency) from 3 sides (north, east and west). The net was 4 m high, and completely decoupled from piers.

The container-type building with computers and observers was located at about 5 m from the central pier, to the south-west. With a prevailing wind from the North the GSM was supposed to be free from the locally generated turbulence, and the building was not troublesome either. On the other hand, with the southern wind GSM was in the turbulent lee created by its own building.

1.4.2 Data acquisition and reduction

Observing procedure

A stellar source was selected from a list of single bright stars (Table 1.1) that pass close to zenith at Cerro Pachon at this season. Due to the limitation of the possible hour angles (in the adopted configuration the telescopes could not be pointed at hour angle less than 1 h before meridian because they touched the piers) the selected star was usually some 40 min. before meridian at the start, and 2-3 h after meridian at

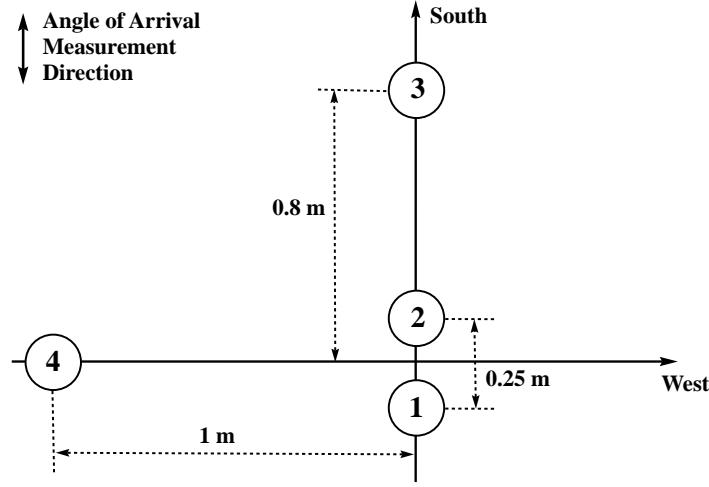


FIGURE 1.3: The GSM configuration at the Cerro Pachon site.

the end of the observation (depending on the availability of a more suitable source). Observations were obtained at zenith angles from 0° to 45° . At least once per night the modulation amplitude was checked and re-adjusted (its slight dependence on temperature was noted).

Code	HR	R.A., Dec. (2000)						V	$B - V$	Spectral type
		h	m	s	$^{\circ}$	$'$	$''$			
aphe	99	0	26	17.0	-42	18	22	2.39	1.09	K0III
ssgr	7121	18	55	15.9	-26	17	48	2.02	-0.22	B2.5V
apav	7790	20	25	38.9	-56	44	6	1.94	-0.20	B2IV
agru	8425	22	8	14.0	-46	57	40	1.74	-0.13	B7IV
apsa	8728	22	57	39.1	-29	37	20	1.16	0.09	A3V

TABLE 1.1: Informatio on the observed stars with GSM during Cerro Pachón campaign.

After pointing to the source, the telescopes were focused by looking at the modulation contrast and trying to maximize it. Then the acquisition sequence was started, interrupted every 30-40 minutes for centering of the star in the field of view. Signal was normally registered during 2 mn, and these acquisitions were repeated every 4 mn. Occasionally, longer or shorter acquisition times were used for exploratory purpose. Normal sequence of acquisitions was performed automatically, but it was commanded manually in special circumstances (clouds etc.). An observing log-book was maintained as a supplement to computer database, for various comments.

Immediately after acquisition the data were transferred to hard disk and processed. This enabled a quick assessment of data quality and results, including the seeing isoplanatic angle and \mathcal{L}_0 .

Data reduction algorithm

As explained in ESO report (1996), GSM data file consists of the 2-byte integer flux values recorded every 5 ms which correspond to the A, B, C, D signals in our notation. Thus, nominal data rate is 1600 bytes per second, and a standard 120s acquisition occupies 192 KB of disk space. Relevant parameters and processing results are stored in the database, hereafter called GSM.DAT. After every night the data were backedup.

The data reduction can be decomposed into following three steps:

1. First pass: reading data file and computing modulation phase, contrast and flux. The corresponding formulae are given in Martin et al. (1994). The phases are computed as fractions of grating period and then an integer number of periods is added from phase continuity considerations. Sometimes, when noise spikes become comparable to the half-period, a phase jump may occur. Phase jumps are detected and eliminated during the first pass by a special filter (which, in fact, is the most time-consuming part at this stage).

During first pass the mean flux, flux fluctuations, mean contrast and contrast fluctuations (as a mean square difference of adjacent contrast values) are computed as well. The computation of matrix elements for the rms parabolic trend adjustment is performed. The trend is caused by small residual linear motion due to imperfect orientation of mounting axes.

2. Second pass (statistical calculations). The phases are read from temporary file. Trend is subtracted. Angle of arrival (AA) variances and covariances are computed. The photon and scintillation noise is subtracted from phase variances.

Noise estimate is based on the contrast fluctuations as computed during pass 1. It can be shown that the phase noise σ_p^2 (in units of grating period squared) is related to the contrast fluctuations σ_C^2 as follows:

$$\sigma_p^2 = \sigma_C^2 / [8\pi^2 C^2 (1 + 4C^2/\pi^2)], \quad (1.23)$$

where C is the mean contrast. This formula is obtained by calculating $\langle C^2 \rangle - \langle C \rangle^2$ under assumption that relative flux variations in the 4 channels ABCD are uncorrelated and are equal to δ . The relation between δ and σ_p^2 is given in Martin et al. (1994). For pure photon noise $\delta = 1/N$, N being the average number of photons per channel. Thus the *noise factor* $f_2 = \delta N$ is equal to 1 for poisson noise and is > 1 when scintillation noise is added.

The temporal averaging during 5 ms has negligible effect on the computed AA covariances and dispersions, but is non-negligible for differential AA variance σ_d^2 because its spectrum has more power at high temporal frequencies. A correction for time averaging is performed by computing additionally the AA variances with a degraded temporal resolution of 10 ms. Then the "true" variance corresponding to zero integration time is estimated as

$$\sigma_d^2(0\text{ms}) = 2\sigma_d^2(5\text{ms}) - \sigma_d^2(10\text{ms}) \quad (1.24)$$

This linear extrapolation law was found from the study of exposure time influence conducted by Ziad and can be explained by the power-law character of the AA spectrum ($\sigma_d^2(\tau)$ continues to increase as τ approaches 0). In ESO report (1996)

it was shown that the uncertainty of the correction for finite integration time constitutes a major source of measurement errors of σ_d^2 . Now, when this correction is properly taken into account, this error term must not be included in the error calculation.

The scintillation index σ_I^2 (flux variance normalized by the square of mean flux) is computed during pass 1 with a 5 ms time resolution from the variance of the sum of ABCD (thus annullating the flux modulation). It should be noted that a global flux variance for the whole acquisition is computed, and it is sensitive to the low-frequency flux variations, e.g. due to clouds. The scintillation index for partially cloudy nights is thus overestimated and must not be used for high altitude turbulence characterization. This scintillation is also corrected for temporal averaging in a similar manner than σ_d^2 , i.e. by comparing the 5 ms and 10 ms indexes and extrapolating linearly to 0 ms. The scintillation index σ_I^2 measurements will be used to estimate the isoplanatic angle θ_0 from the next formula as it was suggested by Loos and Hogge (1979):

$$\theta_0 = A(\sigma_I^2)^{-3/5} (\sec z)^{8/3} \quad (1.25)$$

where z is the zenithal angle and A is a coefficient depending on the wavelength and on the altitude h of the turbulent layer producing scintillation. For GSM aperture ($D=10$ cm) the altitude h is fixed at 10 km which gives $A=0.1986$ for 500 nm wavelength.

3. Third pass. The AA covariances normalized by the differential variance are compared to the theoretical normalized covariances which are stored in a file for a grid of baseline coordinates (x, y) and a logarithmic grid of outer scale values. For each baseline its projection onto the sky is calculated, using the time of acquisition (to compute the hour angle), the star name code (to look for its coordinates) and the site code (to look for site coordinates). Then the theoretical covariances as a function of \mathcal{L}_0 are found by interpolating the grid to the projected baseline. Finally the appropriate \mathcal{L}_0 for each baseline is determined. The adopted value of the outer scale is taken as a median of the 6 individual values corresponding to each baseline. When a measured covariance did not provide an outer scale, e.g. being too large, this baseline was not taken into account in median calculation. The error of the final \mathcal{L}_0 values is computed from the scatter of the 6 individual estimates. We checked that the errors on \mathcal{L}_0 computed from noise considerations as detailed in ESO report (1996) are similar to the "statistical" errors obtained from the scatter.

At the third pass the r_0 values calculated from the AA dispersion of each module are corrected for the outer scale, to compare them to the "differential" r_0 . This enables to estimate the importance of telescope vibrations.

It must be noted that small variations of the measured normalized covariances lead sometimes to significant changes of the derived \mathcal{L}_0 , because theoretical curves corresponding to different \mathcal{L}_0 are rather close to each other. Thus, the corrections of the scintillation noise and of the effect of finite integration time were important, because they changed the σ_d^2 by some 10–20%. For example, it was found that with the integration time of 10 ms the derived \mathcal{L}_0 are systematically higher than the "true" \mathcal{L}_0 as given by the procedure described above.

1.5 Instrumented Balloons and Mast

1.5.1 Balloon sounding

This experiment involves the launching of meteorological balloons equipped with sensors which measure the microstructure of the thermal field during their free flight ascent. They sample the atmosphere from the ground level up to about 25km.

We used a technique similar to that of Barletti et al. (1974). The temperature structure function is defined as:

$$D_T(r) = \langle (T(x) - T(x+r))^2 \rangle \quad (1.26)$$

and is assessed by means of a pair of sensors separated by a distance r .

The temperature and refractive indices, T and N , both being passive and conservative additives, are assumed to follow the Obukhov (1949) and Yaglom (1949) spectral law. One can deduce the temperature structure constant profile $C_T^2(h)$ by :

$$D_T(r, h) = C_T^2(h) r^{2/3}. \quad (1.27)$$

C_T^2 and C_N^2 can be linked by virtue of the known mean pressure and temperature P and T , which are also measured on board:

$$C_N^2(h) = C_T^2(h) (80.10^{-6} \frac{P(h)}{T(h)^2})^2. \quad (1.28)$$

Although the general philosophy of this experiment has already been employed during similar campaigns, it is worthwhile mentioning a new set of additional measurements which provide much useful information relevant to the physics of turbulence. Among the main differences we emphasize :

a) The statistical computation of the structure function is performed electronically onboard, in real time during the flight.

b) The structure function is simultaneously calculated for two distinct separations, $r_1 = 0.3m$ and $r_2 = 0.95m$. In so doing, two independent estimations of $C_N^2(h)$ are obtained. It makes also the instrument more reliable.

c) The electronic computation board is coupled to a commercial sonde (Vaisala-Finland) which is also able to transmit time, pressure, temperature, humidity and the modulus and direction of the wind. In order to obtain the wind information, the sonde measures the balloon position as well as the receiving station location, in a differential GPS way, with a very good precision. From those information, it is possible to infer the wind velocity and direction. At a 1.5 s duty cycle, the whole set of information is sent to a ground receiver. The ascent speed being of the order of 4 m/s, the effective vertical resolution is 6m. We thus have at each 6m height interval, $D_T(0.3m, h)$, $D_T(0.95m, h)$, P , T , Rh (Relative humidity), whereas the computation of the wind velocity is performed every 10 seconds ($\Delta h = 40m$).

From all of these measurements one can obtain a set of extremely valuable astrophysical and geophysical parameters. Among these we can cite :

–The integrated water vapor content, which will be of great importance in determining the infrared sky transparency.

- From the C_N^2 profile, one can obtain the isoplanatic angle (Vernin et al. 1991).
- From the knowledge of both $C_N^2(h)$ and $V(h)$, the speckle boiling time can be inferred (Vernin et al. 1991).
- From the simultaneous knowledge of microscopic parameters like $C_N^2(h)$ and macroscopic parameters like T and V , it becomes possible to construct predictive models of turbulence (Coulman et al. 1988). It is also possible to retrieve the outer scale of turbulence profile from Tatarski:

$$C_N^2(h) = a^2 M^2 L_o^{4/3} \quad (1.29)$$

with $M = dN/dz$.

From the knowledge of the vertical profiles of pressure and temperature, it is possible to infer a profile of the potential temperature $\theta(h)$ through the following relationship:

$$\theta(h) = T(h)(1000/P(h))^{0.286} \quad (1.30)$$

The potential temperature takes into account the decrease of pressure with altitude, and transform the absolute temperature into a conservative additive. This means that the absolute temperature of a parcell of air moving up or down, without heat exchange, will follow an adiabatic trend, while its potential temperature will be constant. The vertical gradient of the potential temperature is the key parameter for the static stability of the air: Depending of its positivity, negativity, or zero, the air will be stable, unstable or neutral. Along the plots shown in figures of chapter 3, one will see that generally, the atmosphere is stable. Actually, the air flow becomes turbulent, even under stable static stability, only if enough kinetic energy is injected at this altitude. The relevant parameter is then the Richardson number, which expresses the ratio between the potential and the kinetic energy:

$$\frac{d\theta}{dz} = \frac{\frac{g}{\theta} \frac{d\theta}{dz}}{\left(\frac{dU}{dz}\right)^2} \quad (1.31)$$

g being the gravity acceleration, U the wind modulus and z the altitude. If the kinetic energy overcomes the potential energy, $\frac{d\theta}{dz} > 1/4$, then the flow becomes turbulent.

1.5.2 Instrumented meteorological mast

The meteorological mast is equipped with four pairs of microthermal sensors situated respectively at 4, 8, 16.5 and 27m above ground level, and with standard meteorological sensors of temperature, humidity and wind. The principle of microthermal measurement is the same as already detailed in the last paragraph. The refractive index structure constant C_N^2 is deduced from a pair of horizontally separated microsensors.

From an astrophysical point of view, as already mentioned, the relevant parameter is the integrated C_N^2 profile. In our case, from experimental design, the vertical C_N^2 sampling is done at four levels. Due to the steep decrease of the optical turbulence with altitude, the integrated turbulence between two levels has been computed assuming a power law behaviour, instead of a linear trend.

Chapter 2

OBSERVING CAMPAIGN

The observing campaign lasted during the whole 1998 year, with the GS installed on Cerro Tololo, the balloons launched from Cerro Pachón, the GSM and the mast being set up on the SOAR site, few hundred meters from Pachón.

2.1 Geographical installation

It would have been better to install everything as close as possible to the Gemini building, but no telescope was available. We had to use the GS at the focus of the Cerro Tololo 1.5m telescope, which is the nearest site. Tololo's coordinates are $30^{\circ} 09' 55''$ S latitude and $70^{\circ} 48' 53''$ W longitude. Pachón's coordinates are $30^{\circ} 14' 26''$ S latitude and $70^{\circ} 44' 12''$ W longitude. The respective altitudes of Pachón and Tololo are 2715 and 2210m.

The balloons were launched from the Gemini site, from various spots where no crane, no container, no building, no heavy metallic pieces were obstructing the launching pad! Severe orographic effects were encountered during high wind speed condition, which means that, instead of rising up, the balloon dropped down few tens of meter when reaching the cliff of the mountain and then rose again. Under this condition it is difficult to know if the balloon actually passed through the surface layer, before reaching the boundary layer.

2.2 Time schedule

The year was splitted into 4 intensive campaigns during which both the Scidar and the balloons were used: 12–18 January, 9–15 April, 14–20 July and finally 8 night run 2–9 October. During this last run the GSM and the mast were also set up. During the rest of the year, balloons were launched regularly.

In Table 2.1 is presented the whole set of flights along with the presence of Scidar, GSM and mast. One can remark in column Wind that no wind is available on a set of flights. This is due to the fact that we used two types of radio-sonde technology. When using GPS technique coupled with a DIGICORA radio receiver, borrowed from the Centre National de la Recherche Météorologique (Toulouse,

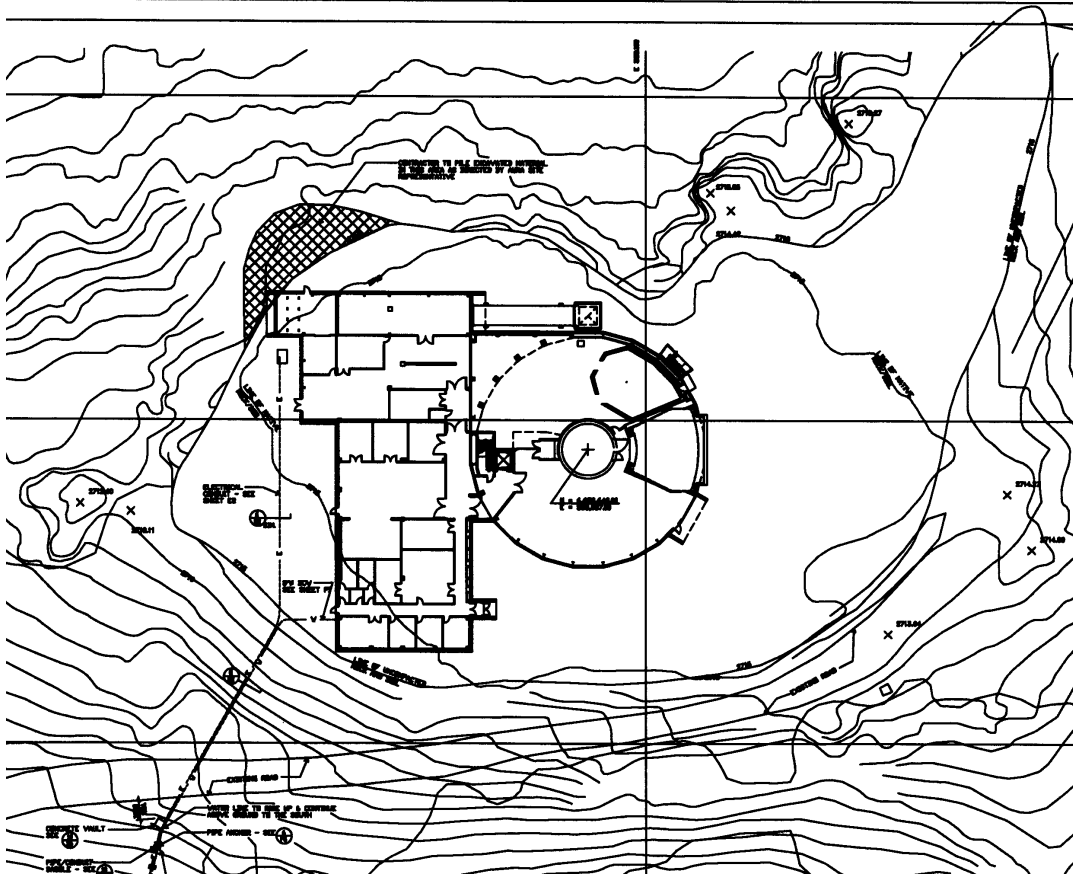


FIGURE 2.1: Map of the area of Gemini building. Depending upon the wind direction, balloons were launched from all around the main building. The radio-receiver for balloon payload was installed on the upper right part of the map, near the “tongue-like” pattern.

France), it was possible to retrieve wind and direction profiles. This equipment had prior commitments in the CNRM schedule. During these times we used a less sophisticated system (STAR), which was able to get all the optical turbulence, pressure, humidity and temperature profiles, but not wind profiles.

TABLE 2.1: Time schedule of the 1998 Cerro Pachón intensive campaign. Y means that this instrument was working, otherwise, no.

Date	Hour	Flight	Wind	Scidar	GSM	Mast	Remark
13/01	2:33	116	Y	Y			
13/01	5:14	117	Y	Y			
14/01	3:08	118	Y	Y			
15/01	2:40	119	Y	Y			
16/01	4:09	120	Y	Y			
17/01	3:44	121	Y	Y			
17/01	21:12	122	Y				Flight dur. day
18/01	2:46	123	Y	Y			
19/01	2:16	124	Y	Y			
15/04	2:15	132		Y			
15/04	4:50	133		Y			
16/04	2:05	134		Y			
16/04	4:30	135		Y			
16/07	3:46	141	Y	Y			
17/07	2:05	142	Y	Y			
17/07	4:20	143	Y	Y			
18/07	6:20	144	Y	Y			
19/07	3:20	145	Y	Y			
20/07	6:00	146	Y	Y			No bal. C_n^2
03/10				Y	Y		No flight
04/10	4:05	155	Y	Y	Y	Y	
05/10	4:26	156	Y	Y	Y	Y	
06/10	4:52	158	Y	Y	Y	Y	
07/10	4:18	159	Y	Y	Y	Y	
08/10	4:10	160	Y	Y	Y	Y	
09/10	4:57	161	Y	Y	Y	Y	
10/10	3:01	162	Y	Y	Y		

Chapter 3

INDIVIDUAL RESULTS

Here will be shown a sample of the processed output from all the instruments used. A whole set of the individual results are given in annex 7.

3.1 G–Scidar

In table 3.1 is given the number of nights during which observations have been performed by the G–Scidar vs the allocated nights. All the lost nights correspond to bad weather. At the begining of each run, a few hours were lost due to optical adjustment of the G–Scidar. In total about 76% of the nights were available for data acquisition. 6900 scintillation correlation functions have been processed, using a maximum entropy method, to give the same number of $C_N^2(h)$ profiles. We analyse these profiles night by night, run by run and finally as a whole set.

From these 6900 profiles, a large number has been processed, as explained before, in order to assess the velocity in each detected turbulent layer, as well as the dome seeing. In what follows, we will refer to **normal (N)** and to **Dome detection (D,A)**, depending on whether or not the dome detection has been taken into account. We recall to simplify, that case **D** corresponds to the case **only one turbulent layer is detected at ground level, with zero speed, the contribution of which is affected to dome**, and that case **A** corresponds to **only one turbulent layer is detected at ground level, with zero speed, the contribution of which is affected to low atmosphere**. To have a better understanding see the discussion in section 1.3.2.

TABLE 3.1: Observed and allocated nights for the G–Scidar

Run	Month	Given nights	Observing nights	Nb prof. on **
01	January	7	6	2227
02	April	7	2	399
03	July	7	6	1534
04	October	8	8	2740
Total	year	29	22	6900

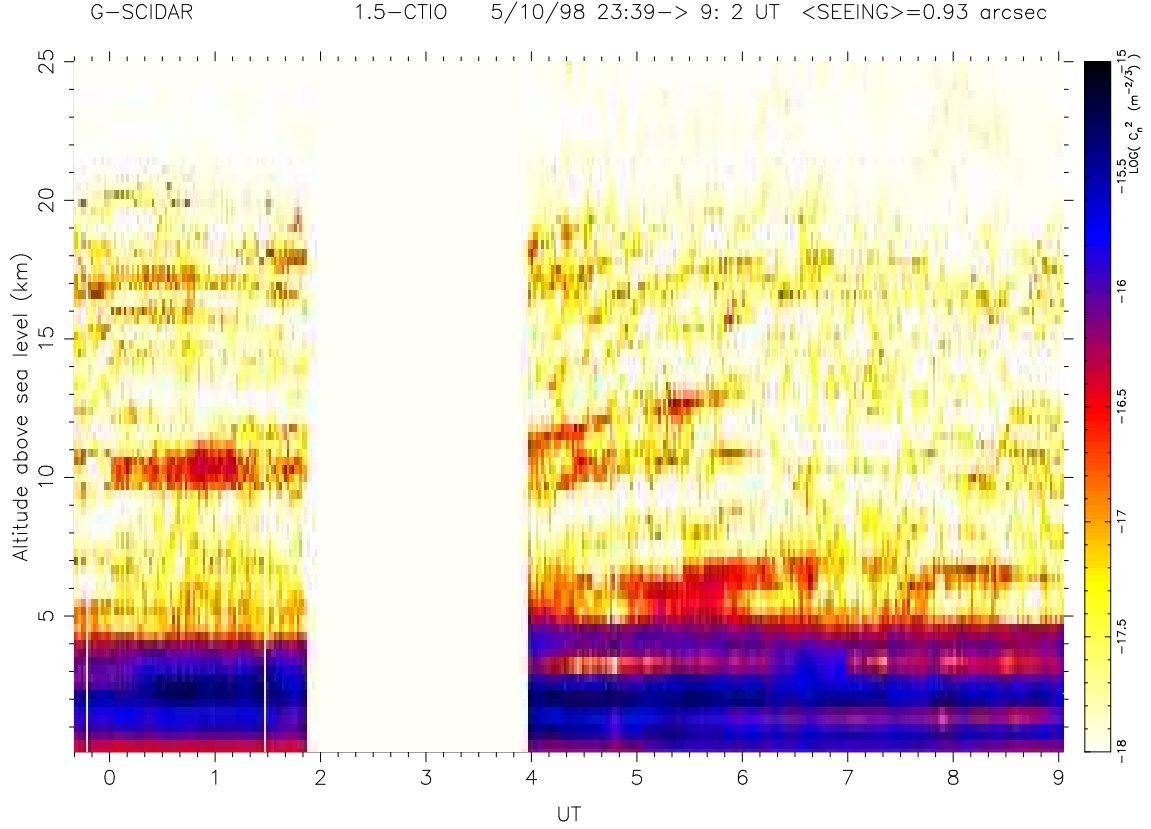


FIGURE 3.1: Temporal evolution of the optical turbulence during the whole night of 4 to 5/10/98

3.1.1 Nightly observation

Normal processing (N)

For each night, one can plot the temporal evolution of the optical turbulence, i.e $C_N^2(h, t)$, which appears in Fig. 3.1. The white horizontal line at 2.2km refers to the Cerro Tololo altitude. In this plot about 295 vertical profiles have been shown. During the whole night a strong turbulent layer is visible at the observatory altitude, which includes the contribution of the turbulence in the boundary layer, the surface layer and also the contribution of the dome and mirror seeing. During the second part of the night, a stable layer is present at 4km. From time to time, between 5 and 6 UT and around 8 UT, another layer is detected at 6.5km. Finally, other layers are visible at 10, 17 and 18km. The top label indicate the name of the instrument, the telescope, the date, the beginning and ending hours in UT, and the average seeing for this particular night.

Then, for the same night, one can deduce the temporal evolution of the seeing in Fig. 3.2; The black, red and blue lines refers respectively to the total, the first km and the free atmosphere contribution to seeing. One can observe that most of the seeing is due to the contribution of the boundary layer, as it was already noticeable in Fig. 3.1.

In Fig. 3.3 is given the temporal evolution of the isoplanatic angle according to both definitions, adaptive optics and speckle interferometry. Since most of the

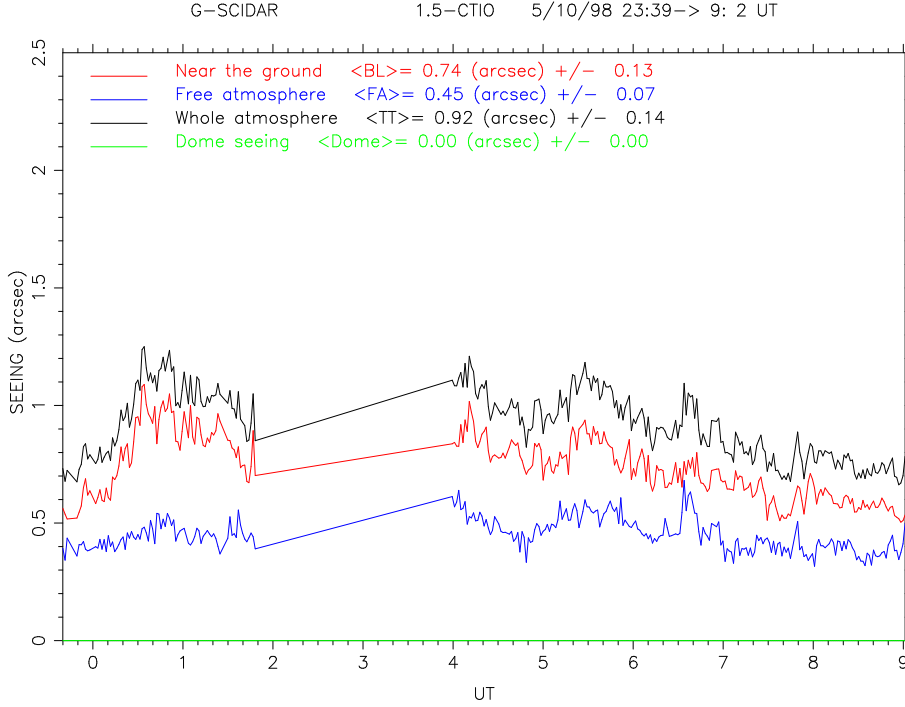


FIGURE 3.2: Temporal evolution of the seeing. Red: Boundary layer (first km); Blue: Free atmosphere (above 1km); Black: Total.

turbulence comes from the low altitude slabs, angles are quite similar.

In Fig. 3.4 are compared the scintillation index given directly by a scintillometer attached to the CTIO 1.5m telescope and the scintillation deduced from the knowledge of the $C_N^2(h)$ profile given by the G-Scidar [1983]. The red line represents the evolution of the scintillation deduced from the G-Scidar and the black refers to the simple scintillometer. At the beginning of the night, the later was not in operation, and it was switched on at 4 UT. Between 4 to 6:30 UT, both measurements agree, but then the scintillometer gave a very large value during half an hour. This can be explained by the fact that the scintillometer apparatus was attached to the border of the telescope tube and unfortunately its path ray was obstructed by the dome. Then the dome has been rotated. After 7 UT, there is a drift which is attributed to the set of the moon. Actually, the scintillation index is computed through

$$\sigma_i^2 = \langle (I - \langle I \rangle)^2 \rangle / \langle I - D \rangle^2 \quad (3.1)$$

where I is the sum of the flux of the star and the dark sky, and D is an estimation of the dark sky, at the beginning of the measurement, just withdrawing the star from field of view. Between 4 to 6:30 UT the moon was shining and the background was well removed and then the moon began to set which implies that D was more and more overestimated, thus diminishing $\langle I - D \rangle$ and overestimating σ_i^2 . Actually the moon passes below the horizon at 6:14.

One can wonder if the same effect might not also affect the G-Scidar technique, even if the zero adjust is well made at the begining of each run, removing the star from the field of view of the intensified CCD camera. We put a stop field of about 6mm in the focal plane of the telescope, which correspond to about 1 arcmin.

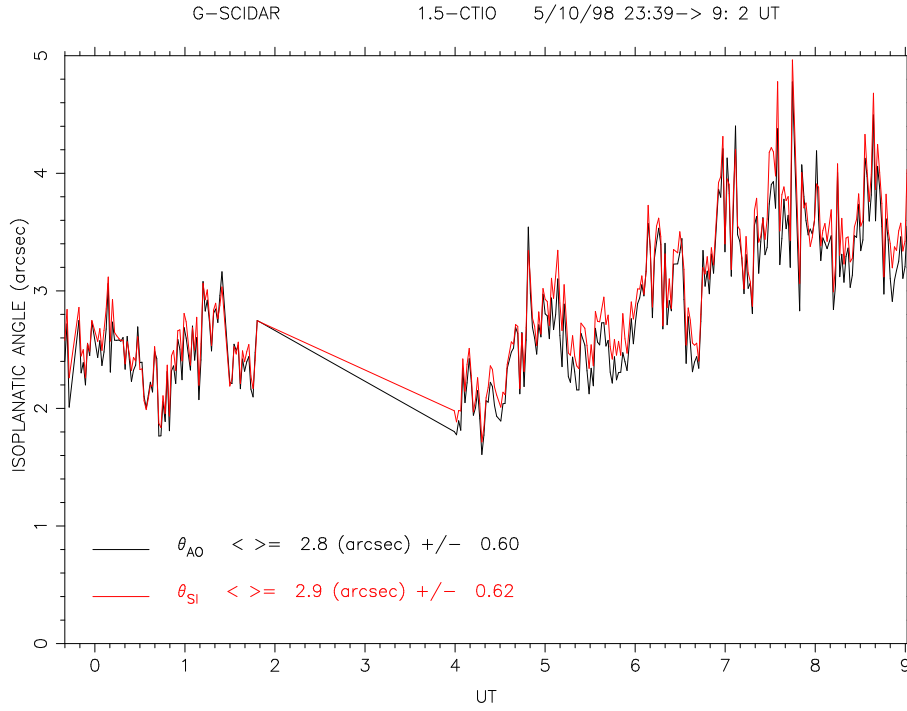


FIGURE 3.3: Temporal evolution of the isoplanatic angle during the whole night of 4 to 5/10/98. Black: Adaptive optics, red: speckle interferometry.

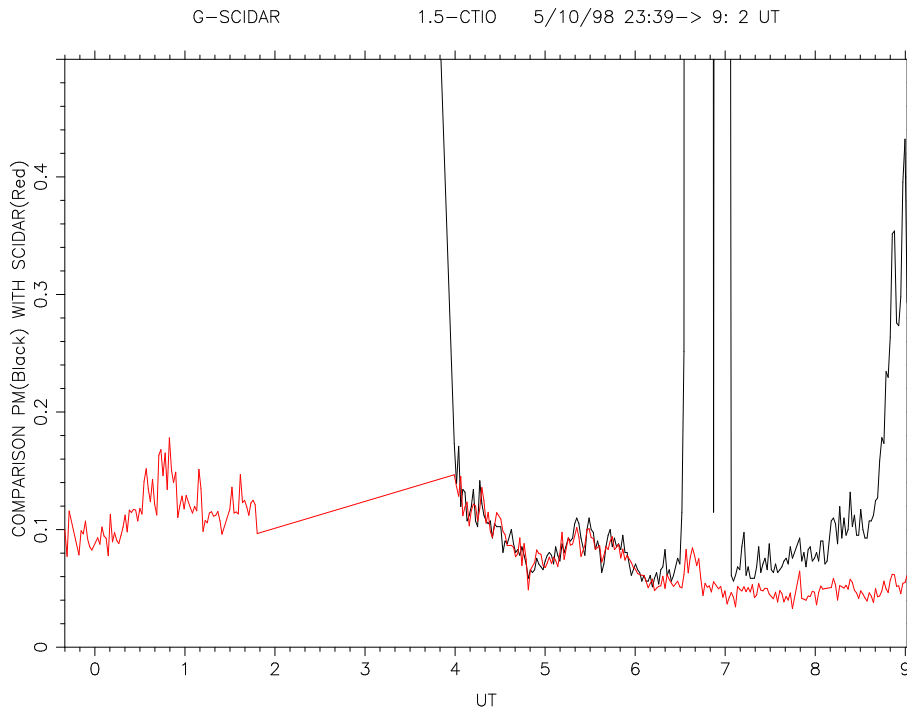


FIGURE 3.4: Comparison of the scintillation index measured by the scintillometer (black) and deduced from the G-Scidar (red).

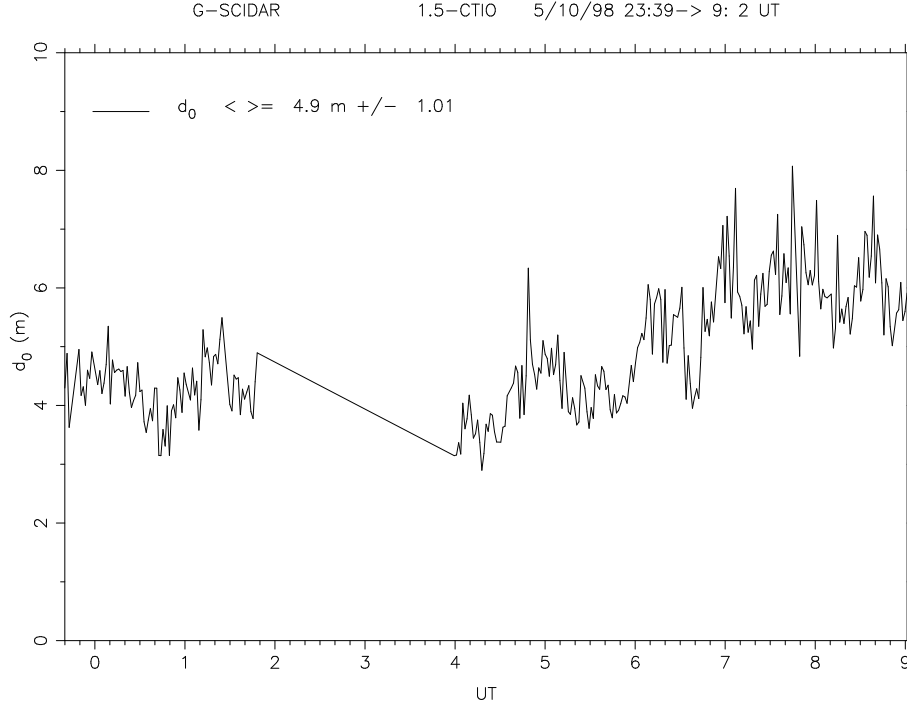


FIGURE 3.5: Temporal evolution of the “cone effect” d_0 during the whole night of 4 to 5/10/98.

This field has to be compared with the half degree stop field of the scintillometer. The dark sky is thus expected to be $30 \times 30 = 900$ time stronger for the scintillometer than for the G-Scidar, knowing that the size of a pixel of the CCD Scidar camera is almost identical to the area of the entrance lens of the scintillometer.

In Fig. 3.5 is given the temporal evolution of the “cone effect” $d_0(t)$ during the same night. And finally, in Fig. 3.6 we plotted the temporal evolution of the three variables h_{opt} in red, h_{dm} in green and h_{eq} in black, respectively defined in Eq. 1.13, 1.14 and 1.15.

For each night it is also possible to have an overview of the whole night throughout the plot of the cumulative distribution of integrated variables, such as seeing in various atmospheric slabs, θ_{OA} and θ_{SI} , as it appears in Fig. 3.7, for the same night.

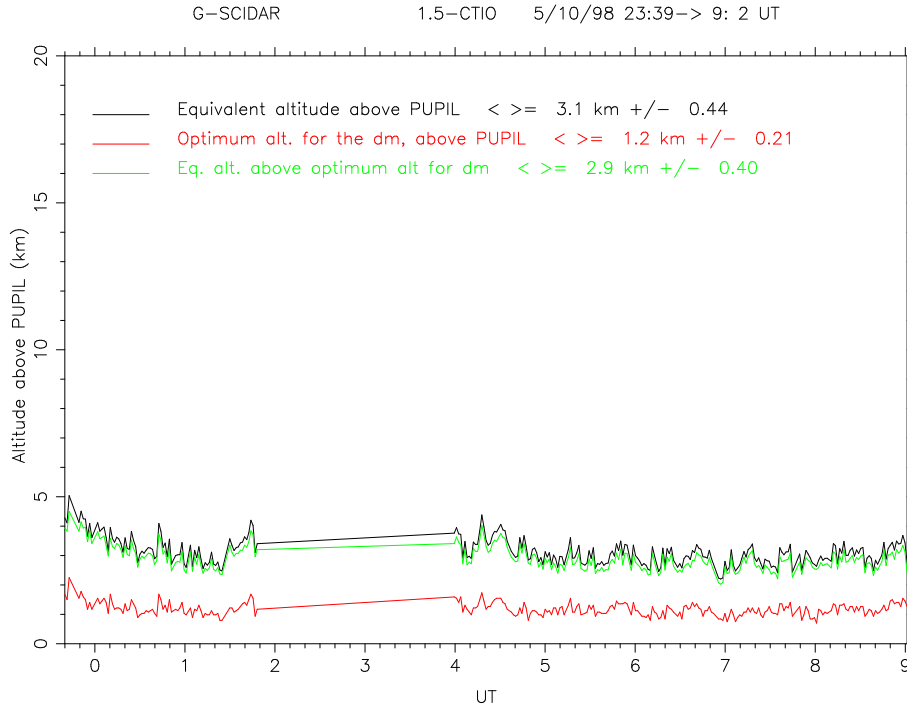


FIGURE 3.6: Temporal evolution of h_{opt} in red, h_{dm} in green and h_{eq} (see text and Eq. 1.13, 1.14 and 1.15) in black during the whole night of 4 to 5/10/98.

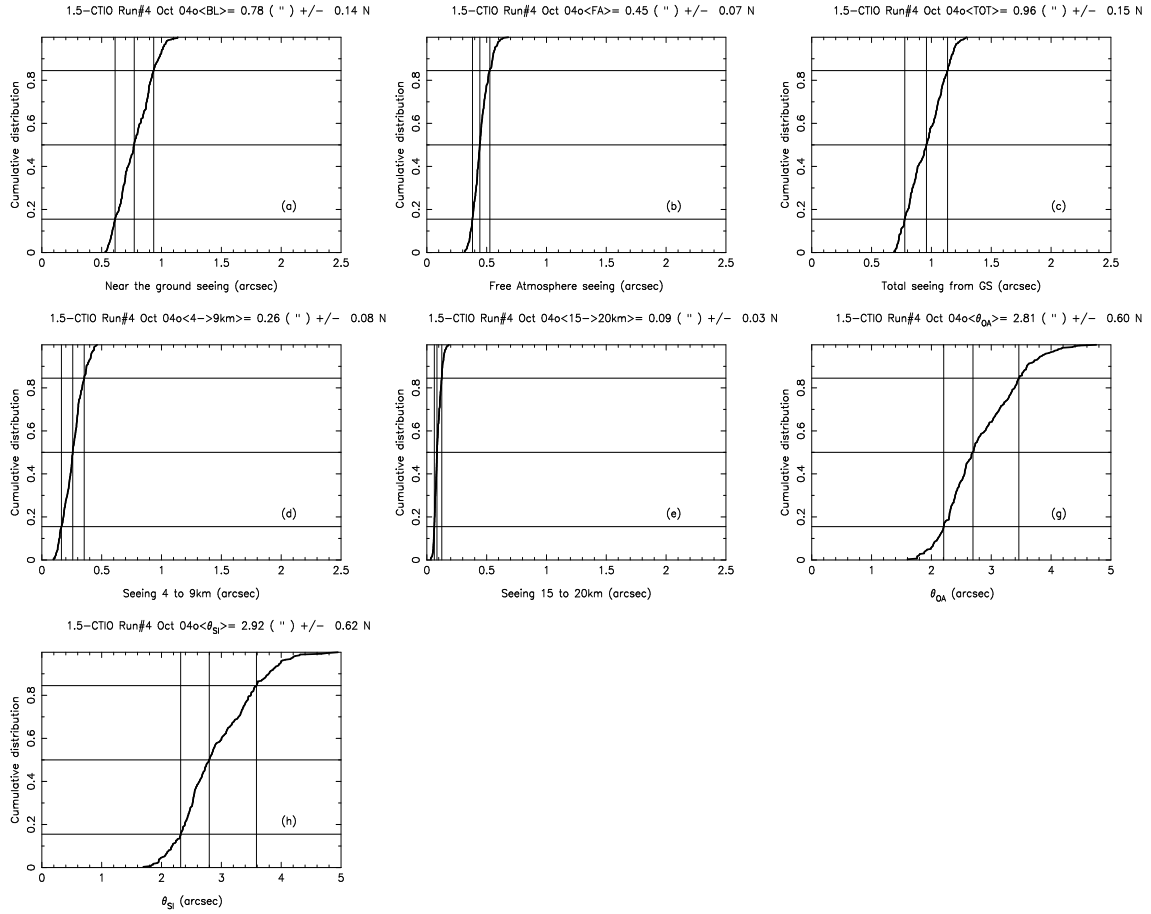


FIGURE 3.7: Cumulative probability distribution of (a) near the ground seeing, (b) free atmospheric seeing, (c) total seeing, (d) \int_{4km}^{9km} , (e) \int_{15km}^{20km} , (g) isoplanatic angle for AO and (h) isoplanatic angle for SI.

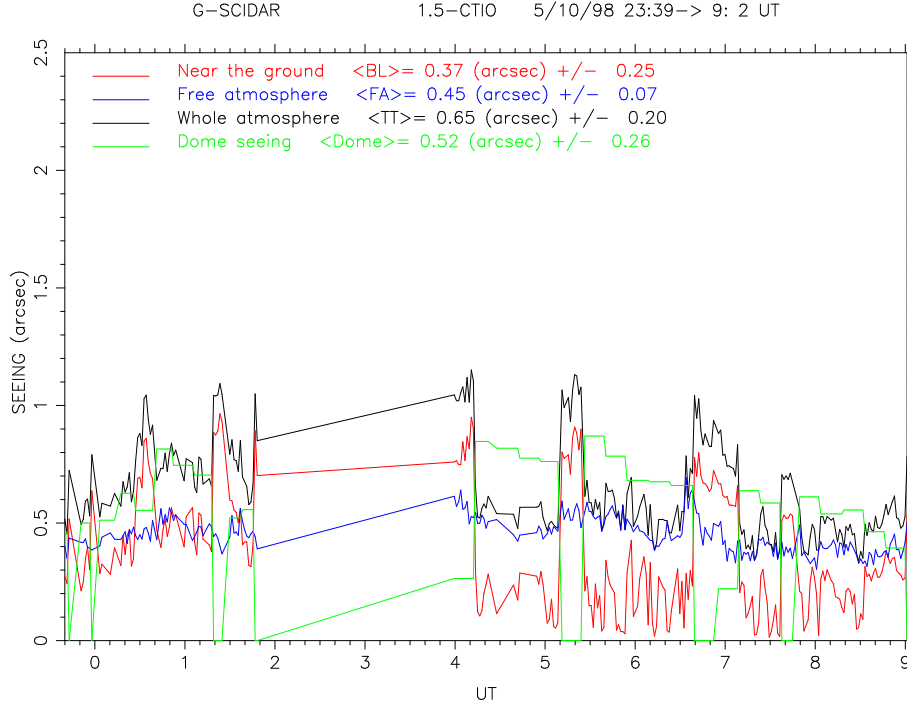


FIGURE 3.8: Temporal evolution of the seeing. Red: Boundary layer (first km); Blue: Free atmosphere (above 1km); Black: Total; Green: dome seeing.(Case D: low altitude layer attributed to Dome seeing).

Dome detection processing

In Figs 3.8 and 3.9 are plotted the temporal evolution of seeing contributions from various slabs of the atmosphere, corresponding respectively to D and A cases. In Fig.3.9 dome seeing is detected without any ambiguity during short periods of the night, for example around 6 UT, with a major contribution when compared to the rest of the time. It is difficult to imagine that dome seeing gave such a large contribution during such a small amount of time. The situation represented in Fig.3.8 seems much more realistic, since the influence of the dome lasts for longer time periods. But one can wonder if, when only one low-altitude, low-speed layer is detected, we give a too large contribution to dome, underestimating the boundary layer effect. This is an argument to assume that **D** processing overestimates the dome influence and that **A** processing underestimates the dome influence.

In Figs 3.10 and 3.11 are given, for the same night, the evolution of the equivalent velocity v and τ for both adaptive optics and speckle interferometry, as defined by the equations given in chapter 1. When zero, it means that no evaluation is available. To our knowledge, it is the first time that a continuous assessment of those variables appears in the litterature.

In next Fig. 3.12 are plotted quality parameters of the method we used to dome seeing detection.

For each night it is also possible to have an overview of the whole night throughout the plot of the cumulative distribution of integrated variables, such as seeing in the various atmospheric slabs and dome, θ_{AO} and θ_{SI} , v_{AO} , v_{SI} , τ_{AO} and τ_{SI} ,

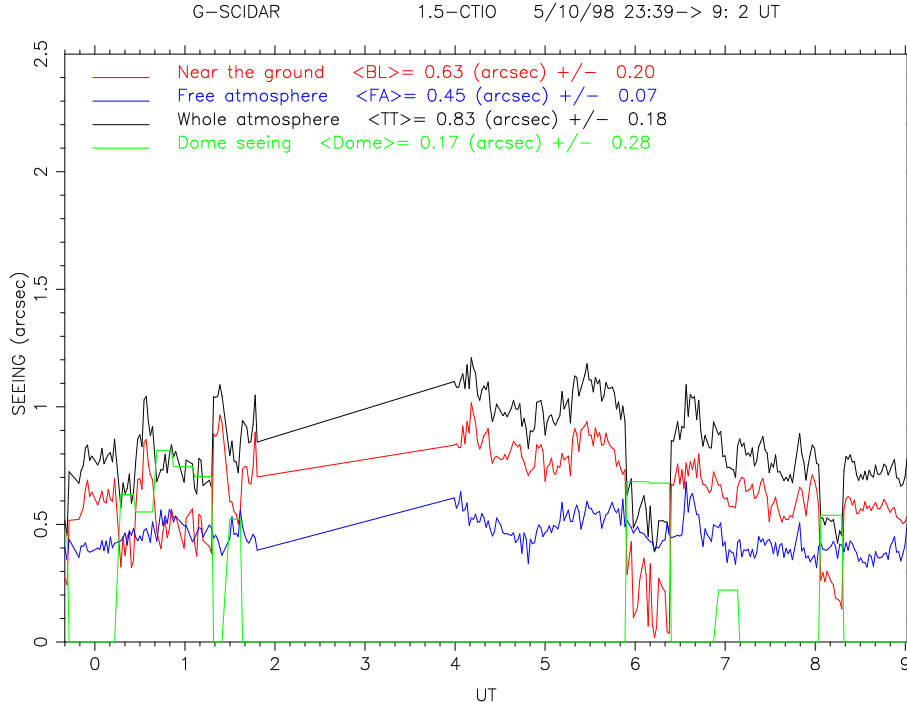


FIGURE 3.9: Temporal evolution of the seeing. Red: Boundary layer (first km); Blue: Free atmosphere (above 1km); Black: Total; Green: dome seeing.(Case A: low altitude layer attributed to boundary layer).

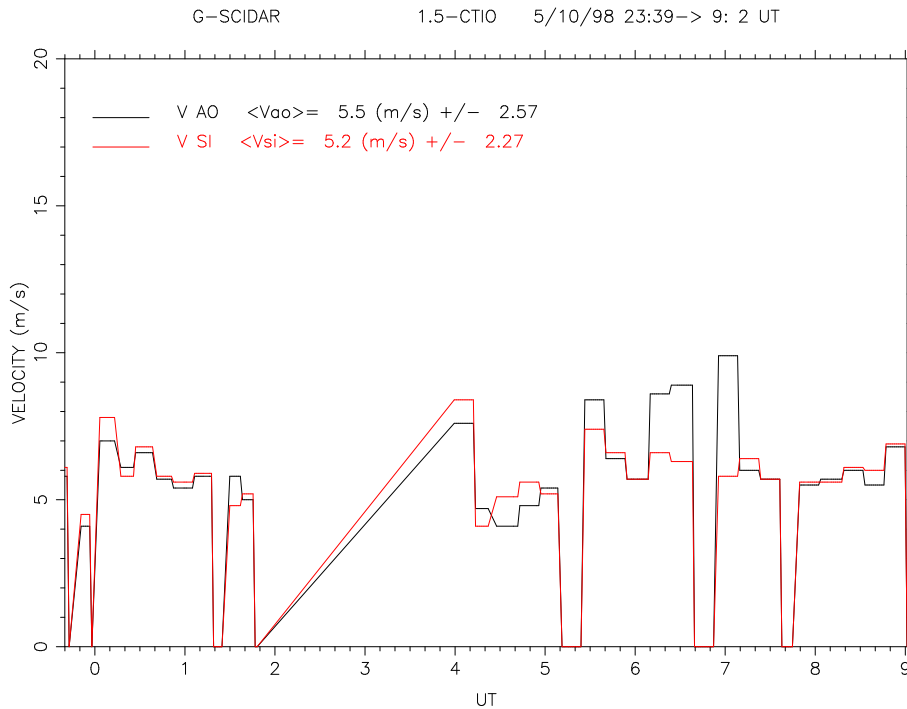


FIGURE 3.10: Temporal evolution of the equivalent speed. Black: for adaptive optics; Red: for speckle interferometry.

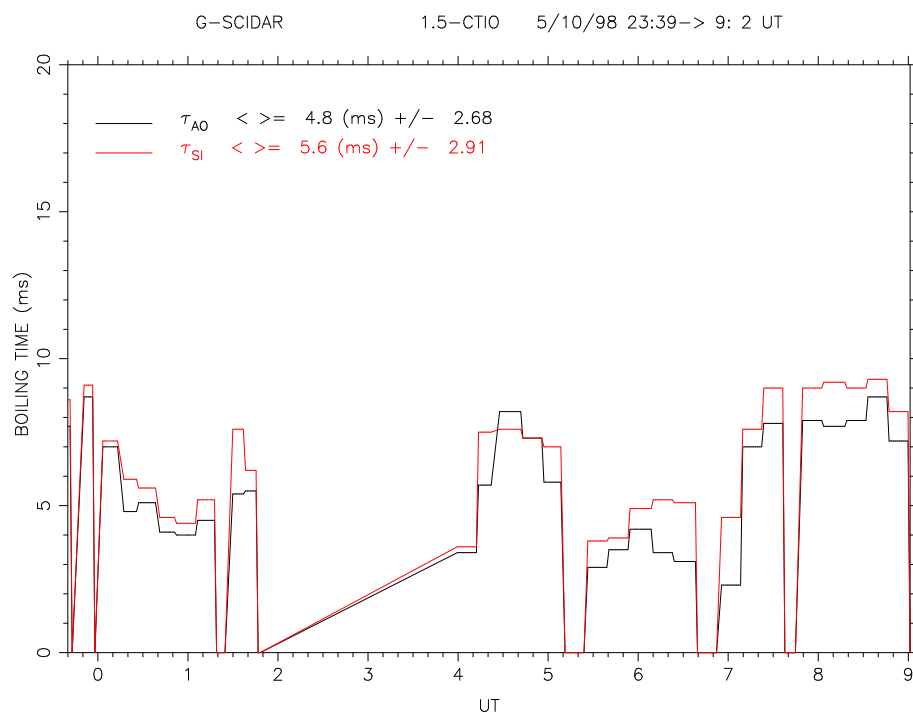


FIGURE 3.11: Temporal evolution of the coherence time. Black: for adaptive optics; Red: for speckle interferometry.

computed with algorithm D. as it appears in Fig. 3.13. In the label of each figure we included the mean value of the relevant integrated variable.

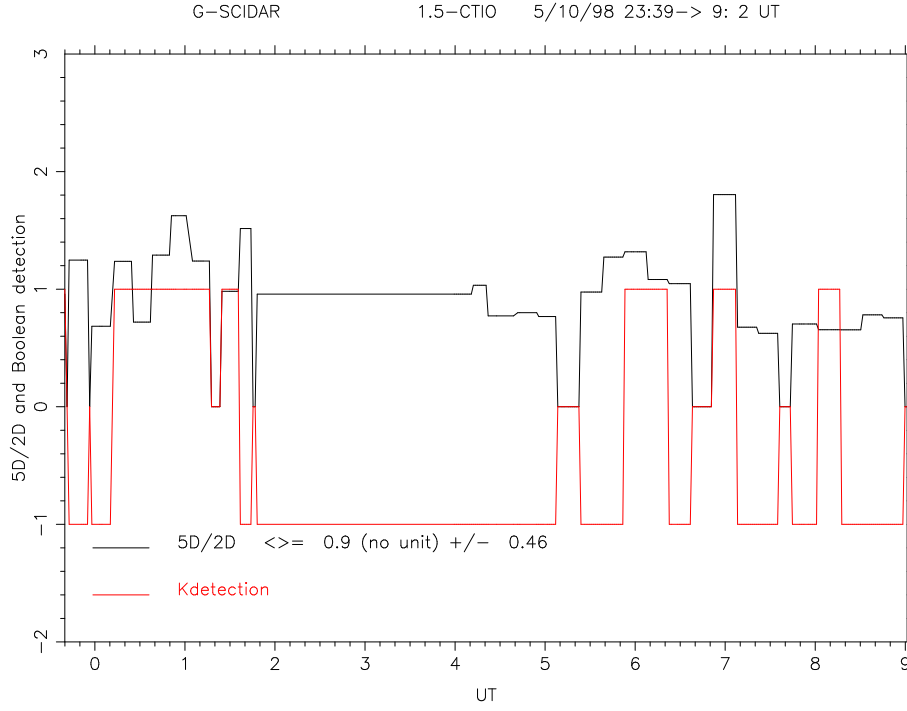


FIGURE 3.12: Temporal evolution of the ratio between $\int C_N^2(h)dh$ issued by the “normal” and the “dome detection” processing. In other words, a ratio of 1 means that all the detected turbulent layers with the spatio-angular, the spatio-temporal angular method accounts for the same amount of optical turbulence detected with the “normal” method (black). In red is given our criterion of detection: 1 means that at least two layers have been detected, at low altitude, but with separated velocities; 0 means that no dome seeing is detected; -1 means that only one low-altitude, low-speed layer is detected.

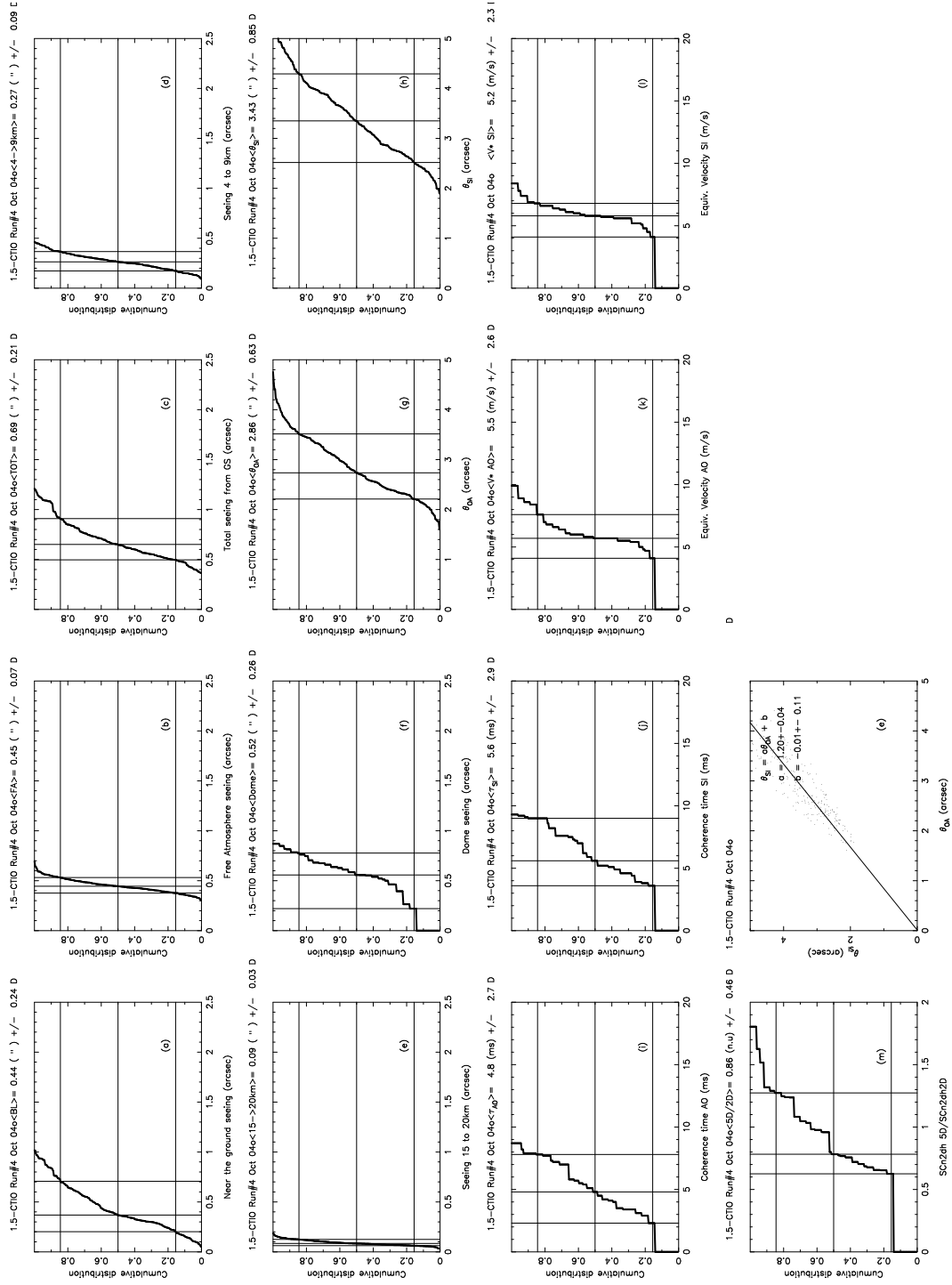


FIGURE 3.13: Cumulative distribution of seeing in various slabs of the atmosphere: (a) first km, (b) above first km, (c) total atmosphere, (d) from 4km up to 9km, (e) from 15 to 20km, (f) dome seeing, (g) θ_{AO} , (h) θ_{SI} , (i) τ_{AO} , (j) τ_{SI} , (k) v_{AO} , (l) v_{SI} , (m) detection quality and (n) θ_{AO} versus θ_{SI} .

3.1.2 Statistics over each one-week run

Normal processing (N)

For each run we computed the cumulative probability distribution of the near the ground seeing, the first km, the free atmosphere seeing and the total seeing. The cumulative distribution of the AO isoplanatic angle is also shown along with its comparison with the SI isoplanatic angle.

As seen in Fig. 3.14 there is a large difference between the median and the average profile. This is due to the fact that the distribution of C_N^2 , at each altitude h , is log-normal with a large skewness. Most of the time the optical turbulence is very low, whereas, from time to time, it can be very strong. The phenomenon is intermitent. This is also visible in Fig. 3.15 where the distribution seems non symmetrical in (a), (b) and (c).

Then are plotted the same figures for run 2, 3 and 4: Fig. 3.16, Fig. 3.17, Fig. 3.18, Fig. 3.19, Fig. 3.20, Fig. 3.21.

These results are summerized in Table 3.2.

TABLE 3.2: Résumé of each G-Scidar run; Normal processing (N).

Run	Month	BL+Dome seeing	FA seeing	Total	θ_{AO}
01	January	0.84	0.49	1.04	2.20
02	April	0.77	0.52	0.99	1.87
03	July	0.87	0.85	1.34	1.43
04	October	0.74	0.47	0.94	2.50
All	run	0.80	0.56	1.06	2.14

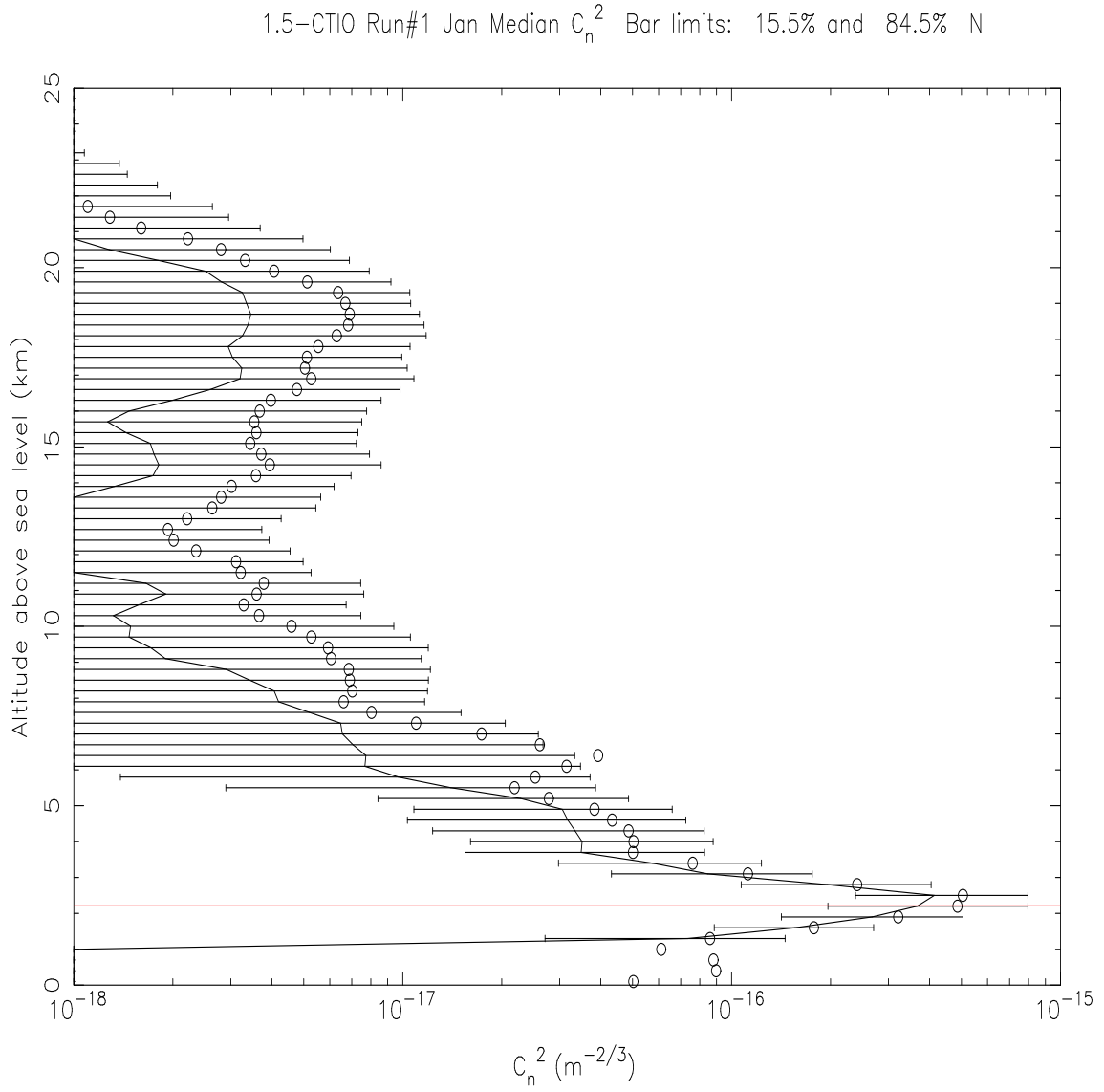


FIGURE 3.14: $C_n^2(h)$ profile averaged over the 6 nights of the first run, January 1998. Line: median, circles: average profile. The red line refers to the Cerro Tololo altitude.

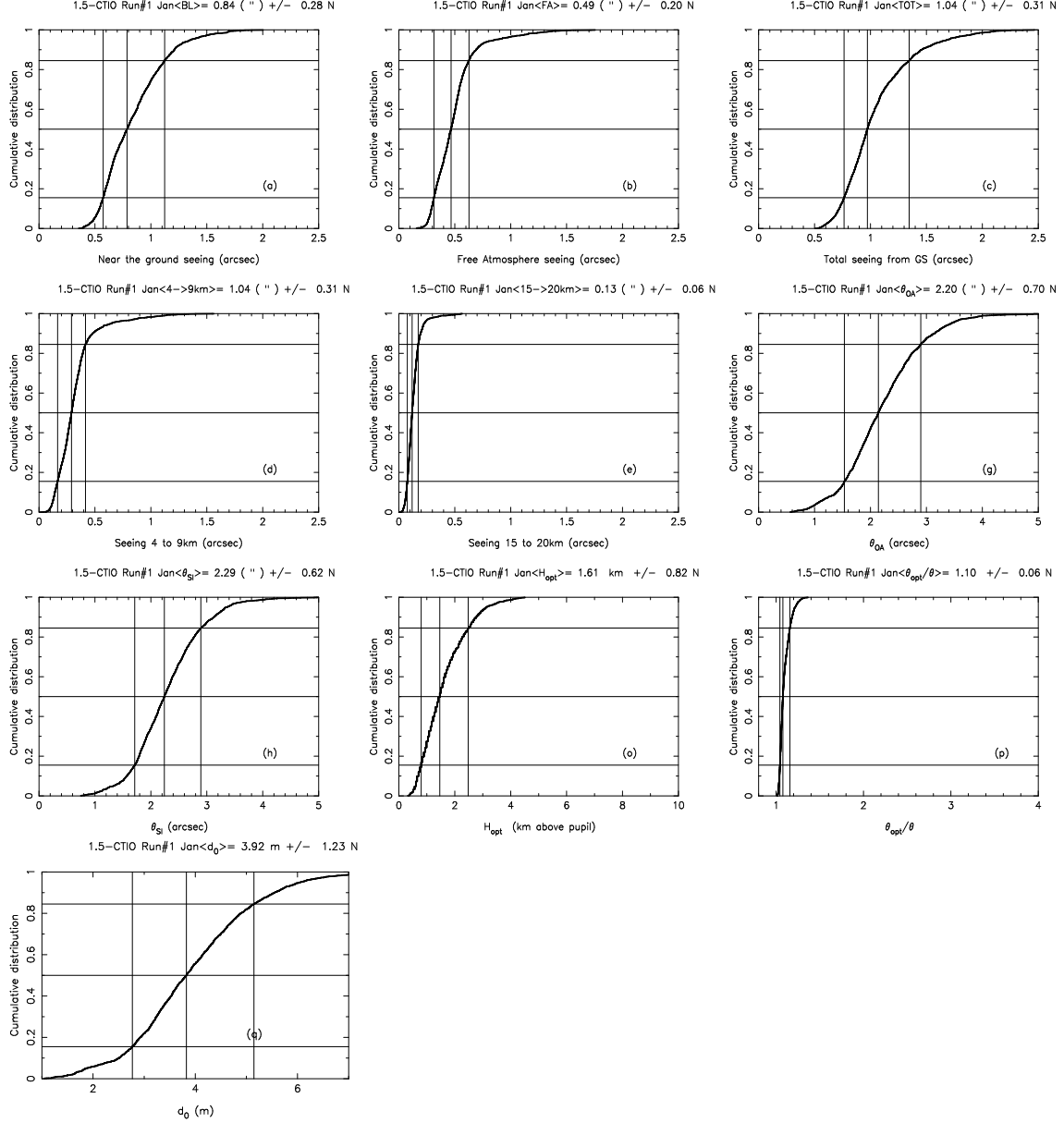


FIGURE 3.15: Cumulative probability distribution of (a) near the ground seeing, (b) free atmospheric seeing, (c) total seeing, (d) \int_{4km}^{9km} , (e) \int_{15km}^{20km} , (g) isoplanatic angle for AO, (h) isoplanatic angle for SI, (i) h_{opt} , (p) θ_{opt}/θ , and (q) the cone effect d_0 . First run, January 1998.

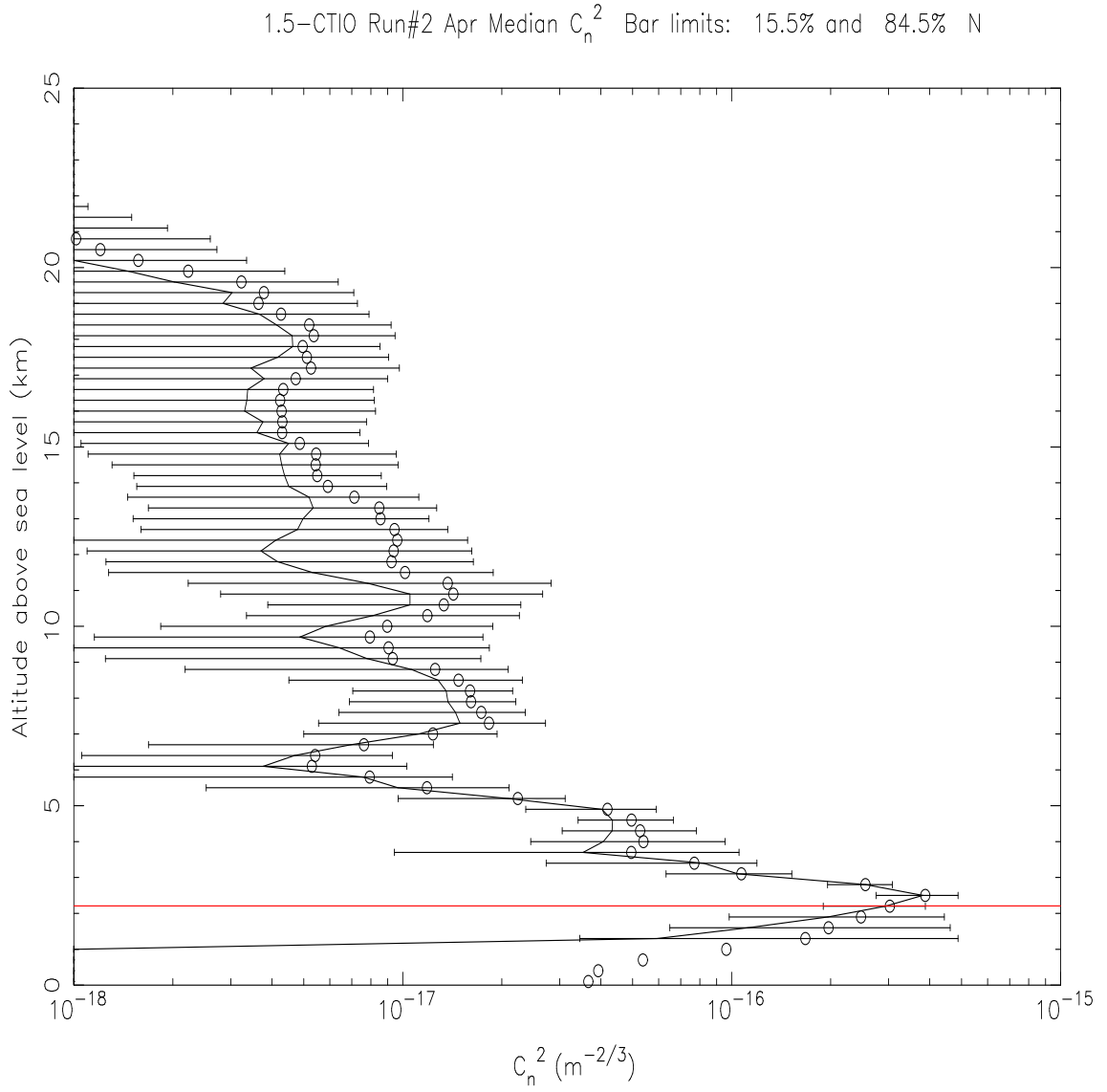


FIGURE 3.16: $C_n^2(h)$ profile averaged over the 2 nights of the second run, April 1998. Line: median, circles: average profile. The red line refers to the Cerro Tololo altitude.

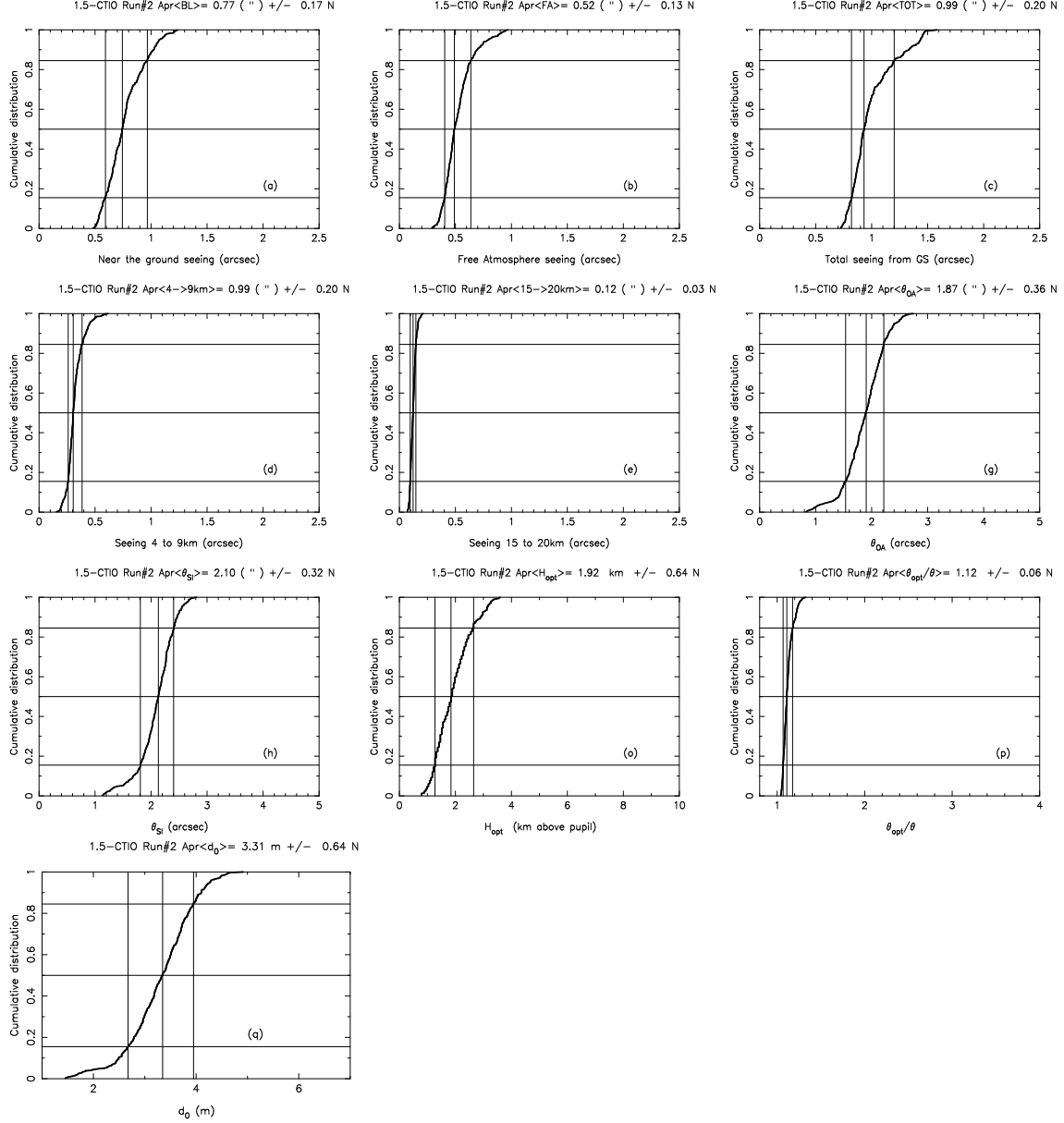


FIGURE 3.17: Cumulative probability distribution of (a) near the ground seeing, (b) free atmospheric seeing, (c) total seeing, (d) \int_{4km}^{9km} , (e) \int_{15km}^{20km} , (g) isoplanatic angle for AO, (h) isoplanatic angle for SI, (o) h_{opt} , (p) θ_{opt}/θ , and (q) the cone effect d_0 . Second run, April 1998.

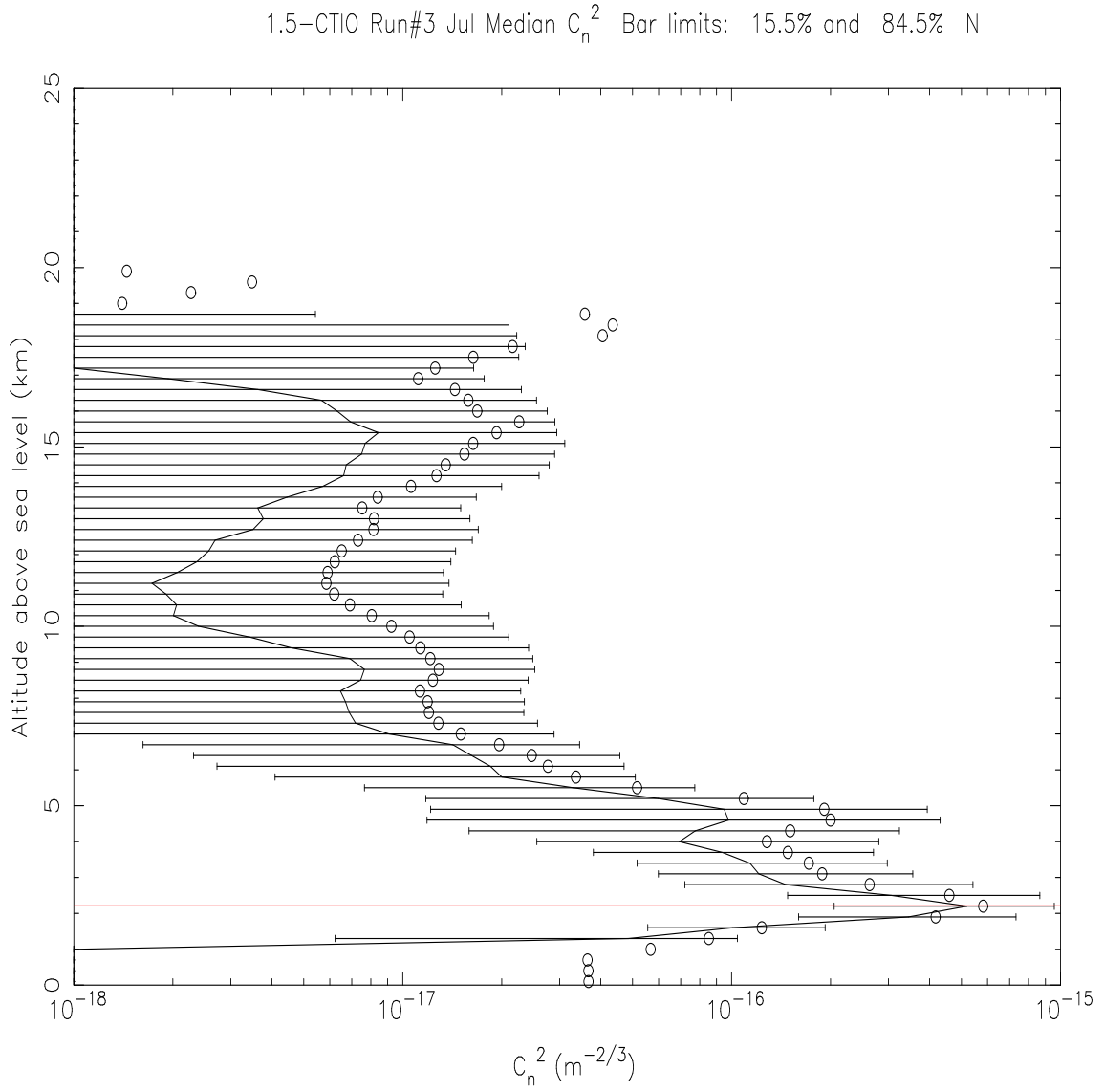


FIGURE 3.18: $C_n^2(h)$ profile averaged over the 6 nights of the third run, July 1998. Line: median, circles: average profile. The red line refers to the Cerro Tololo altitude.

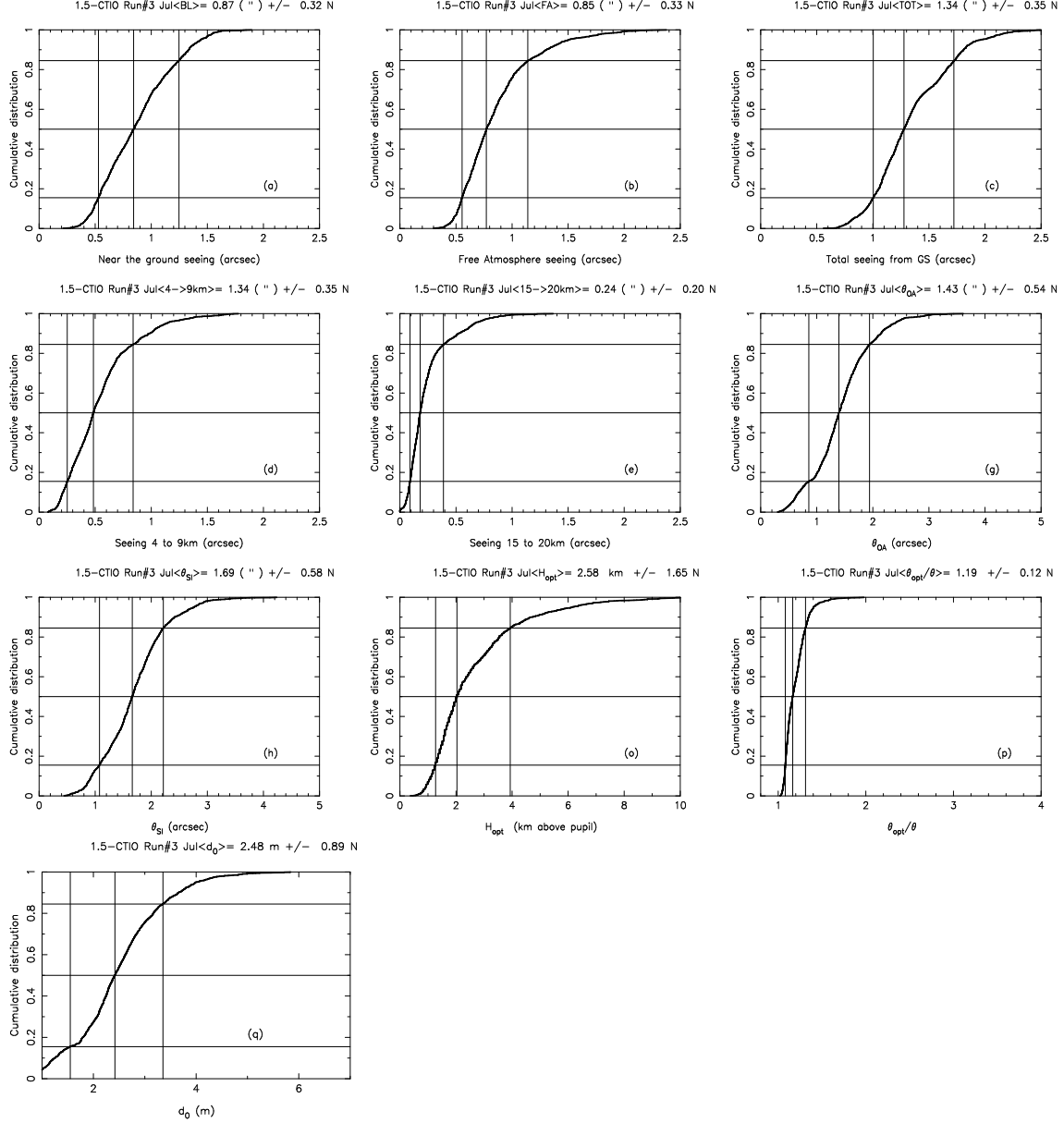


FIGURE 3.19: Cumulative probability distribution of (a) near the ground seeing, (b) free atmospheric seeing, (c) total seeing, (d) \int_{4km}^{9km} , (e) \int_{15km}^{20km} , (g) isoplanatic angle for AO, (h) isoplanatic angle for SI, (i) h_{opt} , (p) θ_{opt}/θ , and (q) the cone effect d_0 . Third run, July 1998.

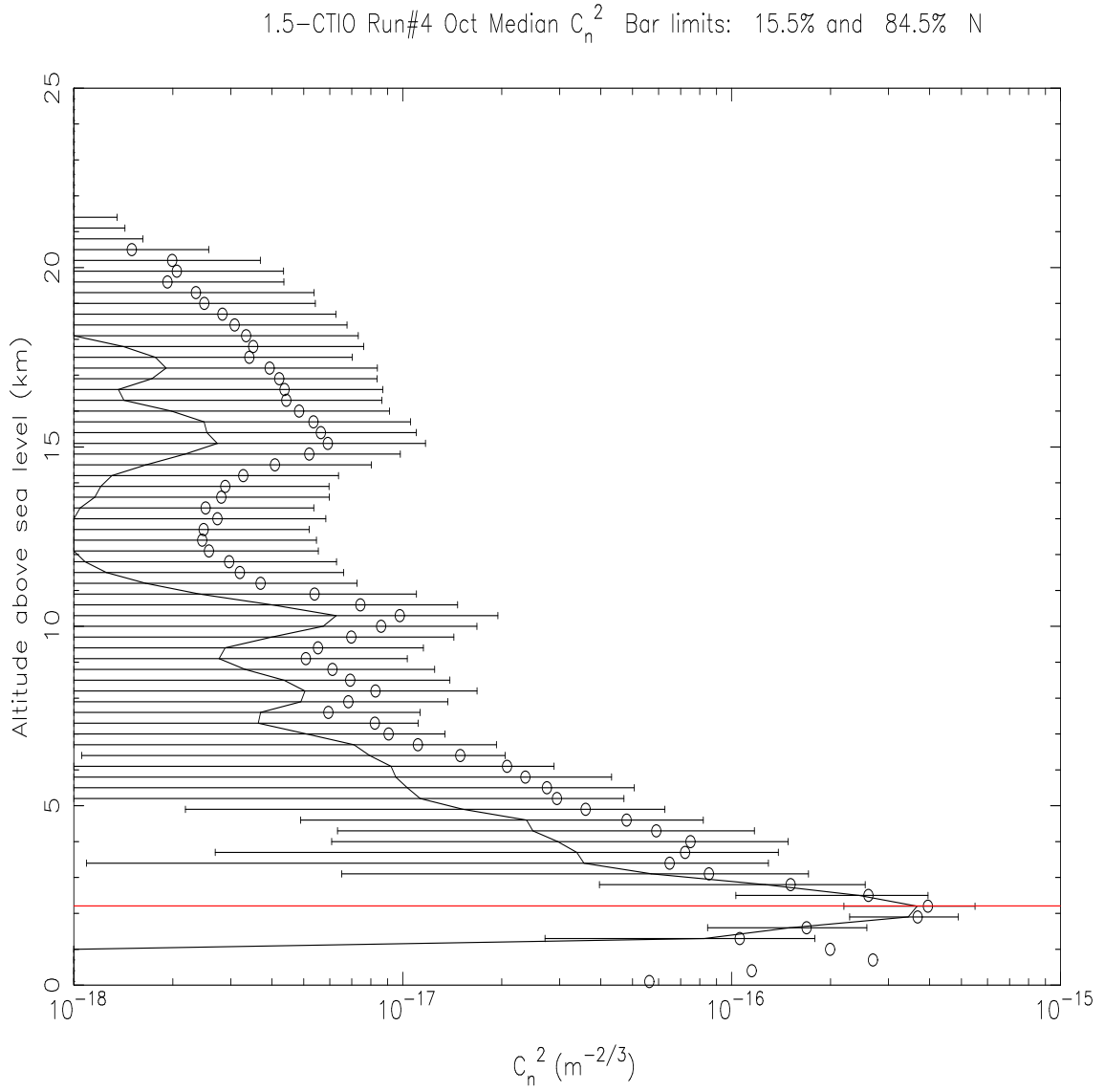


FIGURE 3.20: $C_n^2(h)$ profile averaged over the 8 nights of the fourth run, October 1998. Line: median, circles: average profile. The red line refers to the Cerro Tololo altitude.

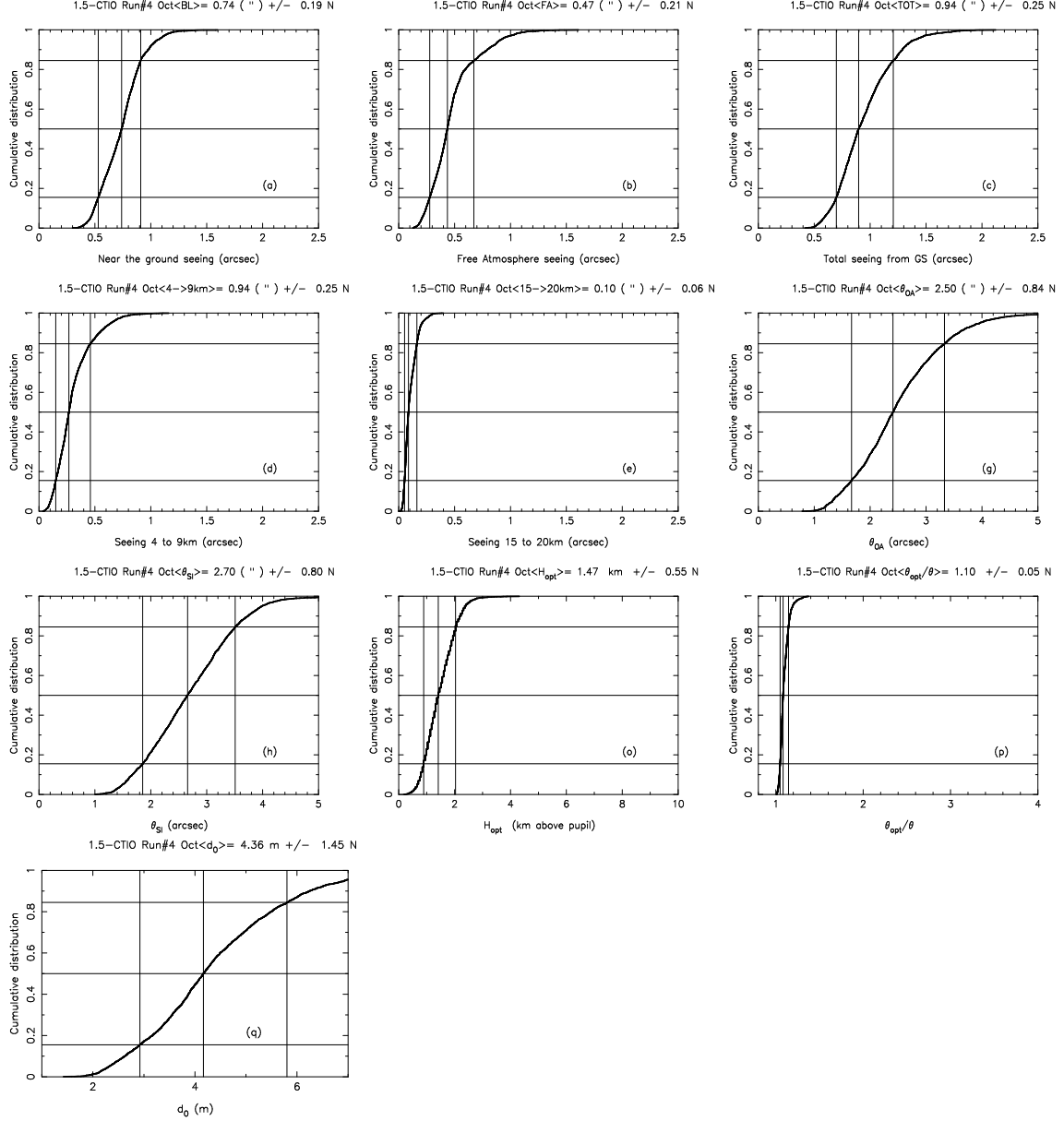


FIGURE 3.21: Cumulative probability distribution of (a) near the ground seeing, (b) free atmospheric seeing, (c) total seeing, (d) \int_{4km}^{9km} , (e) \int_{15km}^{20km} , (g) isoplanatic angle for AO, (h) isoplanatic angle for SI, (o) h_{opt} , (p) θ_{opt}/θ , and (q) the cone effect d_0 . Fourth run, October 1998.

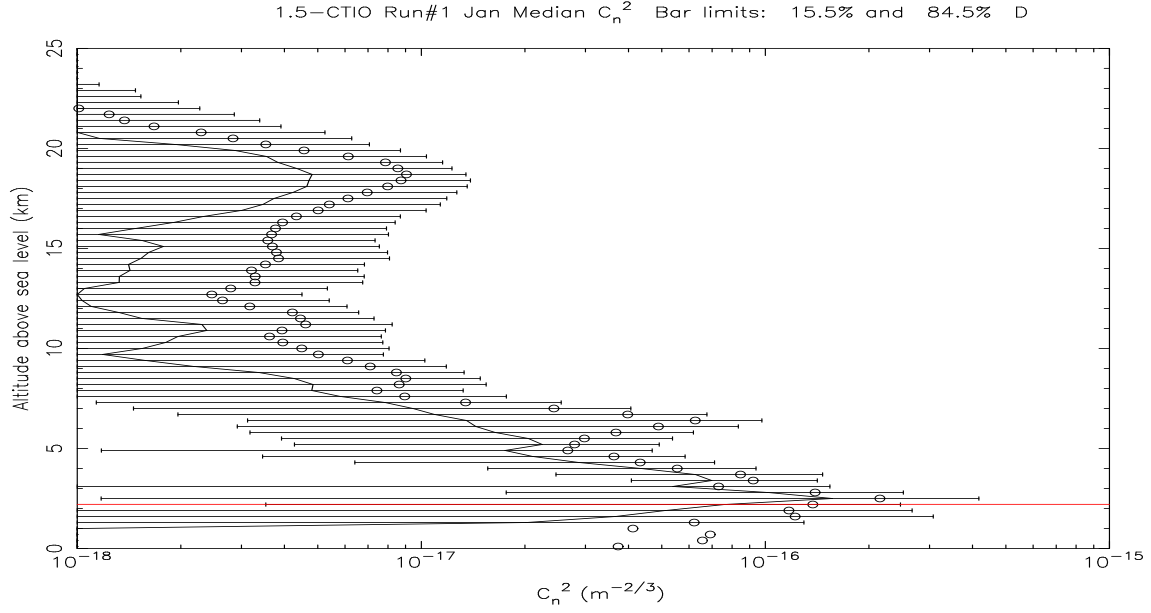


FIGURE 3.22: GS $C_n^2(h)$ profile averaged over the 6 nights of the first run, January 1998. Line: median, circles: average profile. The red line refers to the Cerro Tololo altitude. Dome seeing has been substracted.

Dome detection processing

If we take into account the dome contribution and exclude it, the corresponding C_n^2 averaged profiles are plotted in the following Figs 3.22, 3.23, 3.24 and 3.25. The respective cumulative distribution are given in Figs 3.26, 3.27, 3.28 and 3.29. As both cases D and A give very similar results, we opted to show only case D.

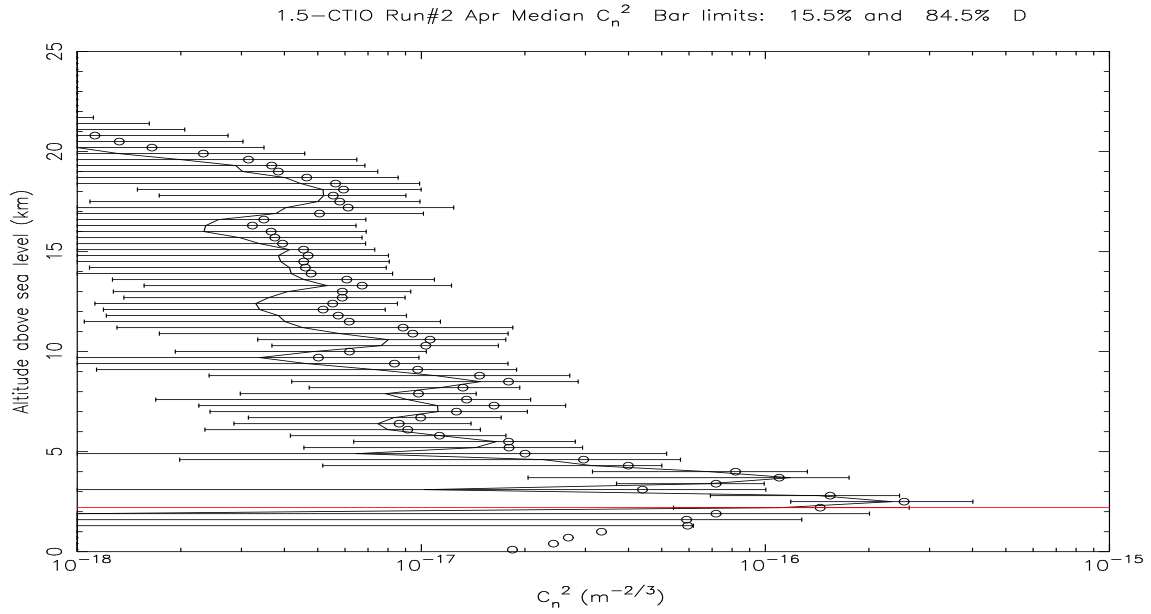


FIGURE 3.23: GS $C_n^2(h)$ profile averaged over the 2 nights of the second run, April 1998. Line: median, circles: average profile. The red line refers to the Cerro Tololo altitude. Dome seeing has been subtracted.

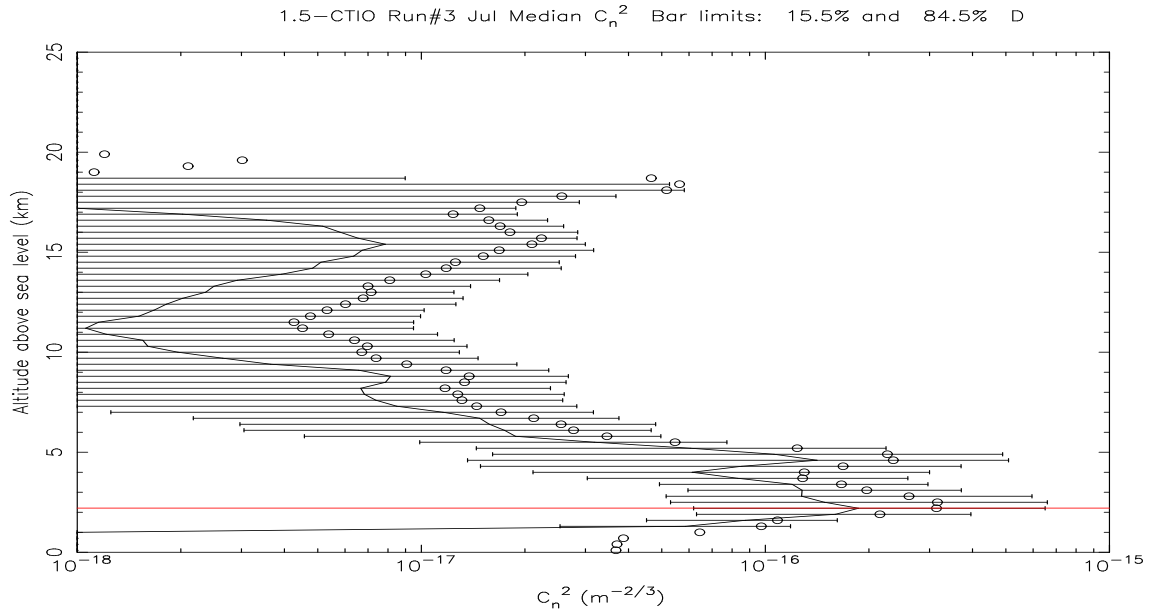


FIGURE 3.24: GS $C_n^2(h)$ profile averaged over the 6 nights of the third run, July 1998. Line: median, circles: average profile. The red line refers to the Cerro Tololo altitude. Dome seeing has been subtracted.

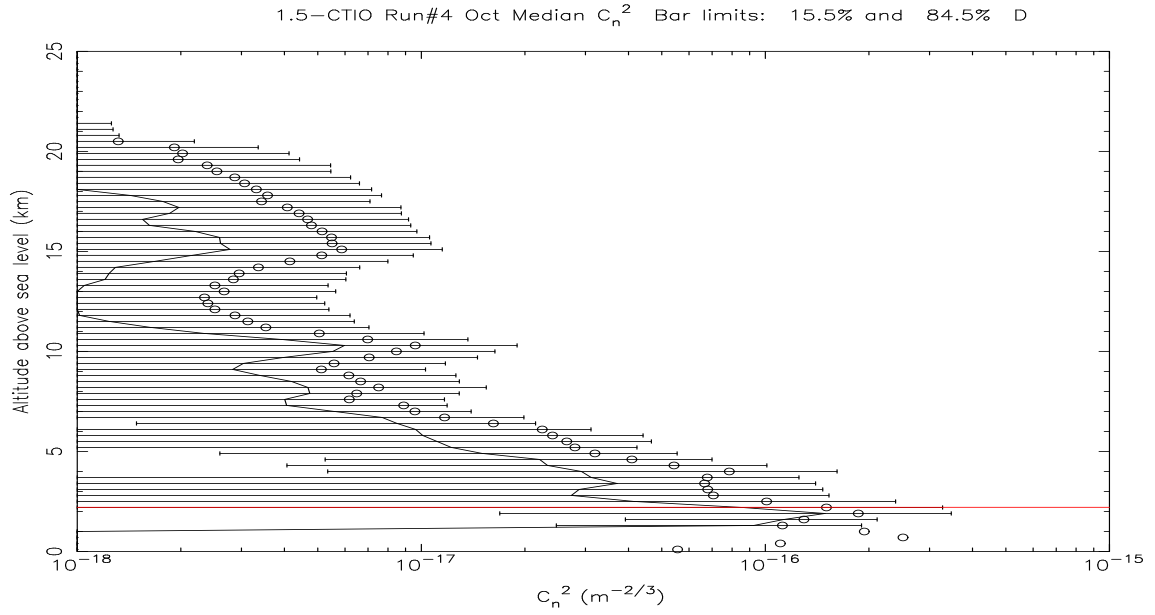


FIGURE 3.25: GS $C_n^2(h)$ profile averaged over the 8 nights of the fourth run, October 1998. Line: median, circles: average profile. The red line refers to the Cerro Tololo altitude. Dome seeing has been subtracted.

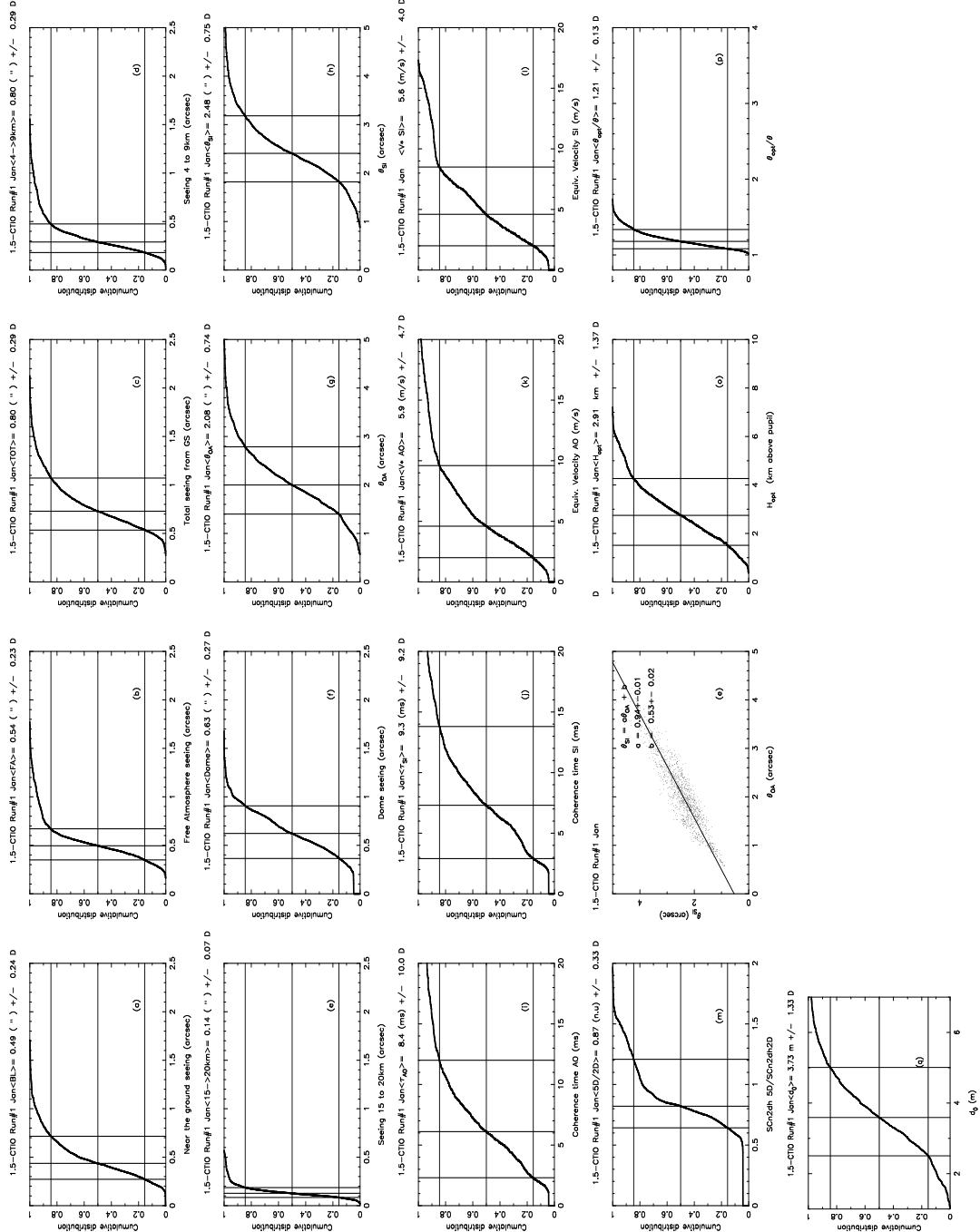


FIGURE 3.26: Cumulative distribution of seeing in various slabs of the atmosphere: (a) first km, (b) above first km, (c) total atmosphere, (d) from 4km (ASL) up to 9km, (e) from 15 (ASL) to 20km, (f) dome seeing, (g) θ_{AO} , (h) θ_{SI} , (i) τ_{AO} , (j) τ_{SI} , (k) v_{AO} , (l) v_{SI} , (m) detection quality, (n) θ_{AO} versus θ_{SI} , (o) h_{opt} , (p) θ_{opt}/θ and (q) d_0 . First run, January 1998.

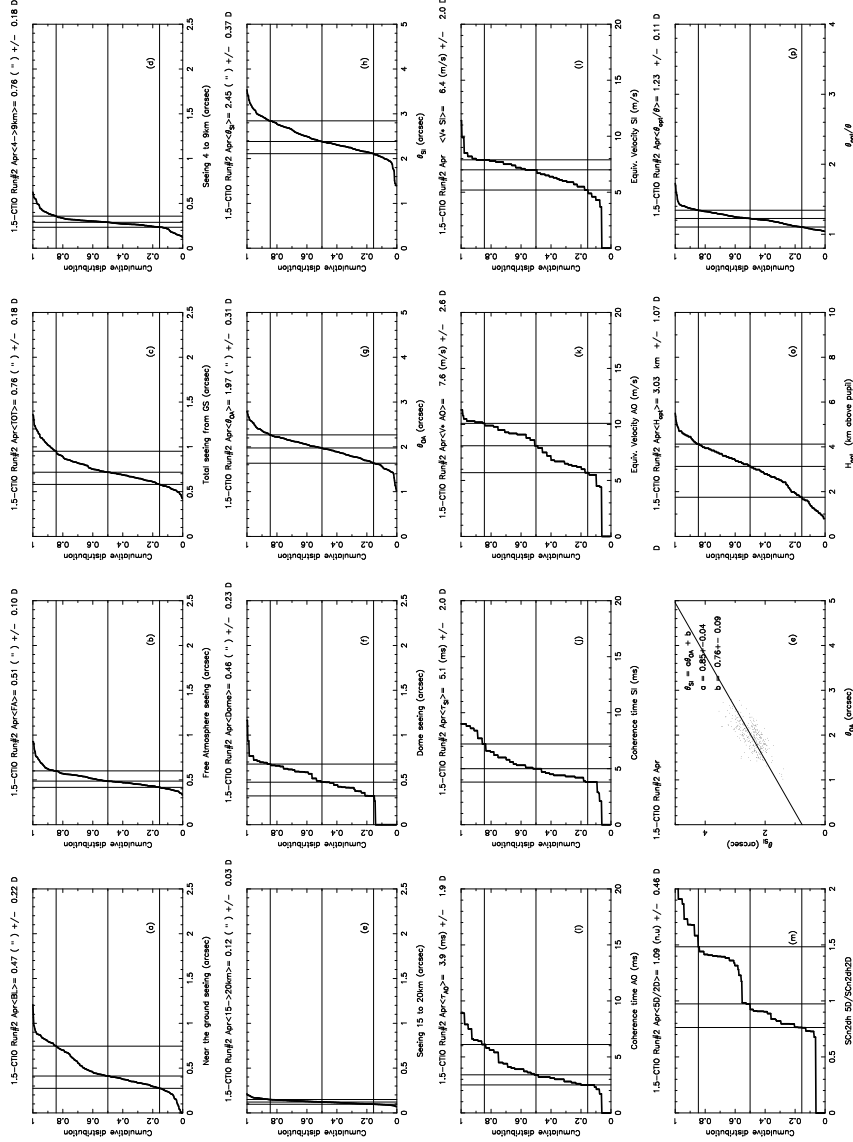


FIGURE 3.27: Cumulative distribution of seeing in various slabs of the atmosphere: (a) first km, (b) above first km, (c) total atmosphere, (d) from 4km (ASL) up to 9km, (e) from 15 (ASL) to 20km, (f) dome seeing, (g) θ_{AO} , (h) θ_{SI} , (i) τ_{AO} , (j) τ_{SI} , (k) v_{AO} , (l) v_{SI} , (m) detection quality, (n) θ_{AO} versus θ_{SI} , (o) h_{opt} , (p) θ_{opt}/θ and (q) d_0 . Second run, April 1998.

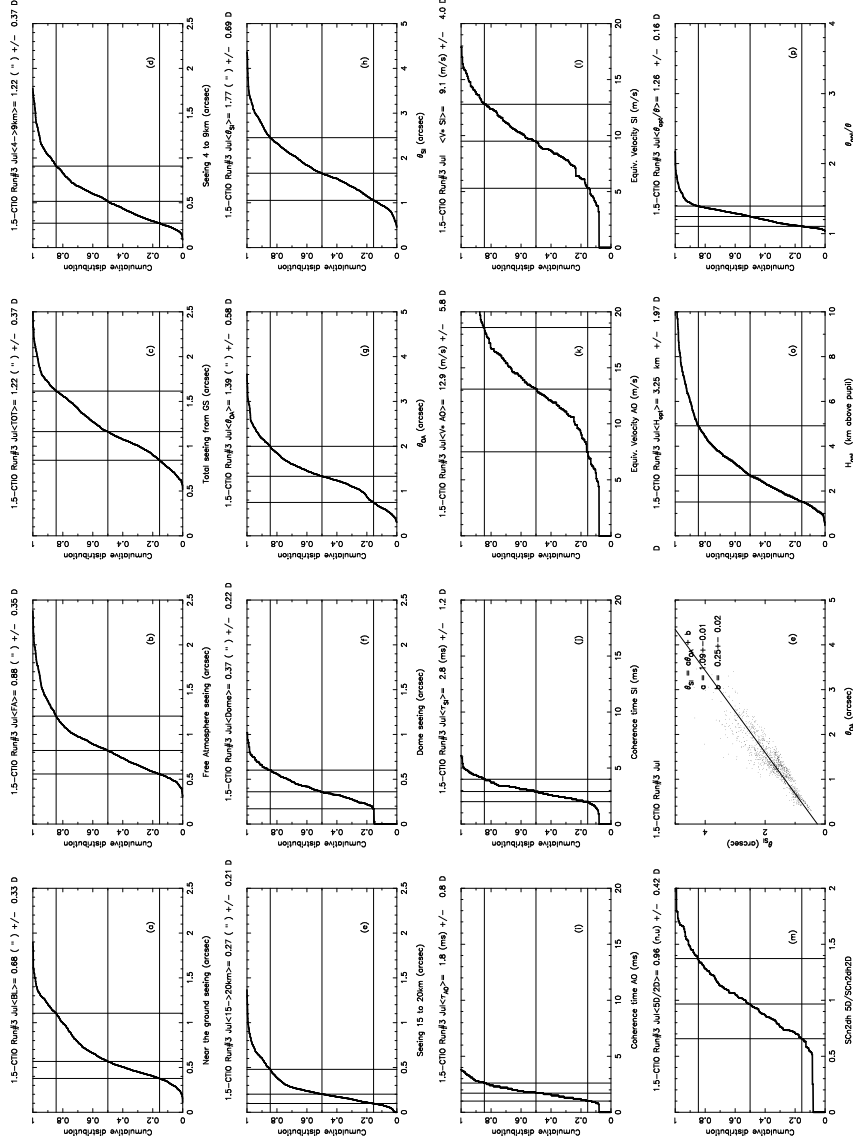


FIGURE 3.28: Cumulative distribution of seeing in various slabs of the atmosphere: (a) first km, (b) above first km, (c) total atmosphere, (d) from 4km (ASL) up to 9km, (e) from 15 (ASL) to 20km, (f) dome seeing, (g) θ_{AO} , (h) θ_{SI} , (i) τ_{AO} , (j) τ_{SI} , (k) v_{AO} , (l) v_{SI} , (m) detection quality, (n) θ_{AO} versus θ_{SI} , (o) h_{opt} , (p) θ_{opt}/θ and (q) d_0 . Third run, July 1998.

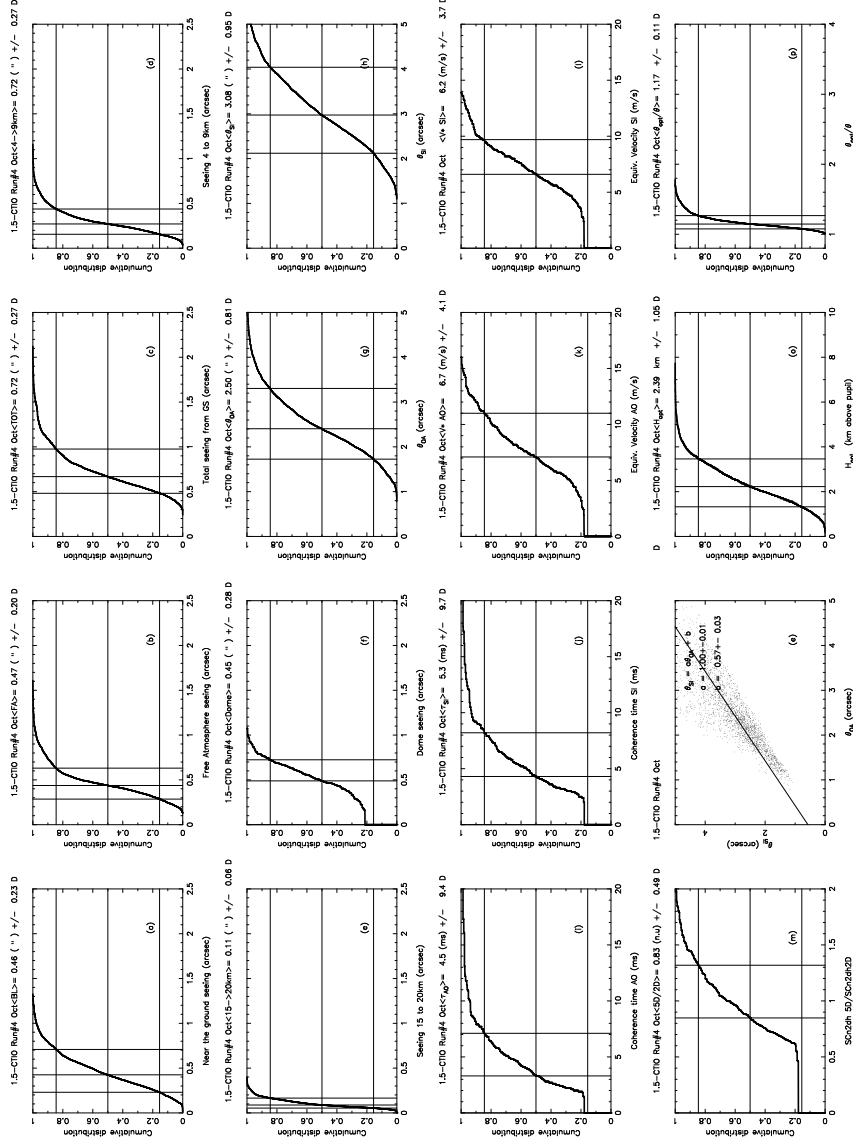


FIGURE 3.29: Cumulative distribution of seeing in various slabs of the atmosphere: (a) first km, (b) above first km, (c) total atmosphere, (d) from 4km (ASL) up to 9km, (e) from 15 (ASL) to 20km, (f) dome seeing, (g) θ_{AO} , (h) θ_{SI} , (i) τ_{AO} , (j) τ_{SI} , (k) v_{AO} , (l) v_{SI} , (m) detection quality, (n) θ_{AO} versus θ_{SI} , (o) h_{opt} , (p) θ_{opt}/θ and (q) d_0 . Fourth run, October 1998.

In Table 3.3, one can see a résumé of each four runs for what concern the seeing in the first km (BL), above the first km (FA) and the dome at the 1.5m Tololo telescope. For the assessment of BL, total atmosphere and dome we wrote a lower and upper limit which have been issued through cases (D) and (A). The FA contribution comes from the normal processing (N). The first column shows the contribution of BL + 1.5m Dome optical turbulence given by the normal processing.

TABLE 3.3: Résumé of G-Scidar seeing measurements for each run and for the whole campaign.

Run	BL+D	BL	BL	FA	Atmos.	Atmos.	Dome	Dome
Case	N	inf.	sup.	N	inf.	sup.	sup.	inf.
unit	arcsec	D	A	arcsec	D	A	D	A
01 Jan	0.84	0.49	0.53	0.49	0.80	0.83	0.63	0.57
02 Apr	0.77	0.47	0.49	0.52	0.76	0.78	0.46	0.44
03 Jul	0.87	0.68	0.68	0.85	1.22	1.23	0.37	0.36
04 Oct	0.74	0.46	0.57	0.47	0.72	0.80	0.45	0.28
All	0.80	0.52	0.58	0.56	0.85	0.89	0.48	0.38

In Table 3.4, we summarized all the assessed integrated variables, θ , v , and τ for adaptive optics and speckle interferometry, with the G-Scidar, as given with processing case D.

TABLE 3.4: Résumé of each G-Scidar integrated variables, for each run and for the whole campaign. Normal Dome seeing processing (D).

Run	θ_{AO}	θ_{SI}	v_{AO}	v_{SI}	τ_{AO}	τ_{SI}
Case	D	D	D	D	D	D
unit	arcsec	arcsec	m/s	m/s	ms	ms
01 Jan	2.1	2.5	5.9	5.6	8.2	9.2
02 Apr	2.0	2.5	7.6	6.4	3.9	5.1
03 Jul	1.4	1.8	12.9	9.1	1.8	2.8
04 Oct	2.5	3.1	6.7	6.2	4.2	5.0
All	2.1	2.6	7.9	6.7	4.6	5.6

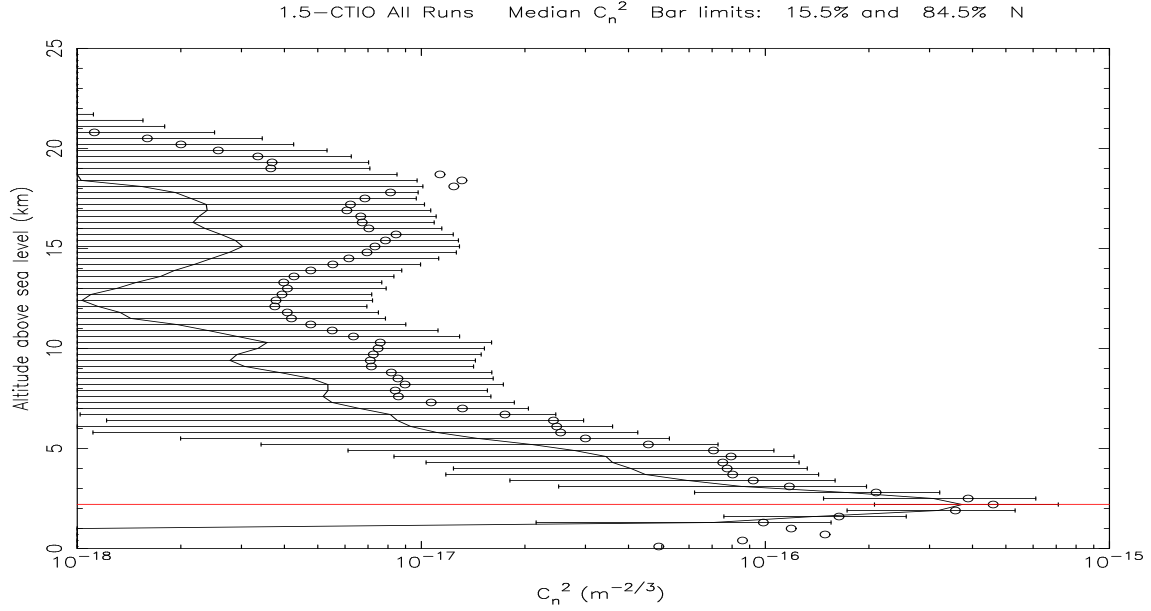


FIGURE 3.30: $C_n^2(h)$ profile averaged over the 22 nights of the whole campaign, 1998. Line: median, circles: average profile. The red line refers to the Cerro Tololo altitude.

3.1.3 All run statistics

Normal processing (N)

As for last section, in Fig. 3.30 and Fig. 3.31 appear statistics over all the measurements done with the G-Scidar which concern the optical turbulence profile and the cumulative distribution.

Dome detection processing

As for last section, in Fig. 3.32 and Fig. 3.33 appear statistics over all the measurements done with the G-Scidar which concern the optical turbulence profile and the cumulative distribution, when dome contribution has been substracted, following case D.

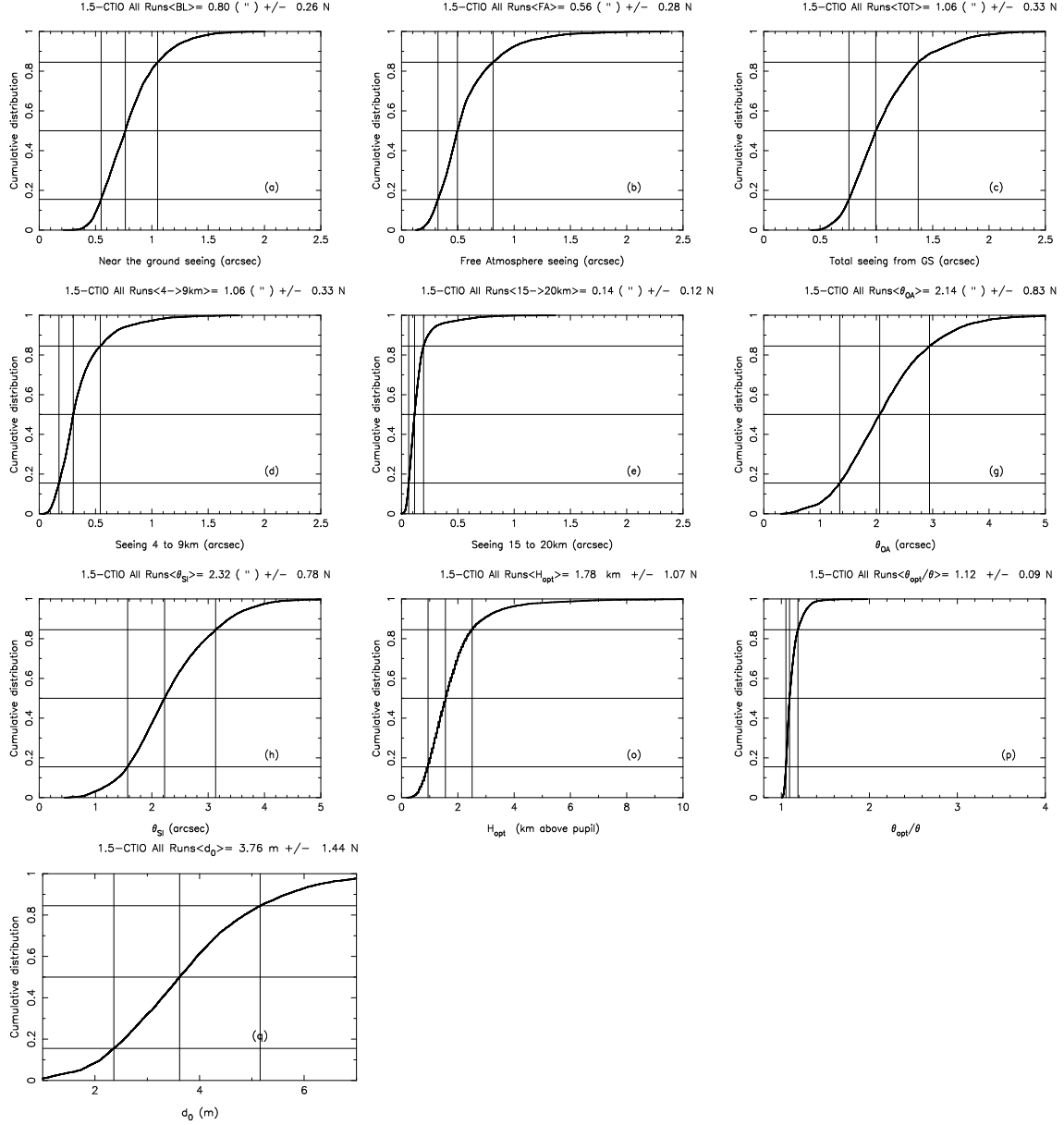


FIGURE 3.31: Cumulative distribution of seeing in various slabs of the atmosphere: (a) first km, (b) above first km, (c) total atmosphere, (d) from 4km (ASL) up to 9km, (e) from 15 (ASL) to 20km, (f) dome seeing, (g) θ_{AO} , (h) θ_{SI} , (i) τ_{AO} , (j) τ_{SI} , (k) v_{AO} , (l) v_{SI} , (m) detection quality, (n) θ_{AO} versus θ_{SI} , (o) h_{opt} , (p) θ_{opt}/θ and (q) d_0 . Whole campaign, 1998.

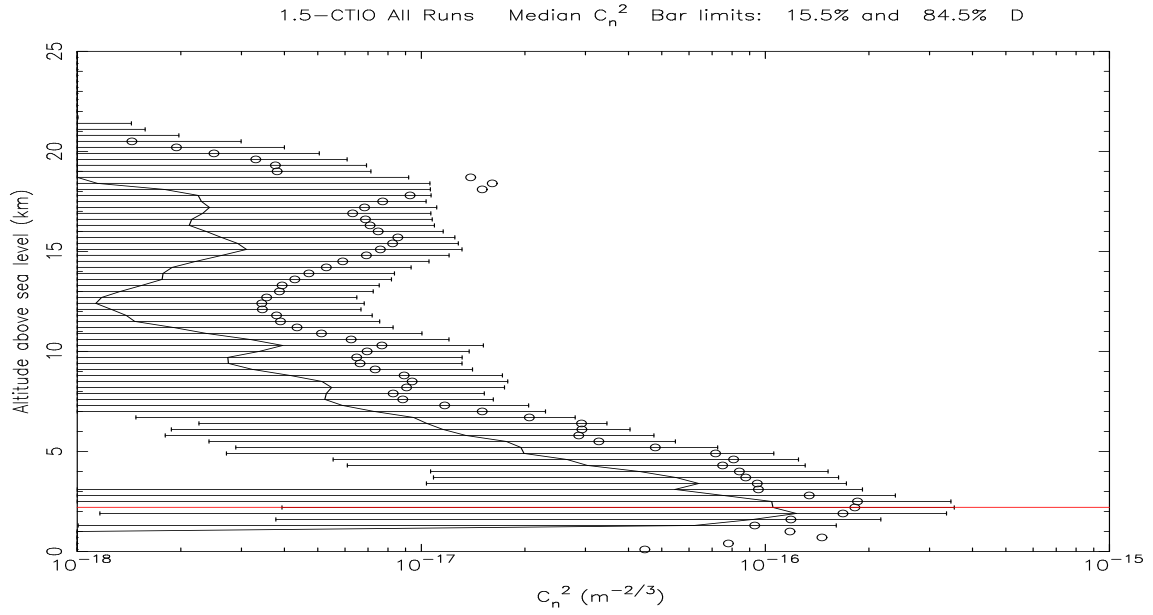


FIGURE 3.32: GS $C_n^2(h)$ profile averaged over the 22 nights of the whole campaign, 1998. Line: median, circles: average profile. The red line refers to the Cerro Tololo altitude. Dome seeing has been subtracted.

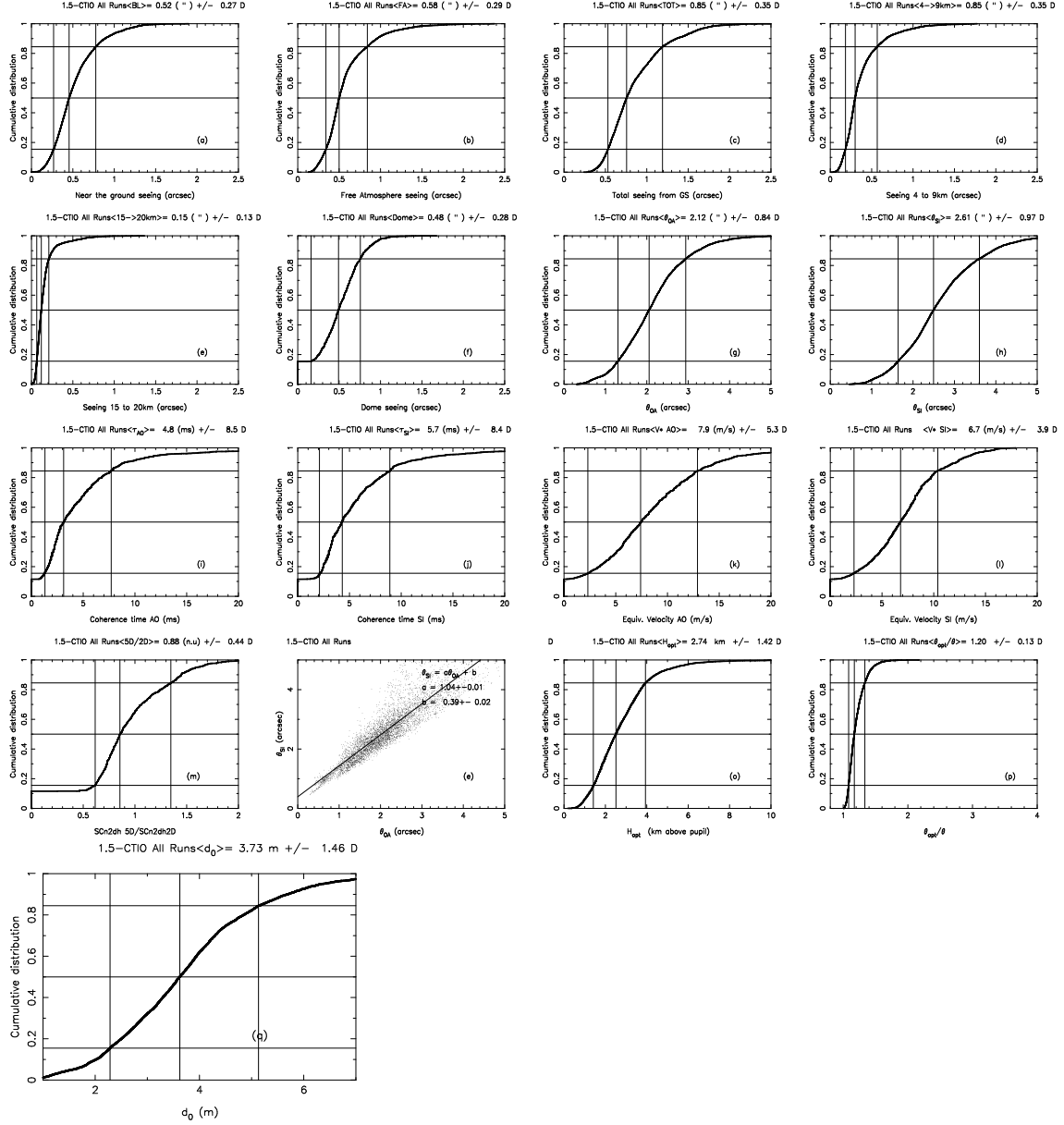


FIGURE 3.33: Cumulative distribution of seeing in various slabs of the atmosphere: (a) first km, (b) above first km, (c) total atmosphere, (d) from 4km (ASL) up to 9km, (e) from 15 (ASL) to 20km, (f) dome seeing, (g) θ_{AO} , (h) θ_{SI} , (i) τ_{AO} , (j) τ_{SI} , (k) v_{AO} , (l) v_{SI} , (m) detection quality, (n) θ_{AO} versus θ_{SI} , (o) h_{opt} , (p) θ_{opt}/θ and (q) d_0 . Whole campaign, 1998.

3.2 GSM

3.2.1 Data Analysis

Table 3.5 shows the summary results obtained during the Pachon mission (from 3 to 10 October 98). The left curves present the temporal evolution of the outer scale \mathcal{L}_0 , seeing ε_0 , isoplanatic angle θ_0 . Each point is corresponding to 2 minute acquisition time measurement taken every 4 minutes. The total data obtained during this mission is 616 measurements which corresponds to 7 to 8 hours of continuous measurements per night. In the same figure histograms of those parameters are given from which one can deduce that most of outer scale data are decametric with a median value of 26.7 m. The observed seeing is generally less than 1 arcsecond with a median value of 0.85 arcsecond. For the isoplanatic angle, the whole measurements are distributed from 1 to 5 arcsecond around a median value of 2.84 arcsec. Nights of 9 and 10 present dispersed and largest outer scale values because the meteorological conditions were bad with a strong wind coming sometimes from the non-protected GSM direction. So, it can not be excluded that this strong wind caused telescope vibrations.

	Mean	Median
ε_0 (as)	0.98	0.85
\mathcal{L}_0 (m)	35.6	26.7
θ_0 (as)	2.9	2.84
$\frac{\sigma_I^2}{\langle I \rangle^2}$ (%)	1.86	1.40

TABLE 3.5: Résumé of GSM results

3.2.2 Night-by-night results

In appendix 7.3.1 of this report are presented for each night results of atmospheric turbulence parameters measured by GSM. On each page, the temporal evolution the outer scale \mathcal{L}_0 , seeing ε_0 , isoplanatic angle θ_0 . Short gaps in the data correspond usually to a change of the observed star, while larger gaps are caused by clouds on partially clear nights. A Table summarizes the main parameters measured with GSM.

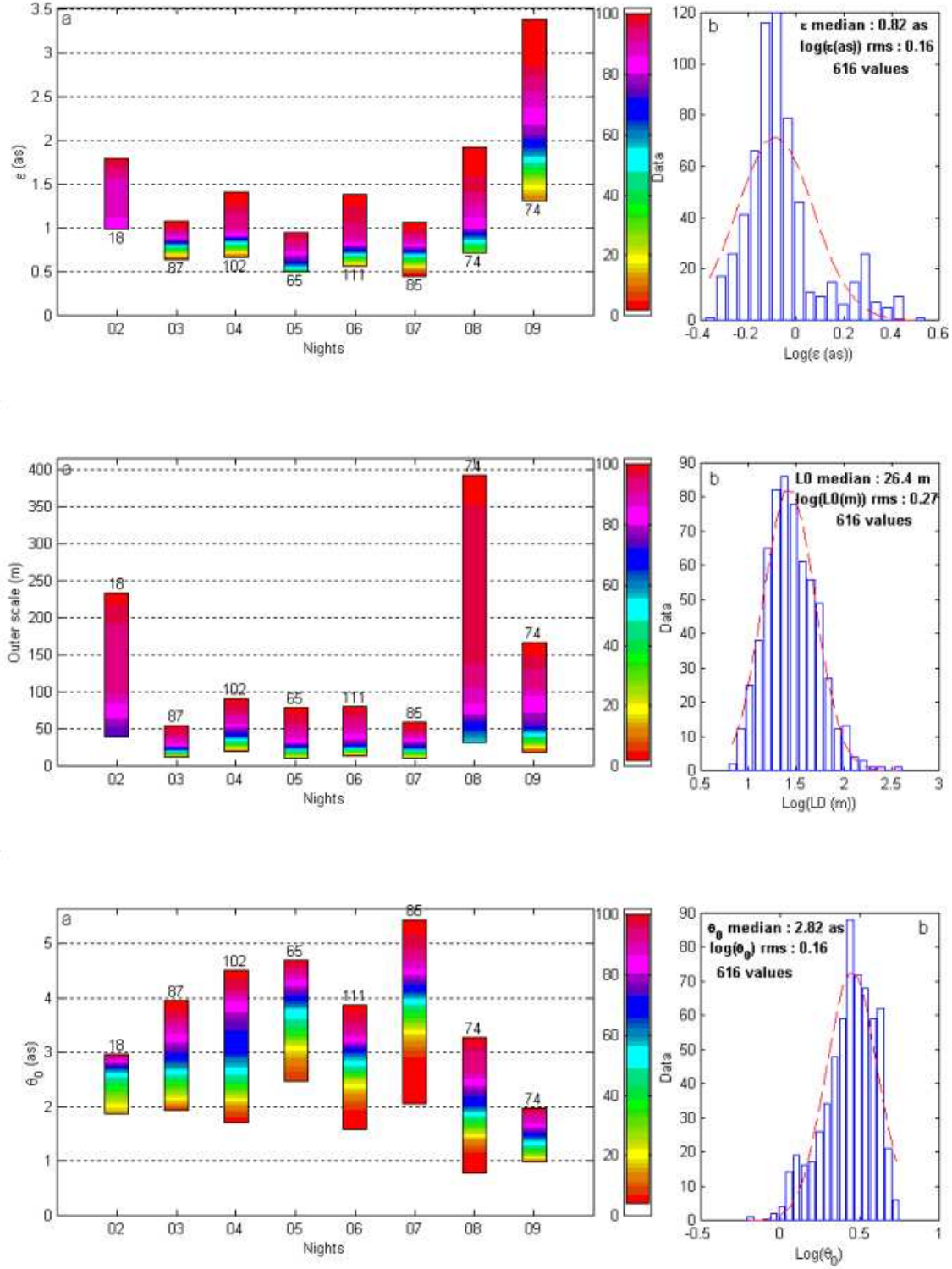


FIGURE 3.34: The GSM results obtained during Cerro Pachón mission from 2 to 10 October 1998: evolution of outer scale L_0 , seeing ε_0 and isoplanatic angle θ_0 . Histograms of those parameters are also presented.

3.3 Balloon

In Tab. 3.6 and 3.7, all the results deduced from balloon flights are summarized. All the variables have been integrated from 20m, which is approximately the altitude of the mirror of Gemini telescope. Column *WV* refers to the water vapor content, deduced from the relative humidity profile.

Then in Tables 3.8 and 3.9, are summarized the same variables, but with the integration beginning at 5m above ground level. This new set of data are presented here to be later compared with G-Scidar.

Detailed profiles of each flight is given in chapter 7.

TABLE 3.6: Résumé of all balloon results. The integrated parameters have been computed from about 20m above ground level, which is approximately the height of Gemini mirror.

Fl.	Date	U.T	Mod	Up km	ϵ as	r_o cm	Scint %	θ_{AO} as	τ_{AO} ms	θ_{SI} as	τ_{SI} ms	WV mm
116	13/01	02:33	GPS	22	.38	27	8	2.1	5.8	3.2	8.1	3.1
117	13/01	05:14	GPS	22	.32	32	3	4.0	8.6	4.7	10.3	3.3
118	14/01	03:08	GPS	25	.53	19	20	1.1	3.7	2.0	6.1	3.2
119	15/01	02:40	GPS	16	.41	25	7	2.5	5.3	3.8	9.2	3.0
120	16/01	04:09	GPS	22	.89	11	9	2.6	6.1	2.7	6.6	2.0
121	17/01	03:44	GPS	27	.60	17	9	2.0	7.5	2.3	8.1	.8
122	17/01	21:12	GPS	19	2.10	5	61	.65	2.0	.8	2.4	3.3
123	18/01	02:46	GPS	25	.37	28	4	2.9	10.6	3.4	13.7	2.3
124	19/01	02:16	GPS	31	.75	14	19	1.4	3.1	2.0	5.3	9.3
125	31/01	03:00	STA	26	.64	16	17	1.5		2.4		4.6
126	15/02	02:07	STA	28	.47	22	7	2.5		3.2		2.5
127	29/02	01:51	STA	24	.39	26	6	2.6		3.3		2.8
128	17/03	03:24	STA	12	.69	15	6	4.5		5.1		8.0
129	29/03	03:00	STA	25	.54	19	29	.87		3.9		1.3
130	14/04	03:40	STA	26	.61	17	8	2.7		3.1		4.0
131	14/04	06:50	STA	23	1.18	9	33	.89		1.1		1.7
132	15/04	02:15	STA	25	.72	14	13	1.6		1.9		2.0
133	15/04	04:50	STA	26	1.82	6	25	1.1		1.1		2.4
134	16/04	02:05	STA	25	.77	13	9	1.8		2.2		3.2
135	16/04	04:30	STA	25	.52	20	7	2.6		3.0		3.7
136	18/05	02:30	STA	25	.25	40	3	3.7		5.5		1.7
137	31/05	00:44	STA	23	.67	15	22	1.0		1.6		.9
138	21/06	01:50	STA	21	.59	17	7	2.8		3.2		3.2

TABLE 3.7: Résumé of all balloon results (next). The integrated parameters have been computed from about 20m above ground level, which is approximately the height of Gemini mirror.

Fl.	Date	U.T	Mod	Up km	ϵ as	r_o cm	Scint %	θ_{AO} as	τ_{AO} ms	θ_{SI} as	τ_{SI} ms	WV mm
139	05/07	01:30	STA	23	1.27	8	50	.63		.8		2.1
140	15/07	05:35										
141	16/07	03:46	GPS	25	1.02	10	30	.98	1.1	1.3	1.9	3.4
142	17/07	02:05	GPS	10	.68	15	10	3.4	1.5	6.1	3.0	4.1
143	17/07	04:20	GPS	25	1.06	10	30	1.2	1.0	1.7	2.1	4.2
144	18/07	06:20	GPS	25	.71	15	20	1.4	2.3	2.4	2.8	1.3
145	19/07	03:20	GPS	25	.88	12	21	1.5	1.7	2.2	2.6	2.8
146	20/07	06:00										
147	2/08	01:20	GPS	22	.72	14	33	.86	1.8	1.7	3.6	2.9
148	16/08	01:30										
149	16/08	04:56	GPS	20	.55	19	9	2.3	3.8	2.9	5.3	2.5
151	30/08	01:37										
152	13/09	01:53	GPS	23	.91	11	45	.7	1.6	1.3	2.5	4.3
153	13/09	6:37	GPS	14	.71	14	7	2.7	2.2	3.0	3.0	2.6
154	02/10	03:18	GPS	23	.72	14	10	1.8	3.5	2.0	9.3	1.3
155	04/10	04:05	GPS	23	.49	21	13	1.5	4.5	2.3	6.0	2.4
156	05/10	04:26	GPS	24	.50	20	11	1.7	5.0	2.5	7.8	3.3
157	06/10	03:07										
158	06/10	04:52	GPS	24	.27	38	4	3.4	11.8	4.9	15.8	2.5
159	07/10	04:18	GPS	23	.32	32	5	3.0	7.1	4.6	10.0	1.3
160	08/10	04:10	GPS	23	.39	26	5	2.5	6.5	3.2	7.6	1.6
161	09/10	04:57	GPS	24	.55	19	6	2.4	3.5	2.7	5.6	1.8
162	10/10	03:01	GPS	23	1.26	8	28	1.3	1.6	1.5	2.6	.3
163	02/11	01:00	STA	28	.28	36	5	2.9		5.2		1.6
164	21/11	03:25	STA	24	.31	33	7	2.4		4.1		.7
165	11/12	02:00	STA	23	.47	22	9	2.2		3.1		7.5

TABLE 3.8: Résumé of all balloon results. The integrated parameters have been computed from about 5m above ground level, which is approximately the height of the 1.5m telescope at Tololo.

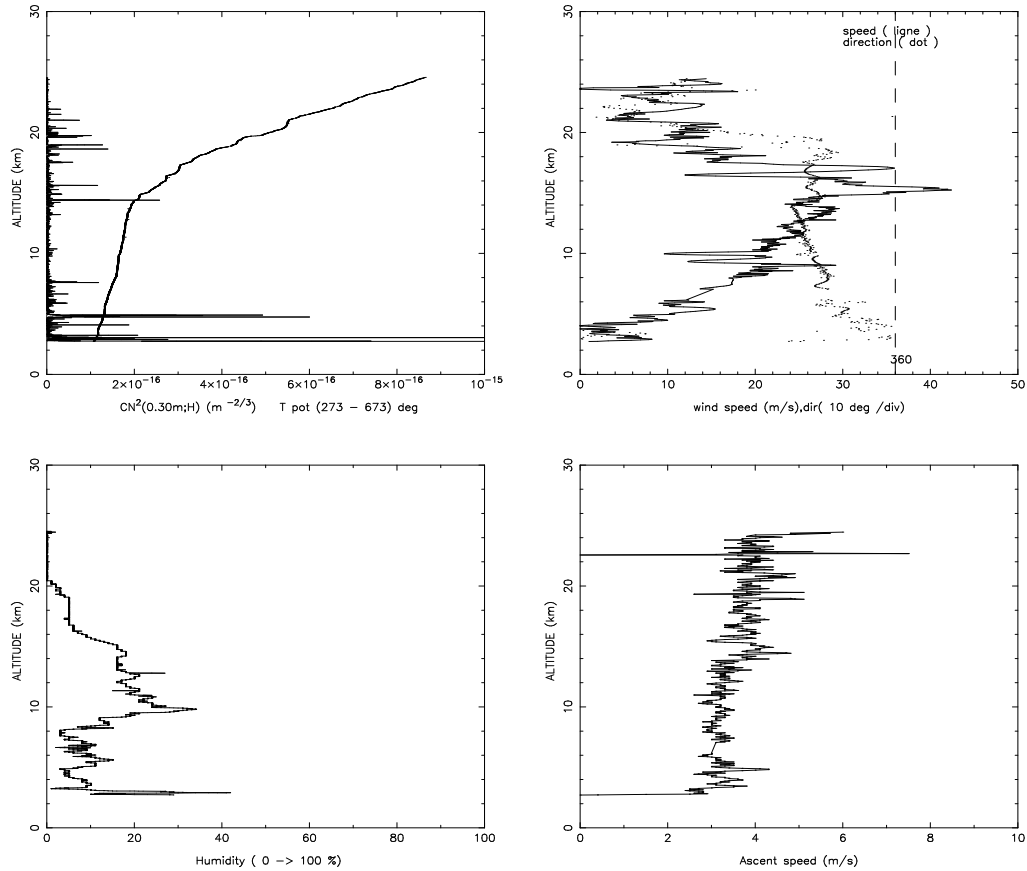
Fl.	Date	U.T	Mod	Up km	ϵ as	r_o cm	Scint %	θ_{AO} as	τ_{AO} ms	θ_{SI} as	τ_{SI} ms	WV mm
116	13/01	02:33	GPS	22	.40	26	7	2.1	5.8	3.1	7.9	3.2
117	13/01	05:14	GPS	22	.38	27	3	4.0	8.5	4.3	9.8	3.3
118	14/01	03:08	GPS	25	.54	19	20	1.1	3.7	1.9	6.0	3.2
119	15/01	02:40	GPS	16	.43	24	7	2.5	5.3	3.6	8.6	3.0
120	16/01	04:09	GPS	22	.89	11	9	2.6	6.1	2.7	6.6	2.0
121	17/01	03:44	GPS	27	.60	17	9	2.0	7.5	2.3	8.1	.8
122	17/01	21:12	GPS	19	2.53	4	61	.65	2.0	.7	2.3	3.4
123	18/01	02:46	GPS	25	.44	23	4	2.9	10.0	3.2	13.1	2.4
124	19/01	02:16	GPS	31	.77	13	18	1.4	3.1	1.9	5.1	9.3
125	31/01	03:00	STA	26	.66	15	17	1.5		2.3		4.7
126	15/02	02:07	STA	28	.51	20	7	2.5		3.1		2.5
127	29/02	01:51	STA	24	.51	20	6	2.6		2.9		2.8
128	17/03	03:24	STA	12	.70	15	6	4.5		5.1		8.2
129	29/03	03:00	STA	25	.54	19	29	.87		3.9		1.3
130	14/04	03:40	STA	26	.67	15	8	2.7		2.9		4.1
131	14/04	06:50	STA	23	1.19	9	33	.89		1.1		1.7
132	15/04	02:15	STA	25	.75	14	13	1.6		1.8		2.1
133	15/04	04:50	STA	26	1.84	6	25	1.1		1.1		2.4
134	16/04	02:05	STA	25	.80	13	9	1.8		2.2		3.2
135	16/04	04:30	STA	25	.55	19	7	2.6		3.0		3.8
136	18/05	02:30	STA	25	.85	12	4	3.7		3.3		1.7
137	31/05	00:44	STA	23	1.31	8	23	1.0		1.1		.9
138	21/06	01:50	STA	21	.65	16	7	2.8		3.1		3.2

TABLE 3.9: Résumé of all balloon results (next). The integrated parameters have been computed from about 5m above ground level, which is approximately the height of the 1.5m telescope at Tololo.

Fl.	Date	U.T	Mod	Up km	ϵ as	r_o cm	Scint %	θ_{AO} as	τ_{AO} ms	θ_{SI} as	τ_{SI} ms	WV mm
139	05/07	01:30	STA	23	1.31	8	50	.6		.8		2.1
140	15/07	05:35										
141	16/07	03:46	GPS	25	1.02	10	30	.98	1.1	1.3	1.9	3.4
142	17/07	02:05	GPS	10	.68	15	10	3.4	1.5	6.1	3.0	4.1
143	17/07	04:20	GPS	25	1.07	10	30	1.2	1.0	1.6	2.0	4.3
144	18/07	06:20	GPS	25	.76	14	20	1.4	2.3	2.2	2.7	1.3
145	19/07	03:20	GPS	25	.88	12	21	1.5	1.7	2.2	2.5	2.8
146	20/07	06:00										
147	2/08	01:20	GPS	22	.77	13	33	.86	1.8	1.6	3.2	2.9
148	16/08	01:30										
149	16/08	04:56	GPS	20	.58	18	8	2.3	3.8	2.8	5.1	2.5
151	30/08	01:37										
152	13/09	01:53	GPS	23	.91	11	45	.7	1.6	1.3	2.5	4.4
153	13/09	6:37	GPS	14	.73	14	7	2.7	2.2	3.0	3.0	2.7
154	02/10	03:18	GPS	23	.84	12	10	1.8	4.6	1.9	6.3	1.3
155	04/10	04:05	GPS	23	.55	19	13	1.5	4.0	2.1	5.8	2.4
156	05/10	04:26	GPS	24	.59	17	11	1.7	4.8	2.2	7.4	3.3
157	06/10	03:07										
158	06/10	04:52	GPS	24	.30	34	4	3.4	11.8	4.6	15.0	2.5
159	07/10	04:18	GPS	23	.35	29	5	3.0	6.9	4.2	8.8	1.3
160	08/10	04:10	GPS	23	.47	22	5	2.5	6.4	2.9	7.1	1.6
161	09/10	04:57	GPS	24	.60	17	6	2.4	3.4	2.6	4.7	1.9
162	10/10	03:01	GPS	23	1.26	8	28	1.3	1.6	1.5	2.6	.3
163	02/11	01:00	STA	28	.32	31	5	2.9		4.4		1.6
164	21/11	03:25	STA	24	.49	21	7	2.4		2.8		.7
165	11/12	02:00	STA	23	.76	13	9	2.2		2.4		7.6

3.3.1 Nightly observation

As said before, balloons give, once a night, high resolution vertical profiles of C_n^2 , temperature, humidity and wind. Knowing the time at which the balloon is at a given altitude, one is able to compute the ascent speed. In Fig. 3.35 one can see four plots and a résumé of the integrated parameters. On the first plot is shown both the $C_n^2(h)$ profile between 0. and $10^{-15} \text{m}^{-2/3}$ and the potential temperature $\theta(h)$ between 273 and 673 °K. When looking carefully at these curves, one will notice that, on many occasions, a pair of turbulent layers appears with coincidence with a “stair-like” trend of the potential temperature (Coulman et al., 1995).



```

VOL N   116 PACHON   13/01/98   2:33.TU
FWHM :  .41 (arcsec)  R0 : 24.59 (cm)  Hum : 3.0 mm
Adaptive Optics      : Time(ms): 4.69   Isop. angle (arcsec) :1.86
Speckle Interferometry : Time(ms): 7.00   Isop. angle (arcsec) :3.00
Sum from    36   to 21845 m. agl. -- lost interval:    0 m.

```

FIGURE 3.35: Résumé of flight 116, on 13 Jan 1998.

Next plot (top-right of Fig. 3.35) gives a vertical profile of the wind, the direction being comprized between 0 and 360°, direction=0 means wind coming from North,

90 coming from East.

Next plot (bottom-left of Fig. 3.35) gives the humidity profile in percent unit. for each night Finally (bottom-right of Fig. 3.35) the ascent speed is plotted.

On the bottom of each figure is a résumé of the integrated parameters: the seeing, r_o , water vapor content (Hum) expressed in mm, the speckle boiling time and isoplanatic angle for both adaptive optics and speckle interferometry.

The most obvious remark is that optical turbulence is concentrated in very thin turbulent layers a few meters thick, except at ground level, where more turbulence is noticed.

On many wind profiles, “weavy-like” patterns are visible, presumably triggered by atmospheric gravity waves. In these areas, one can assume that $\frac{dU}{dz}$ is very large, overcoming the static stability, and gives rise to turbulence. If it coincides with a region in which the vertical gradient of potential temperature is high, one can expect a large C_N^2 value.

At the bottom of each figure is given the boundaries of the integrals, which means the contributing part of the atmosphere, here, for exemple, from 36m to 21 845m, above ground level. “Lost interval” means the total of the slabs where no measurement were sent to the ground receiver.

3.3.2 Statistics over each one-week run

In Fig. 3.36 is shown the mean vertical profile averaged over flights 116 to 124, corresponding to first run, with a vertical convolution over 800m. In Fig. 3.37 is shown the mean vertical profile averaged over flights 130 to 136, corresponding to second run, with a vertical convolution over 800m. In Fig. 3.38 is shown the mean vertical profile averaged over flights 141 to 145, corresponding to third run, with a vertical convolution over 800m. In Fig. 3.39 is shown the mean vertical profile averaged over flights 154 to 162, corresponding to fourth run, with a vertical convolution over 800m.

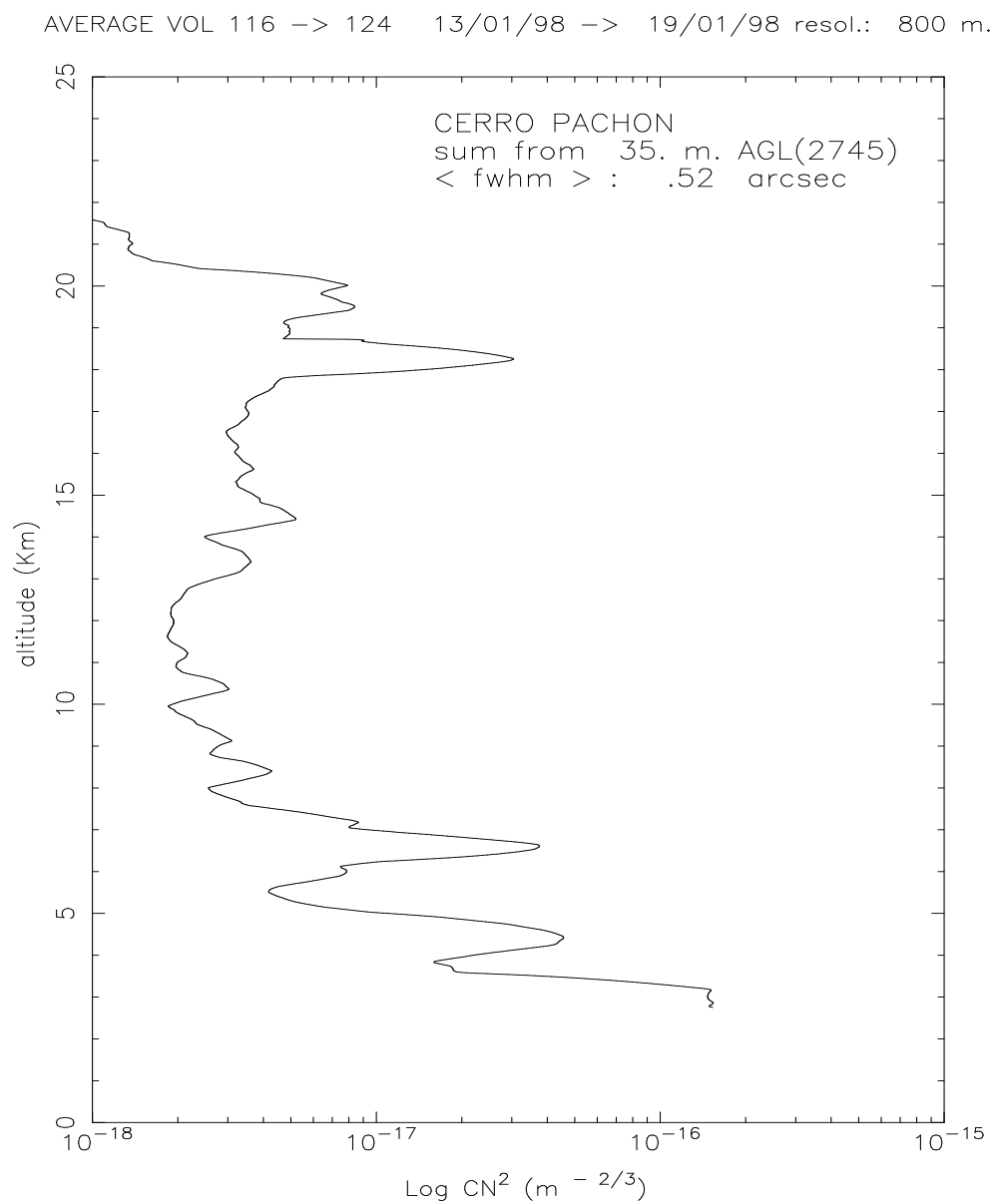


FIGURE 3.36: Average C_N^2 profile, from flight 116 to 124, first run

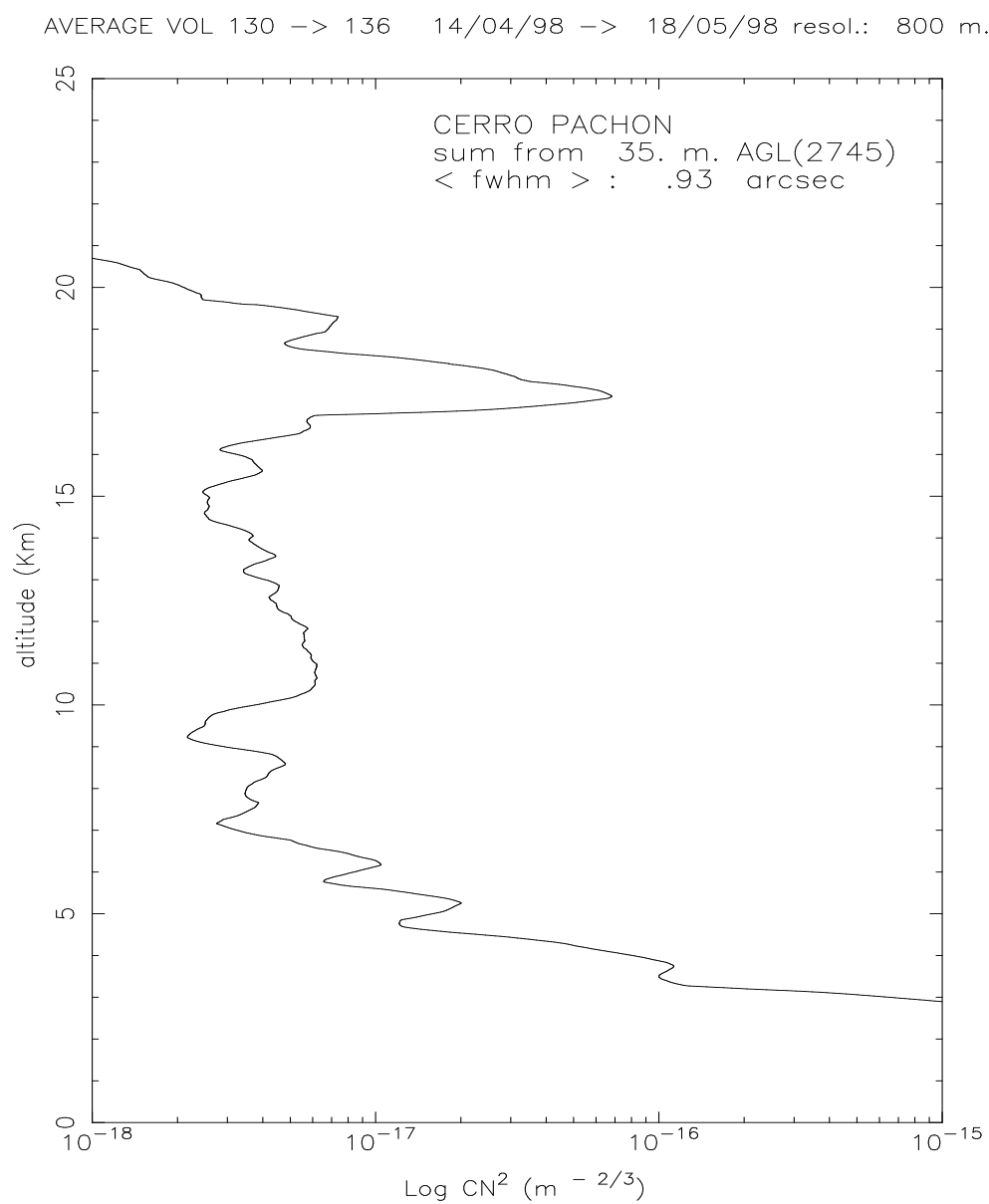


FIGURE 3.37: Average C_N^2 profile, from flight 130 to 136, second run

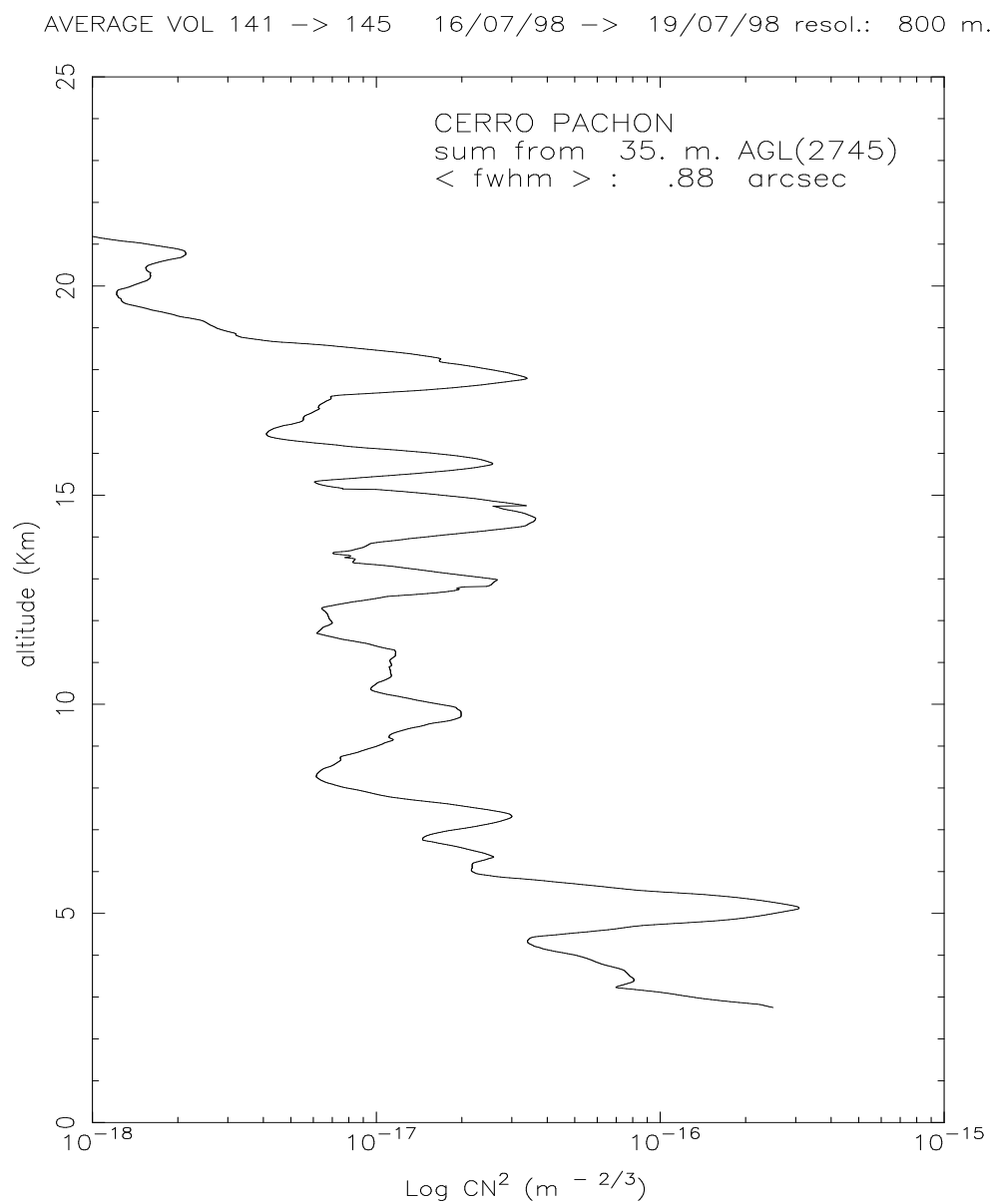


FIGURE 3.38: Average C_N^2 profile, from flight 141 to 145, third run

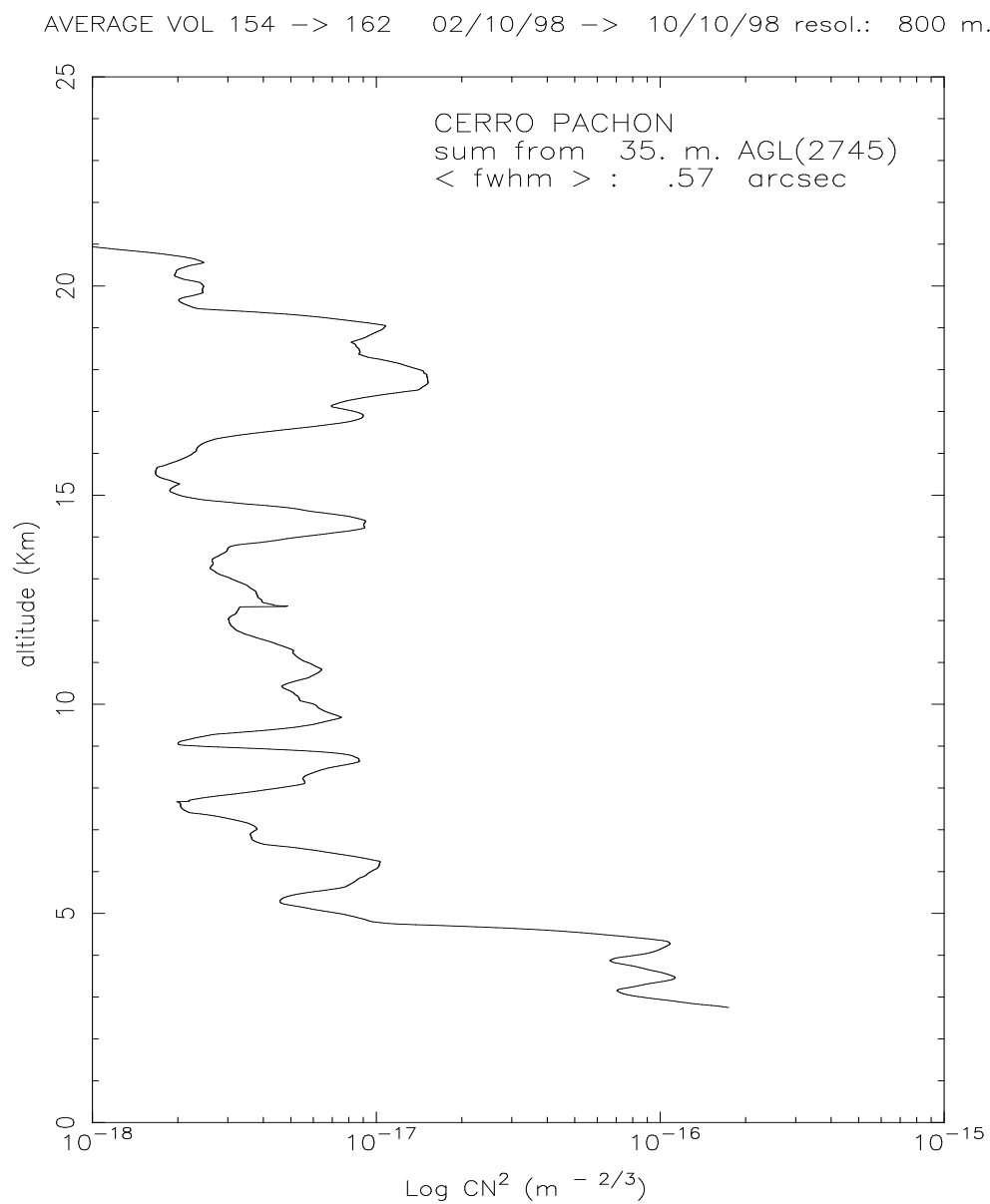


FIGURE 3.39: Average C_N^2 profile, from flight 154 to 162, fourth run

3.3.3 All year statistics

In Fig. 3.40 is plotted the mean vertical profile averaged over flights 116 to 165, with a vertical convolution over 800m. More and more vertical structure disappeared, as expected.

One notes a steep decrease close to the ground, a thin bump at 5km, then a larger layer at 17.5–19km, and finally quite no turbulence above 20km.

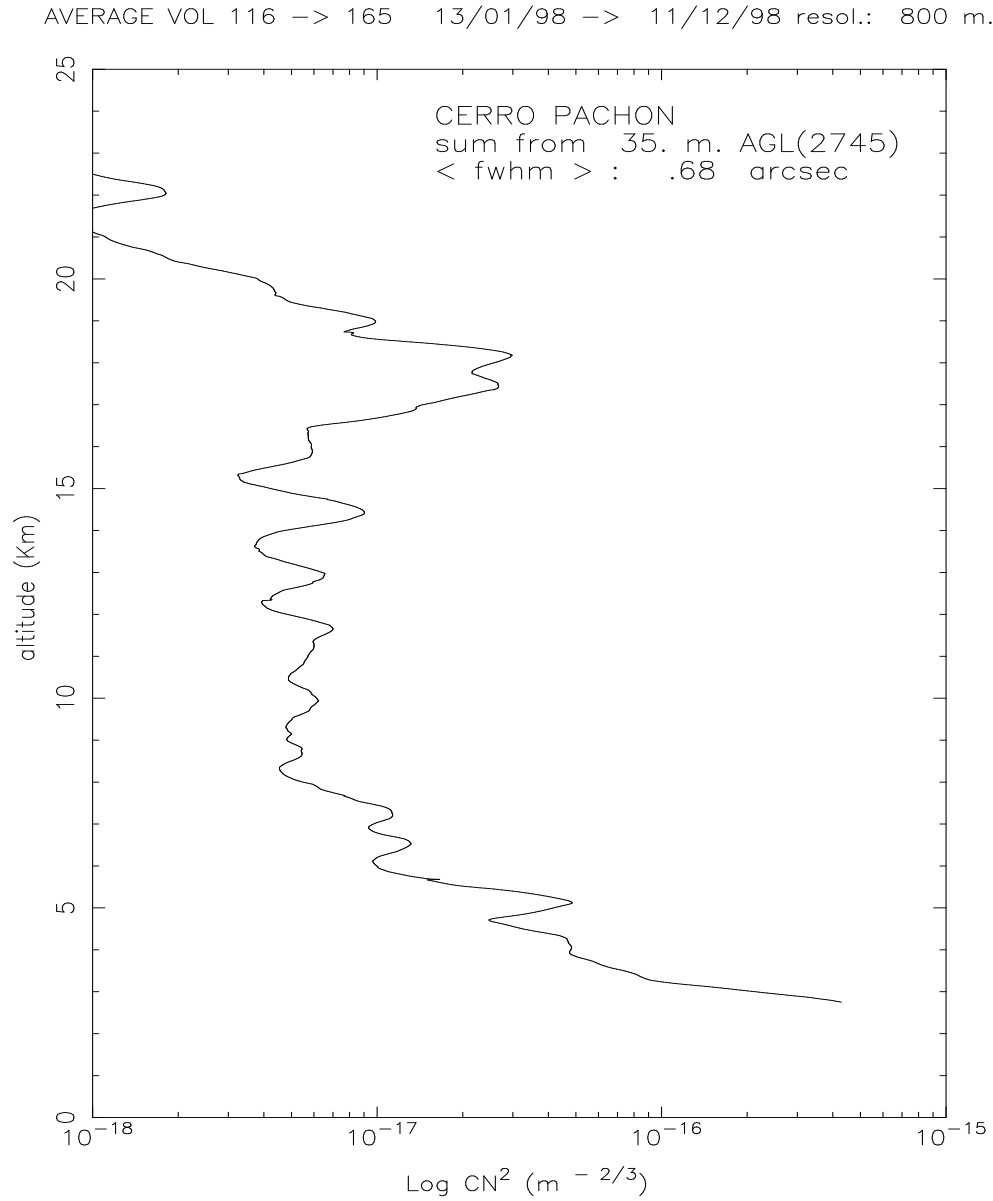


FIGURE 3.40: Average C_N^2 profile, from flight 116 to 165, whole year

Set	Date -Time	Equivalent seeing between 4 and 27 m	
		Min – Max (arcsec)	$< median > / mean$ (arcsec)
1	10.03.98 : 22:27→02:58 UT	0.02 – 0.27	0.08/0.12
2	10.04.98 : 22:25→05:16 UT	0.02 – 0.44	0.08/0.12
3	10.05.98 : 22:15→03:28 UT	0.01 – 0.24	0.06/0.08
4(*)	10.06.98 : 23:49→10:49 UT	0.01 – 0.15	0.05/0.08
5	10.07.98 : 17:19→21:19 UT		
	10.07.98 : 21:19→06:47 UT	0.004 – 0.35	0.08/0.11
	10.08.98 : 06:47→21:07 UT		
	10.08.98 : 21:07→10:07 UT	0.01 – 0.45	0.09/0.13

TABLE 3.10: Surface layer contribution as measured with the instrumented mast. (*) minimum, maximum and mean values are computed between 23:49 and 06:49 UT, for this night, to avoid the bias due to the increase of C_n^2 after the sunrise

3.4 Mast

From 3 to 8 of December 1998, 5 sets of continuous mast measurements are taken. The fourth one are nightly measurements and the fifth run over two days (columns one and two of the Table 3.10, the fifth set of data is split into its daily and nightly parts). The time resolution of the microthermal sensors is around 5ms. An integrated value of the structure constant C_T^2 is transmitted to the ground each 1.5s. The C_n^2 is calculated from the C_T^2 using the appropriate values of mean temperature and pressure.

3.4.1 Nightly observations

Smoothed temporal profiles of the C_n^2 are obtained in computing the temporal average of the data over 1mn every minute. Each minute, both median and mean values are calculated. For the fifth set, the mean and median temporal profiles at the 4 altitudes are plotted on Fig. 3.41 for the whole set and on Fig. 3.42 from 21:07 to 06:47 local time (LT). In Fig. 3.41, the different phenomena producing the turbulence the day and the night explain the increase of turbulence during the day which causes a saturation of the microthermal sensors at 4 and 8m. The typical decrease of the C_n^2 with the altitude appears on the nightly graph (Fig. 3.42).

The weight of the turbulence in the surface layer is estimated in integrating the C_n^2 between 4 and 27m and converting the result in its equivalent seeing. The first step is to log-fit the C_n^2 versus the altitude at each time which gives the constants K and α of the relation $C_n^2(h) = Kh^\alpha$. And finally, the last relationship is integrated between 4 and 27m and converted into seeing. The median and mean temporal profiles of the seeing corresponding to the C_n^2 profiles of the Fig.3.42 are plotted on the Fig. 3.43.

The Table 3.10 summarizes the fluctuations of the seeing for each nightly set of data. The minimum and the maximum of the seeing temporal profiles and the mean of the median and the mean profiles, respectively, are given.

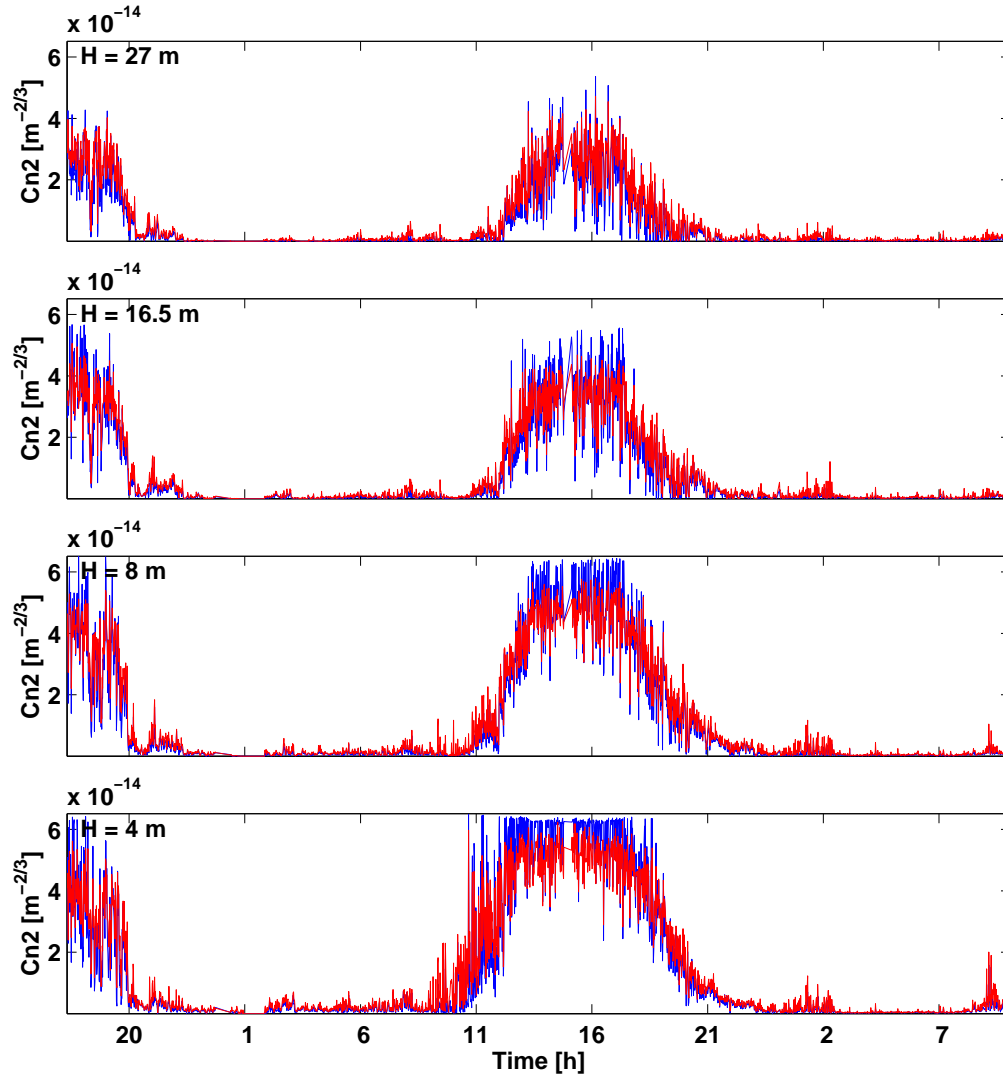


FIGURE 3.41: 1mn sampled temporal profiles of the C_n^2 for the fifth set. The blue lines are the median profiles and the red ones are the mean profiles

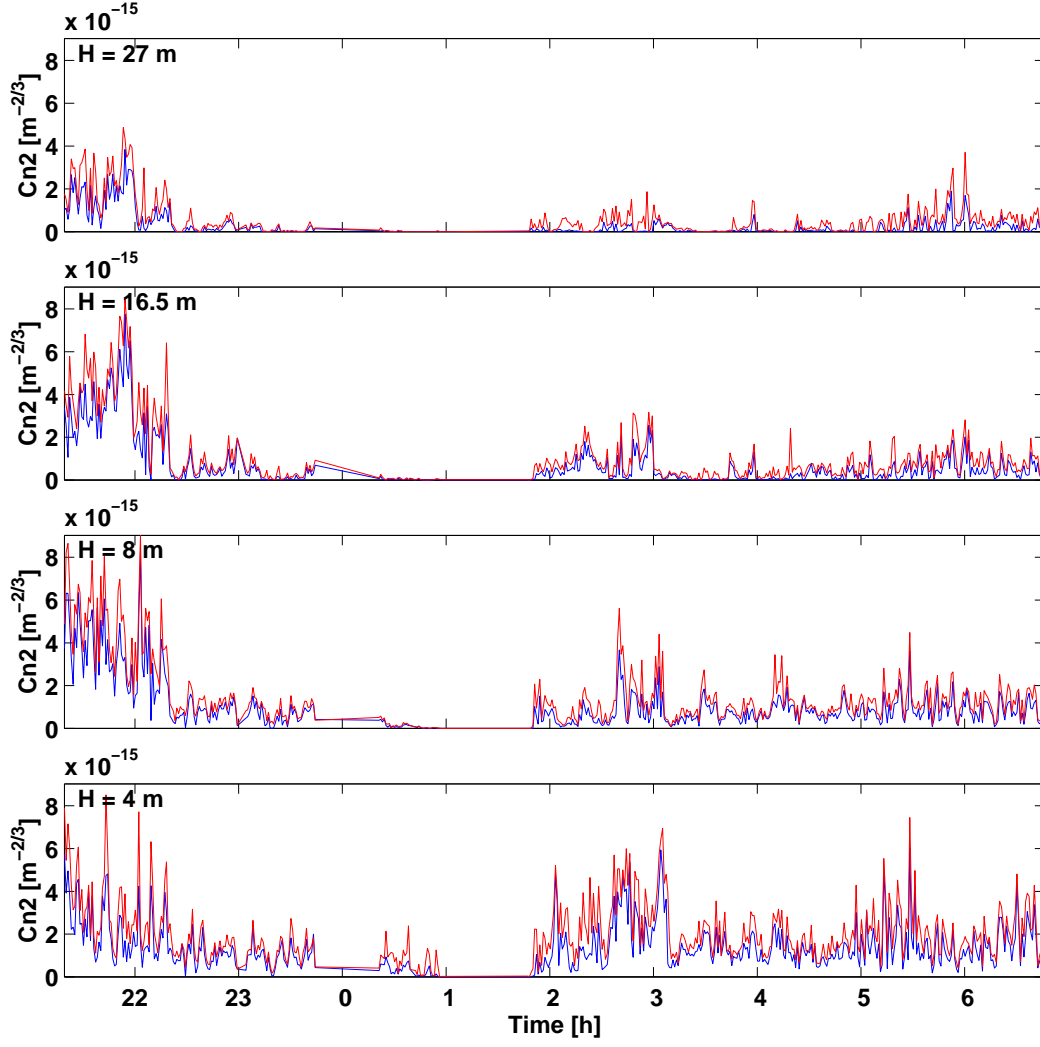


FIGURE 3.42: 1mn sampled temporal profiles of the C_n^2 for the fifth set between 21:07 and 06:47 LT. The blue lines are the median profiles and the red ones are the mean profiles

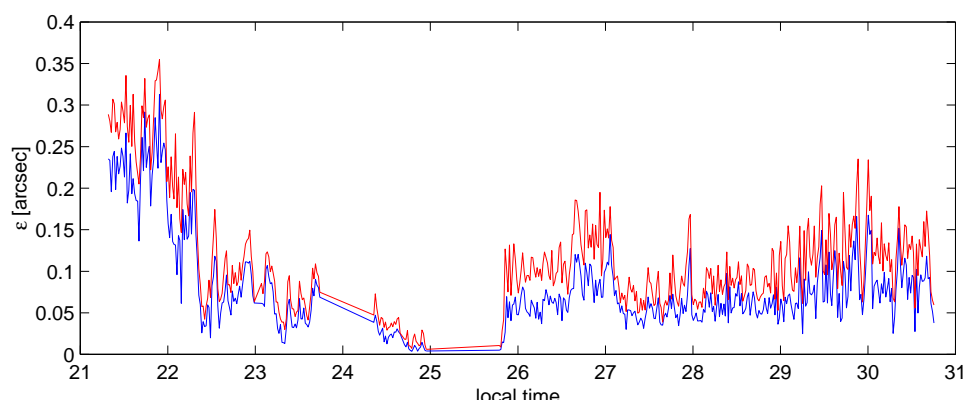


FIGURE 3.43: Seeing of the surface layer between 4 and 27m for the fifth set of data between 21:19 and 06:47 LT (Median: Blue, Mean: Red).

Chapter 4

DISCUSSION

4.1 G–Scidar results

From what has been shown in chapter 3, the G–Scidar alone is able to monitor with great details the behaviour of optical turbulence inside the dome, the boundary layer and each layer propagating in the free atmosphere. For each of these layers, it is possible to monitor, with time and from ground level up to 20–30km, not only its absolute contribution to seeing degradation but also its horizontal velocity. We will show later that the profiles, and the inferred integrated variables, given by the G–Scidar technique will be cross compared successfully with both GSM and balloon instruments.

It is tempting to bring some conclusions of this campaign from the analysis of G–Scidar alone. We reproduce here three main results in Table 4.1, 4.2 and Table 4.3, already shown in last chapter 3.

- **Seeing seasonal effect.** From Table 4.2, one can note that the worst seeing is encountered during winter (July), in the boundary layer as well as in the free atmosphere. The rest of the year (January, April and October), no seasonal effect appears.
- **BL/FA relative contribution.** The threshold arbitrary set at 1km above ground level seems to share the atmosphere in two slabs of almost the same amount of optical turbulence.
- **Dome seasonal trend.** Dome seeing seems to be worst during summer (January), and gives the lowest contribution in July and October.
- **$\theta, v, \tau, d_0, h_{opt}$ and θ_{opt}/θ seasonal effect.** As for the seeing, the worst observing conditions for what concern the isoplanatic angle, the equivalent velocity, the coherence time and the “cone effect” are found in winter, as it appears in Table 4.3.
- **Dynamical range of variation.** From the analysis of the maximum and minimum values of integrated variables, it is possible to assess its dynamical range of variation, on a night by night basis. The result is summarized in Table 4.4.

TABLE 4.1: Résumé of each G-Scidar run; Normal processing (N).

Run	Month	BL+Dome seeing	FA seeing	Total	θ_{OA}
01	January	0.84	0.49	1.04	2.20
02	April	0.77	0.52	0.99	1.87
03	July	0.87	0.85	1.34	1.43
04	October	0.74	0.47	0.94	2.50
All	run	0.80	0.56	1.06	2.14

TABLE 4.2: Résumé of G-Scidar seeing measurements for each run and for the whole campaign. Normal Dome seeing processing (D).

Run	BL+D	BL inf.	BL sup.	FA	Atmos. inf.	Atmos. sup.	Dome sup.	Dome inf.
Case unit	N arcsec	D arcsec	A arcsec	N arcsec	D arcsec	A arcsec	D arcsec	A arcsec
01 Jan	0.84	0.49	0.53	0.49	0.80	0.83	0.63	0.57
02 Apr	0.77	0.47	0.49	0.52	0.76	0.78	0.46	0.44
03 Jul	0.87	0.68	0.68	0.85	1.22	1.23	0.37	0.36
04 Oct	0.74	0.46	0.57	0.47	0.72	0.80	0.45	0.28
All	0.80	0.52	0.58	0.56	0.85	0.89	0.48	0.38

1. The seeing expressed in arcsec varies within a ratio of 3.2. But, when expressed in $C_N^2 dh$ unit the ratio becomes $3.2^{5/3} = 7$.
2. The isoplanatic angle does not vary very much.
3. The equivalent velocity varies more than the isoplanatic angle
4. The coherence time is the most variable integrated parameter, especially τ_{AO} .

TABLE 4.3: Résumé of each G-Scidar integrated variables, for each run and for the whole campaign. Dome seeing processing (case D).

Run	θ_{AO}	θ_{SI}	v_{AO}	v_{SI}	τ_{AO}	τ_{SI}	d_0	h_{opt}	θ_{opt}/θ
Case	D	D	D	D	D	D	D	D	D
unit	arcsec	arcsec	m/s	m/s	ms	ms	m	km	n.u
01 Jan	2.1	2.5	5.9	5.6	8.2	9.2	3.73	2.91	1.21
02 Apr	2.0	2.5	7.6	6.4	3.9	5.1	3.49	3.03	1.23
03 Jul	1.4	1.8	12.9	9.1	1.8	2.8	2.41	3.25	1.26
04 Oct	2.5	3.1	6.7	6.2	4.2	5.0	4.37	2.39	1.17
All	2.1	2.6	7.9	6.7	4.6	5.6	3.73	2.73	1.20

TABLE 4.4: Dynamical range of variation of integrated variables. Max and min values have been sorted from a night by night analysis.

Variable	Minimum	Maximum	Range
seeing (")	0.51	1.64	3.2
$\int C_n^2(h)dh(10^{-13}m^{1/3})$	2.25	15.8	7.0
θ_{AO} (")	1.0	3.6	3.6
θ_{SI} (")	1.5	3.9	2.6
τ_{AO} (ms)	1.1	16.1	14.6
τ_{SI} (ms)	2.3	17.4	7.6
v_{AO} (m/s)	2.3	19.5	8.5
v_{SI} (m/s)	2.4	13.0	5.4

4.2 G-Scidar/Balloon for $C_N^2(h)$ profiles

Here we compare vertical profiles of the optical turbulence issued by instrumented balloons and G-Scidar. In order to compare profiles with about the same vertical resolution, the balloon profile is convolved with a sliding triangle the bottom of which is 2km wide. The altitude is given above sea level. That's why balloon profiles begin 500m above the line which represents the Tololo altitude. Balloon profiles begin at the lowest altitude, where the first measurements were available.

If one is to compare the behaviour of the surface layer of both sites, he has to translate the balloon curve 500m lower, to be at the same high above ground level. But, even doing this, one needs to keep in mind that G-Scidar measurements include the Dome and Mirror seeing. In all the following exemples, low altitude optical turbulence deduced from balloons is lower than the one deduced from G-Scidar.

4.2.1 Detailed Run 1. January 98

Here are presented, from Fig. 4.1 to Fig. 4.7 the comparisons during first run. Few remarks:

- Genrally high altitude turbulence is low, few $10^{-18}m^{-2/3}$.
- In Fig. 4.2 and Fig. 4.3 comparison is excellent up to 16km where the balloon records a very strong turbulence, not seen by the Scidar. This case will encoutered in other runs and can be interpreted by the fact that, balloons are drifted towards the Andes by the main rapid stream, where more high altitude turbulence is expected.
- From both experiments, the low atmosphere is stratified: One layer at 5km in Fig. 4.1 and 4.3, two layers in Fig. 4.4. This structure might be generated by the propagation of gravity waves triggered by the local orography.

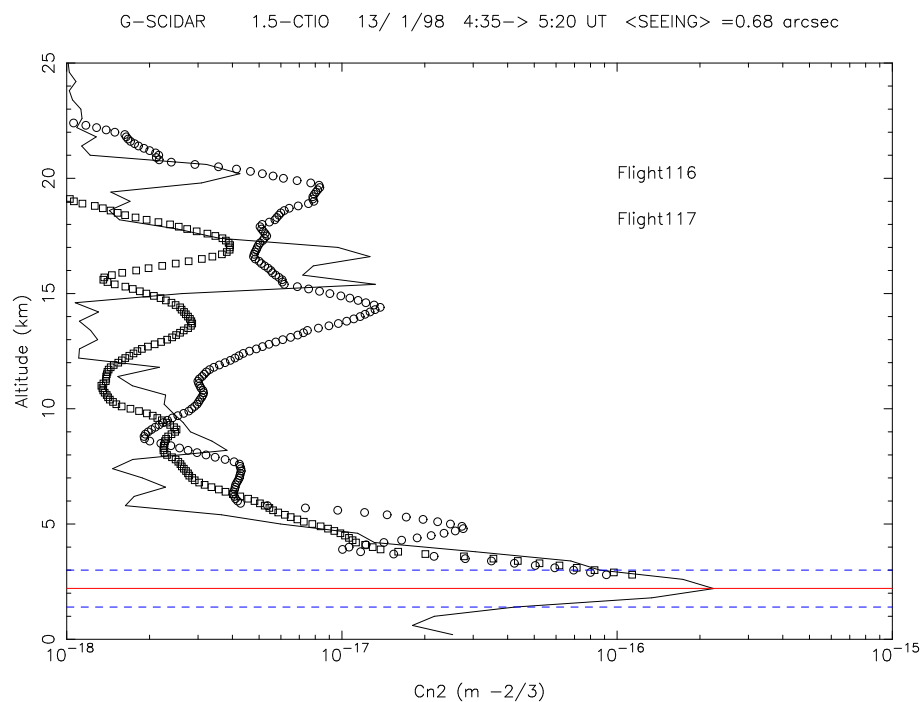


FIGURE 4.1: Comparison G-Scidar/Balloon on 13 Jan 98.

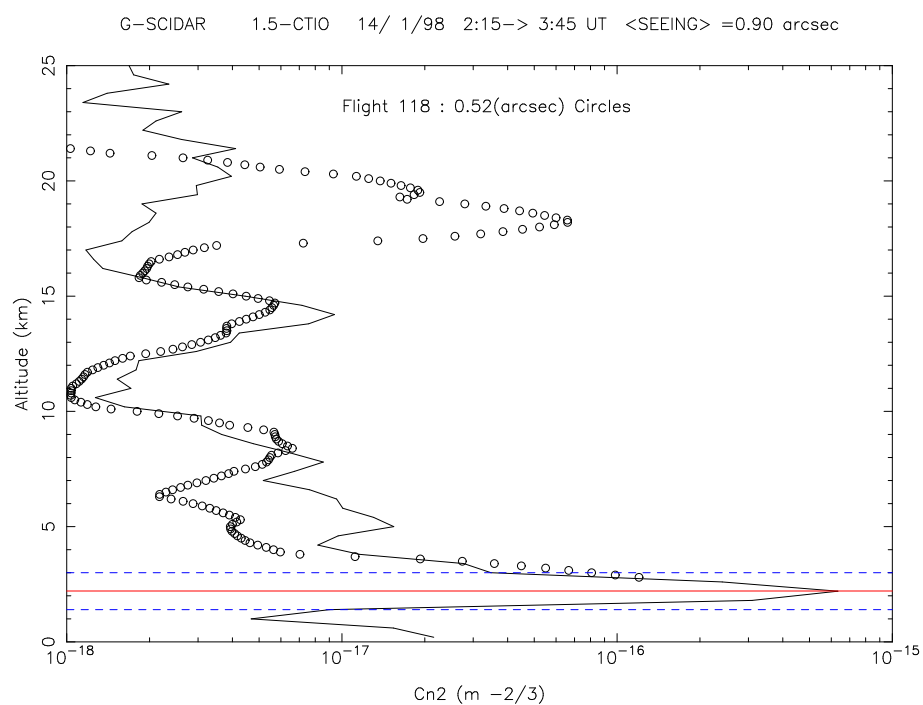


FIGURE 4.2: Comparison G-Scidar/Balloon on 14 Jan 98.

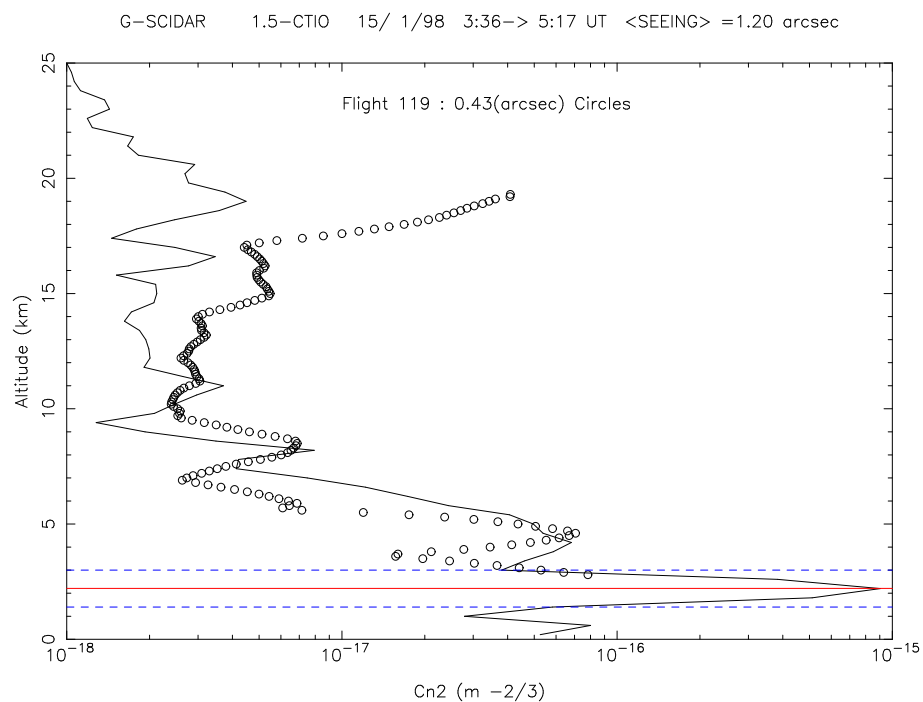


FIGURE 4.3: Comparison G-Scidar/Balloon on 15 Jan 98.

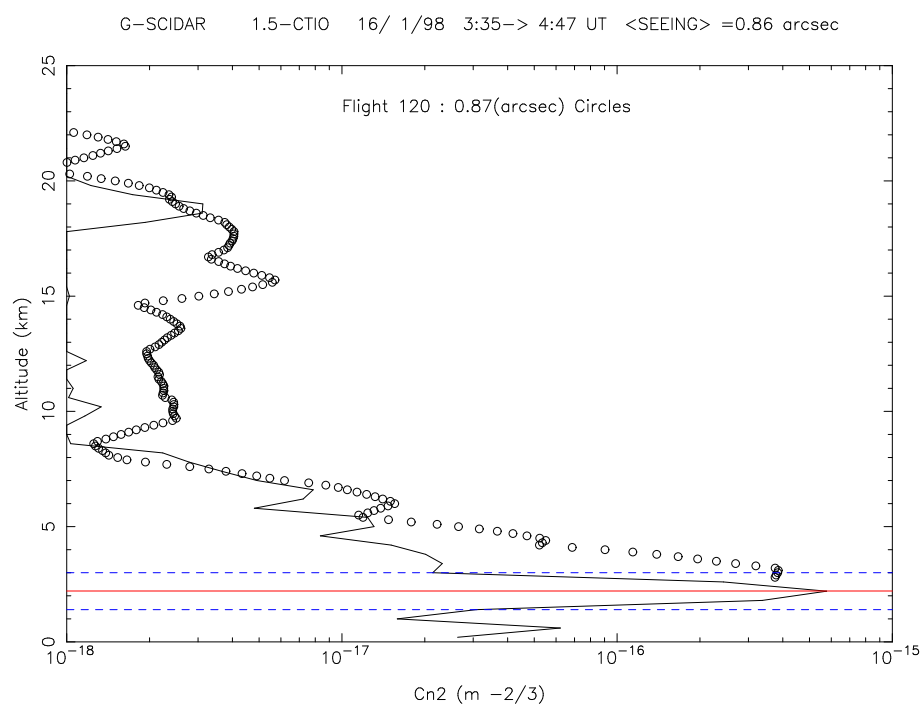


FIGURE 4.4: Comparison G-Scidar/Balloon on 16 Jan 98.

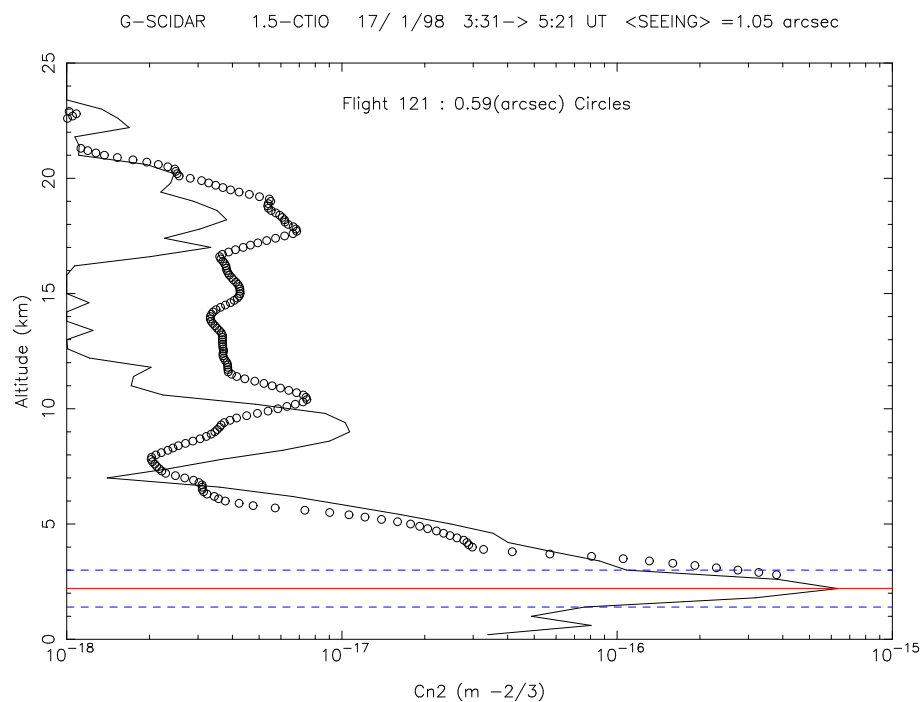


FIGURE 4.5: Comparison G-Scidar/Balloon on 17 Jan 98.

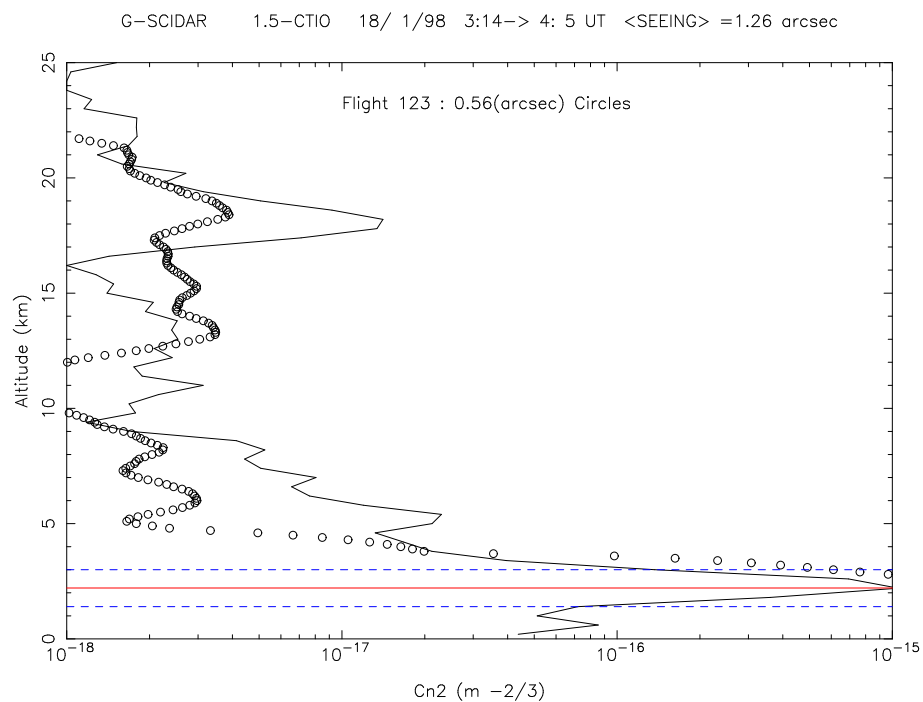


FIGURE 4.6: Comparison G-Scidar/Balloon on 18 Jan 98.

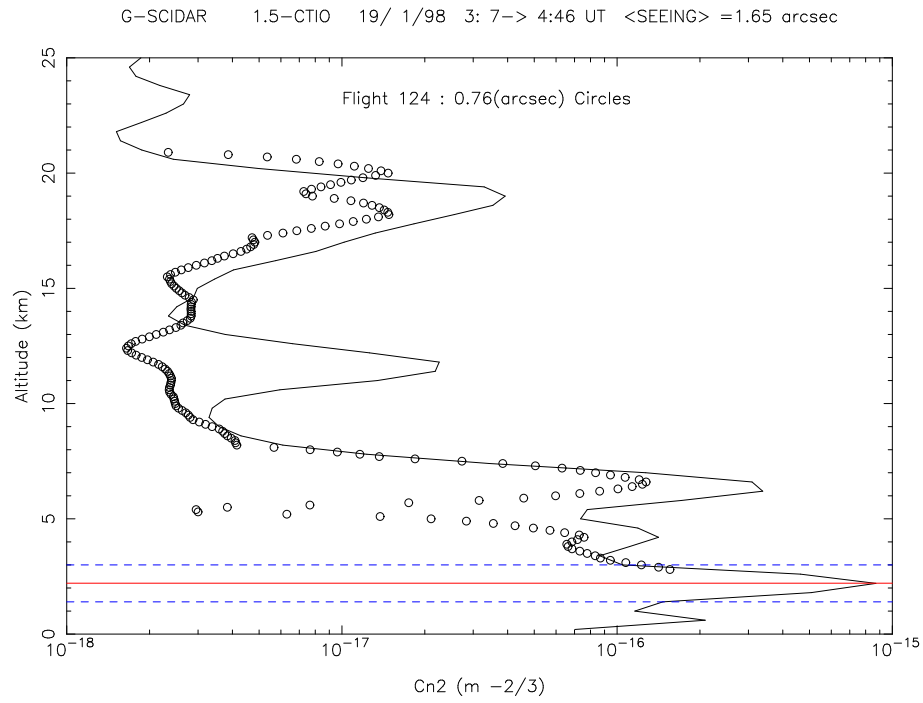


FIGURE 4.7: Comparison G-Scidar/Balloon on 19 Jan 98.

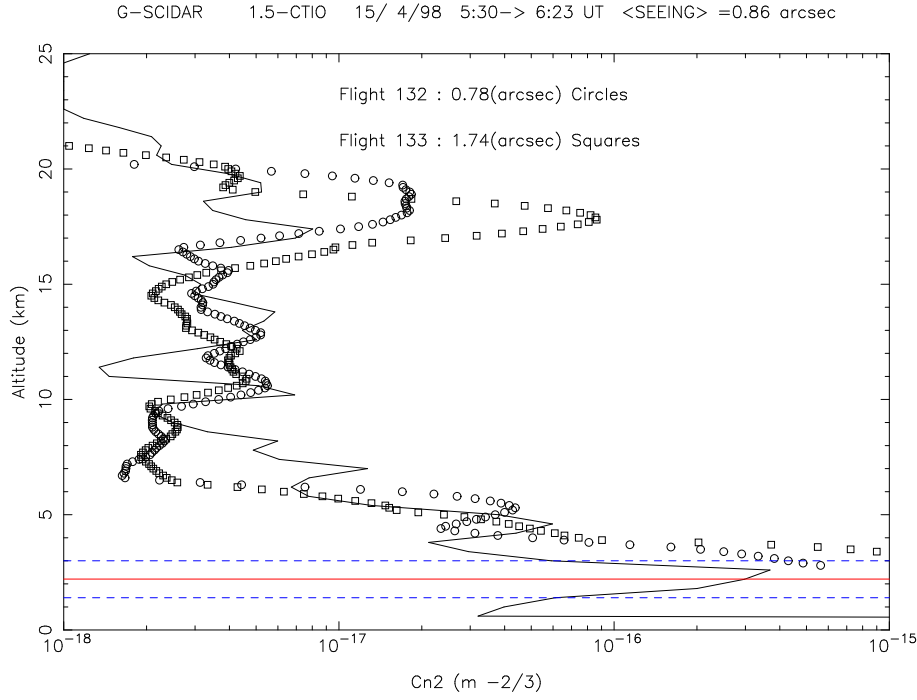


FIGURE 4.8: Comparison G-Scidar/Balloon on 15 Apr 98.

4.2.2 Detailed run 2. April 98

During the second run, where we have few observations due to bad weather, an almost incredible agreement is found between both experiments. During the two nights, two balloons were launched. Few remarks:

- The atmosphere is more structured than during run 1
- Much more turbulence present in the boundary layer at Pachón than at Tololo.
- As in run 1, in Fig 4.8 the 16–17km layer is not detected by the Scidar.

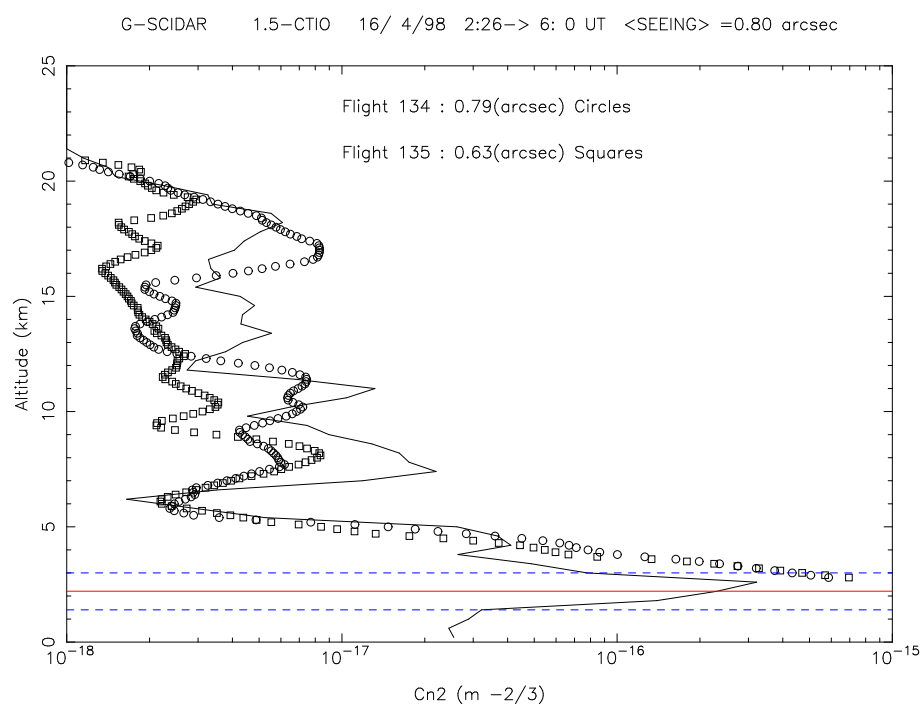


FIGURE 4.9: Comparison G-Scidar/Balloon on 16 Apr 98.

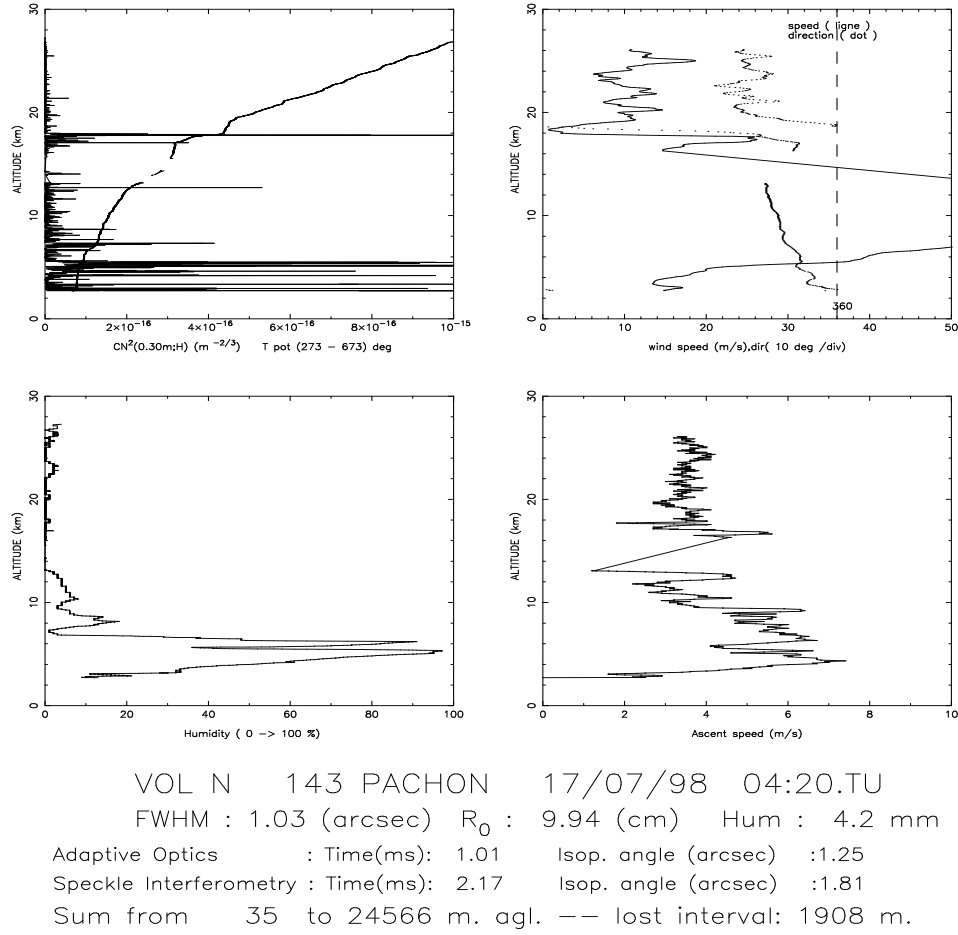


FIGURE 4.10: Résumé of flight 143, on 17 July 1998.

4.2.3 Detailed run 3. July 98

It is winter, and balloons were launched under VERY tough conditions, with extremely high wind and low temperature.

Few remarks:

- Once again, there is a surprising agreement between both experiments. Fig. 4.11 4.12 and 4.13 show about the same level of turbulence at about the same altitude.
- In winter is encountered the worst contribution of the high altitude layers.
- Here again, there are low altitude layers, between 4 and 5km.
- One can notice the strong 18km layer in Fig. 4.12, which corresponds to a steep decrease of the wind from 25 to 0 m/s, in Fig. 4.10.

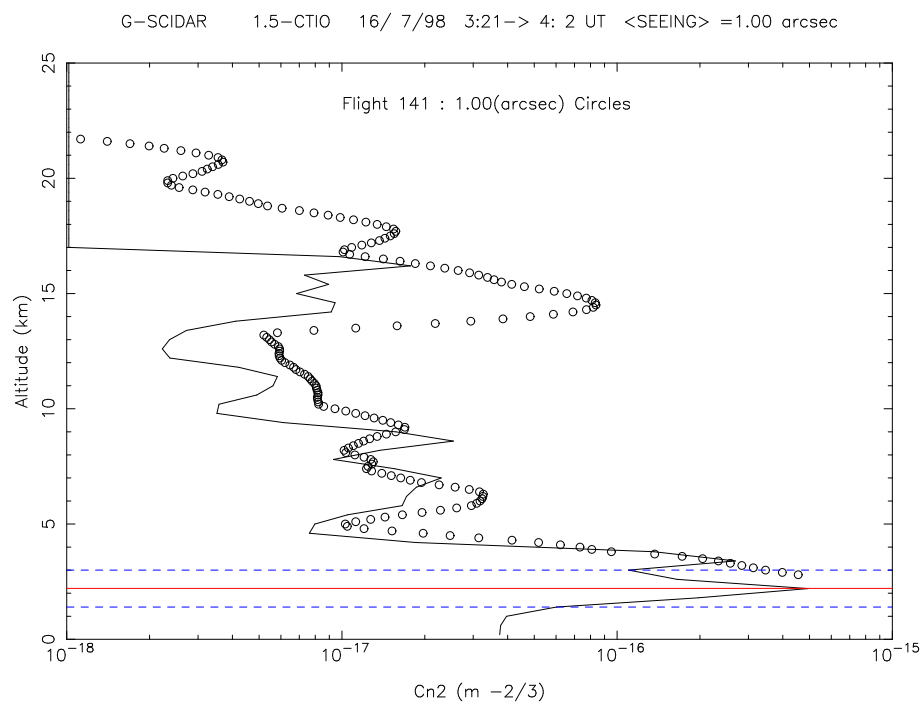


FIGURE 4.11: Comparison G-Scidar/Balloon on 16 Jul 98.

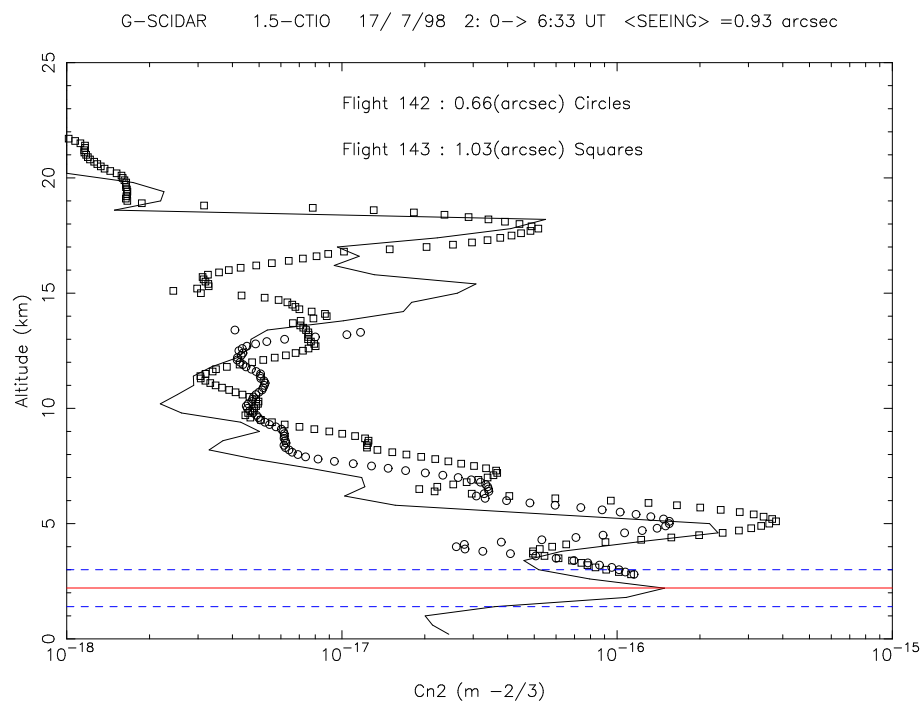


FIGURE 4.12: Comparison G-Scidar/Balloon on 17 Jul 98.

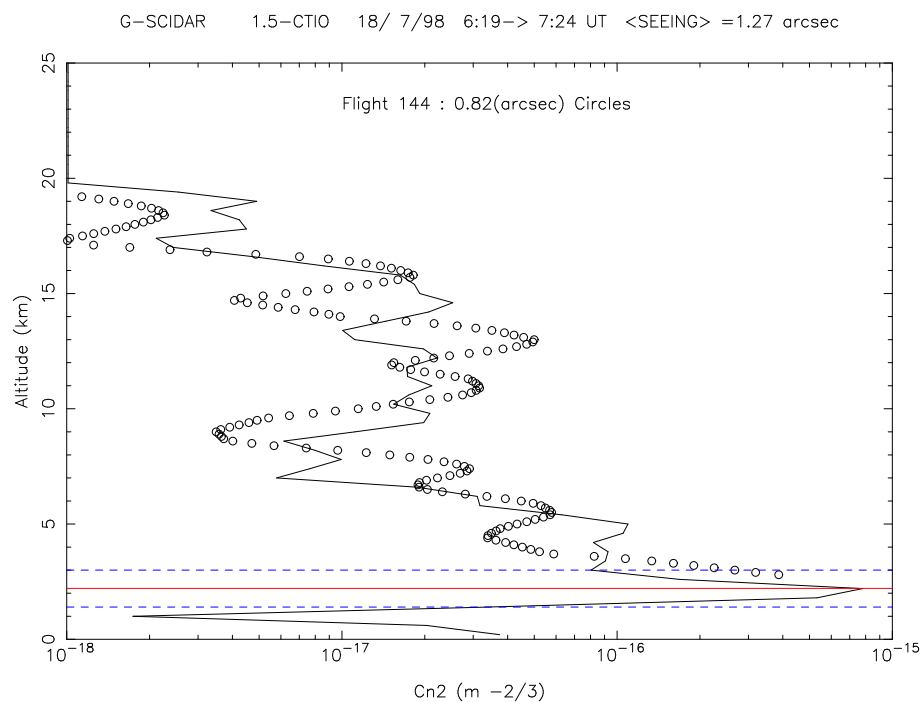


FIGURE 4.13: Comparison G-Scidar/Balloon on 18 Jul 98.

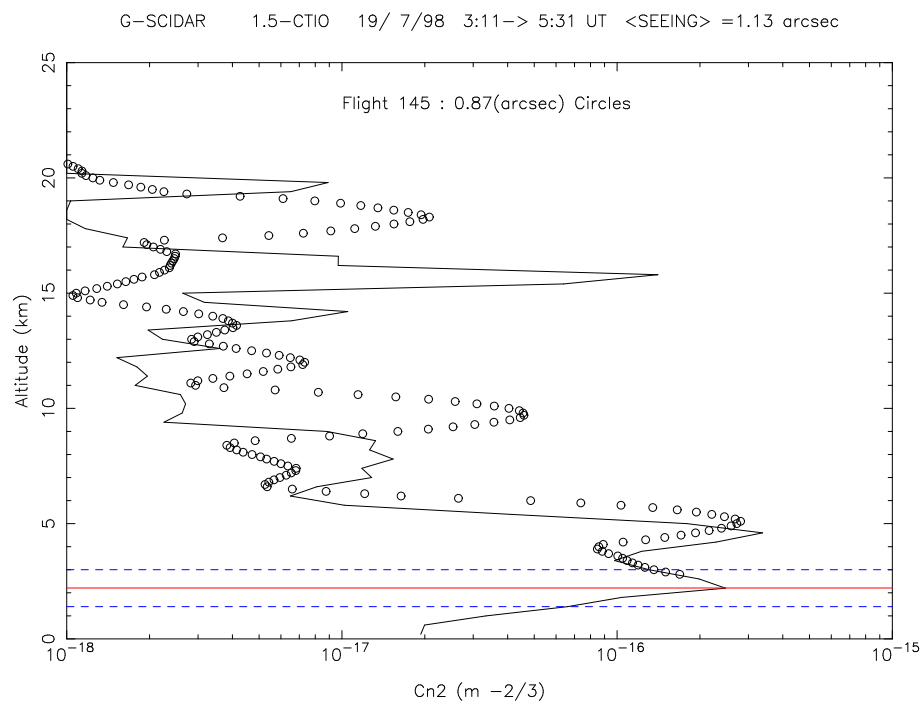


FIGURE 4.14: Comparison G-Scidar/Balloon on 19 Jul 98.

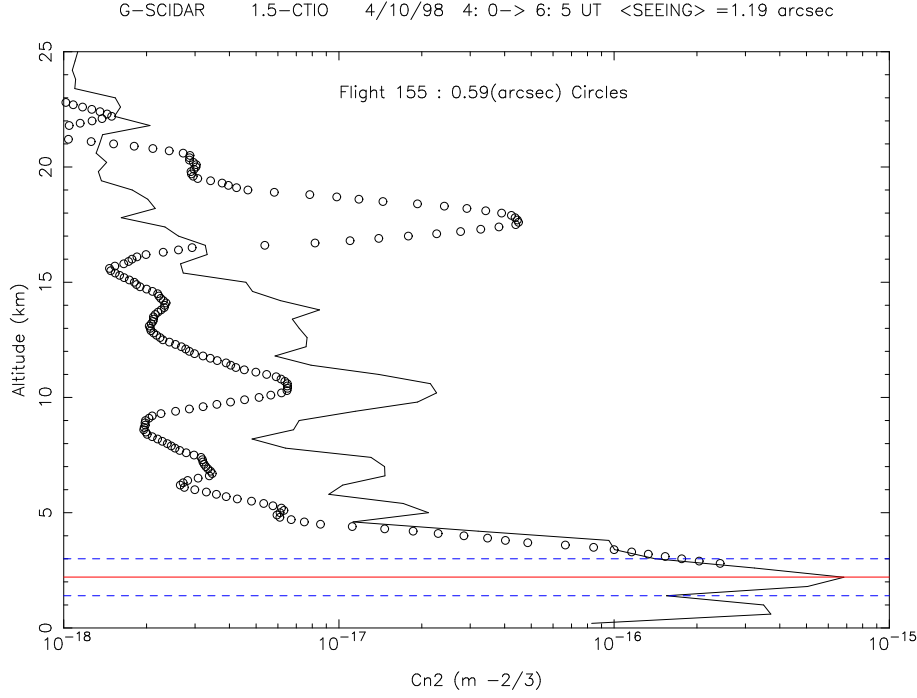


FIGURE 4.15: Comparison G-Scidar/Balloon on 4 Oct 98.

4.2.4 Detailed run 4. October 98

During this last run, agreement between Scidar and balloon is worse.

- In Fig 4.15 the 17km layer is not detected by the Scidar.
- In Fig 4.16 the agreement is satisfactory up to 15km where much more *in situ* turbulence is detected.
- In Fig 4.17 the agreement is very good, with very low high altitude turbulence.
- In Fig 4.18 the agreement is very good, unless the 5km layer is not present in the Scidar profile.
- In Fig 4.21 the 4 km layer agrees perfectly with both experiments.

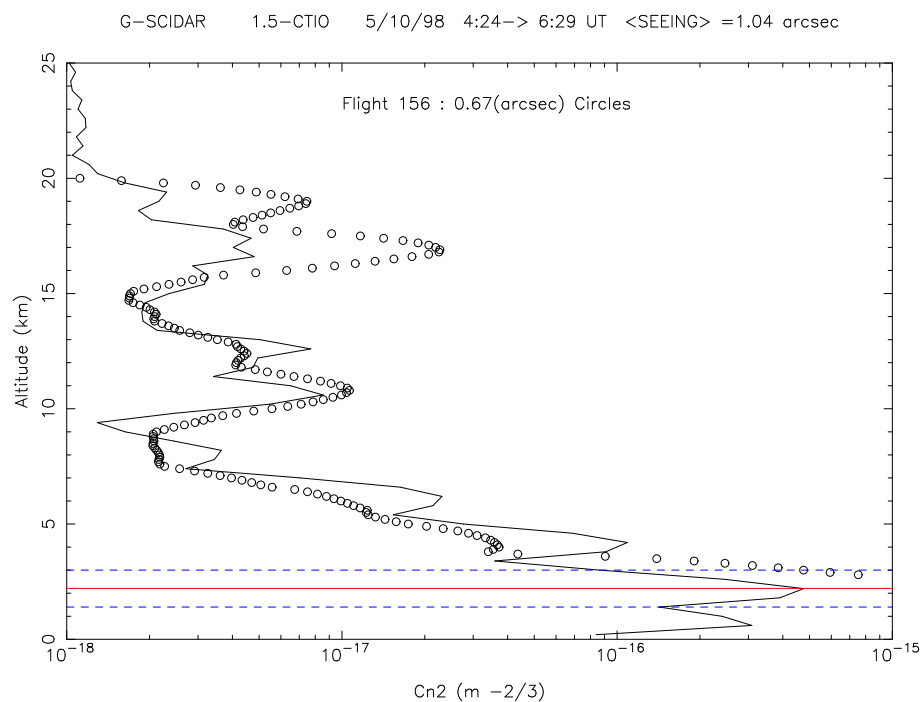


FIGURE 4.16: Comparison G-Scidar/Balloon on 5 Oct 98.

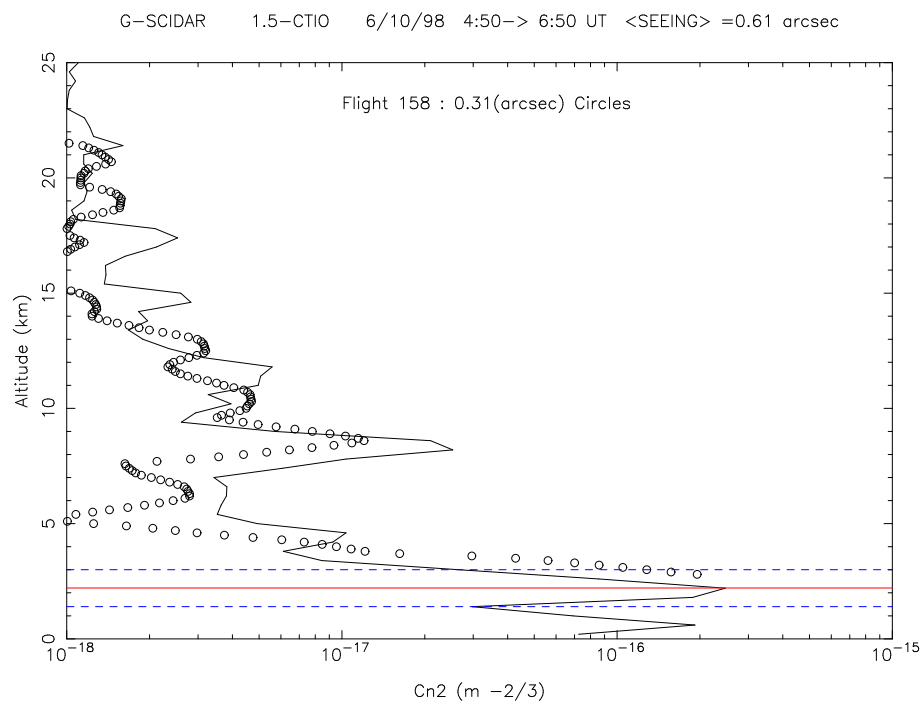


FIGURE 4.17: Comparison G-Scidar/Balloon on 6 Oct 98.

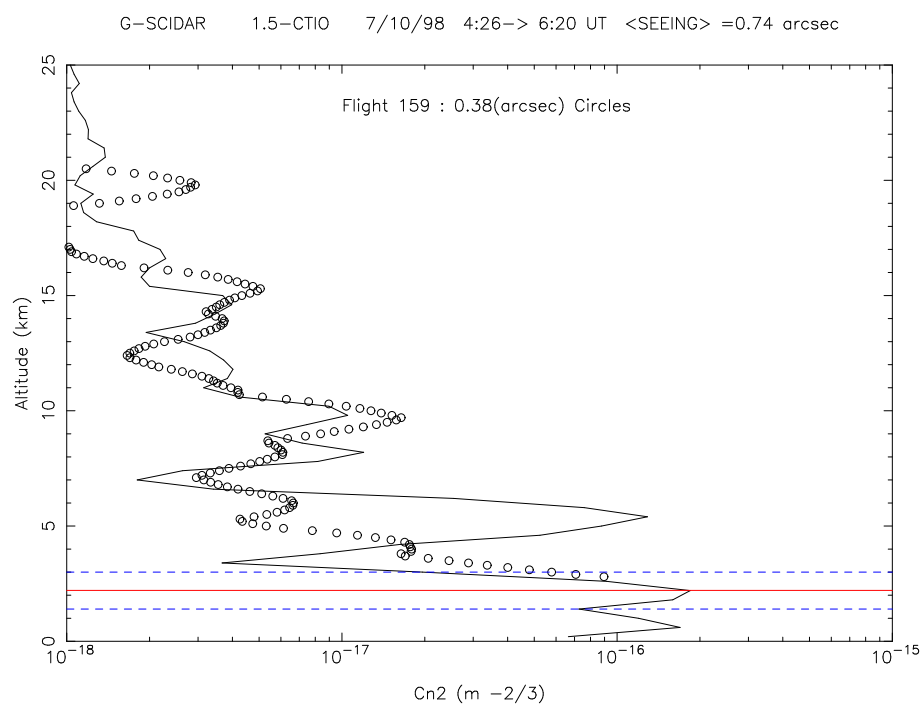


FIGURE 4.18: Comparison G-Scidar/Balloon on 7 Oct 98.

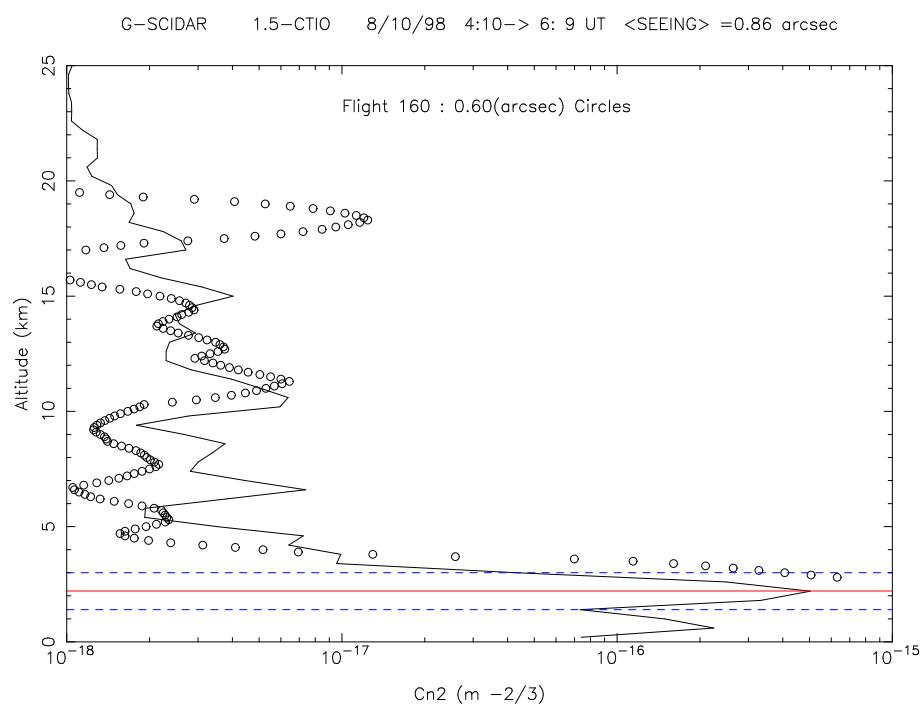


FIGURE 4.19: Comparison G-Scidar/Balloon on 8 Oct 98.

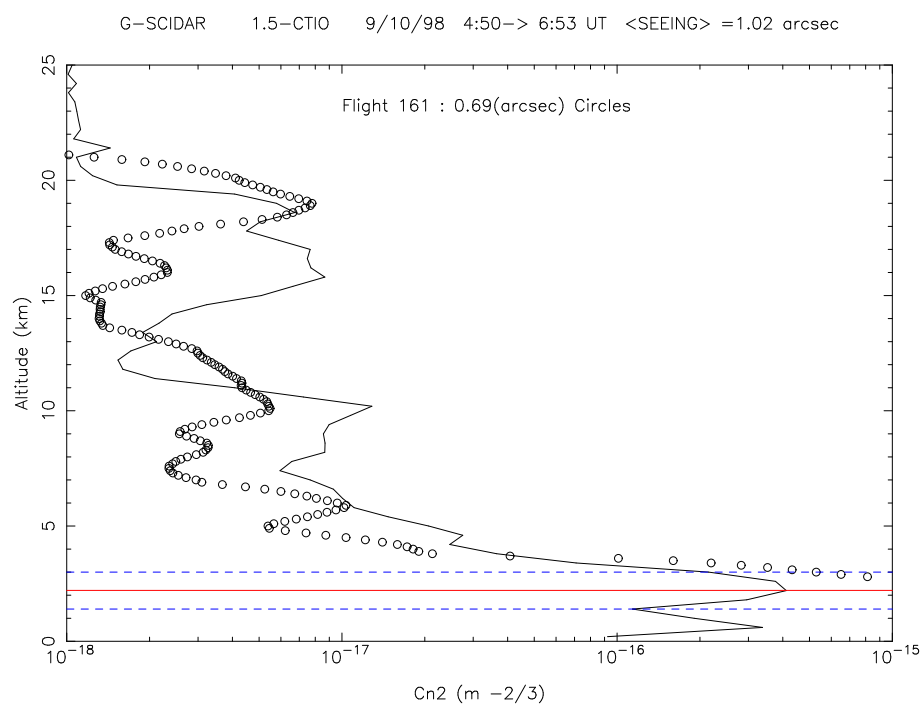


FIGURE 4.20: Comparison G-Scidar/Balloon on 9 Oct 98.

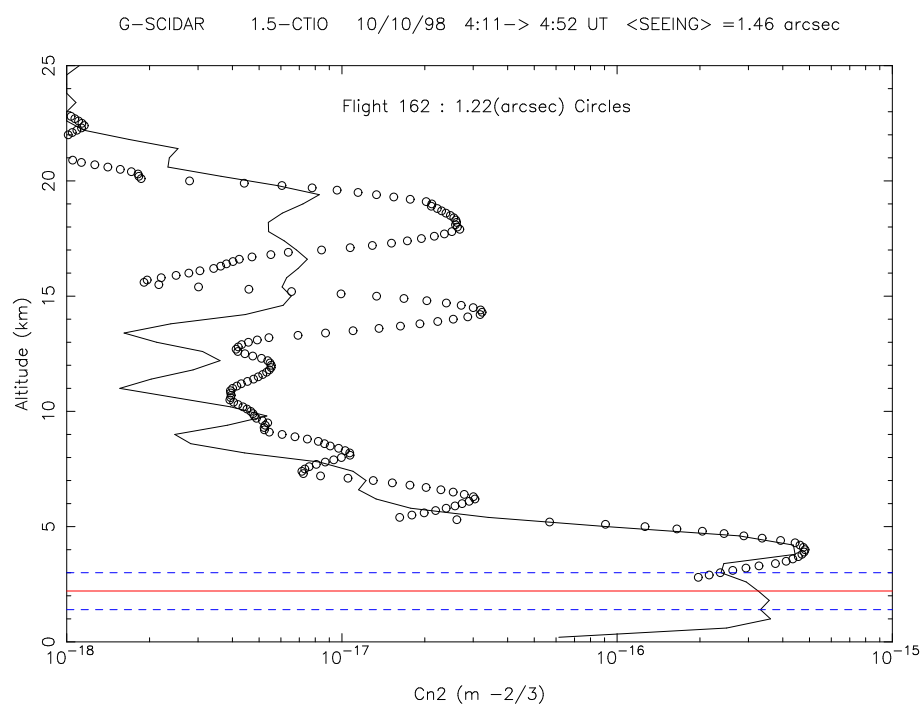


FIGURE 4.21: Comparison G-Scidar/Balloon on 10 Oct 98.

4.2.5 Summary of each run and whole year

Here we present a comparison between averaged GS and Balloon profiles over each four runs, from Fig. 4.22 to 4.25.

Finally, in Fig. 4.26 is shown the comparison of all ths Scidar measurements and all the balloon flights.

One can remark a very good agreement, especially in Figs 4.22, 4.24, 4.25 and 4.26. Except in Fig. 4.24, balloon detects more high altitude turbulence (17–19km) than the Scidar. This can be attributed to Andes perturbation appearing more East, which might be encountered by the balloon going generally eastward, and less by the Scidar.

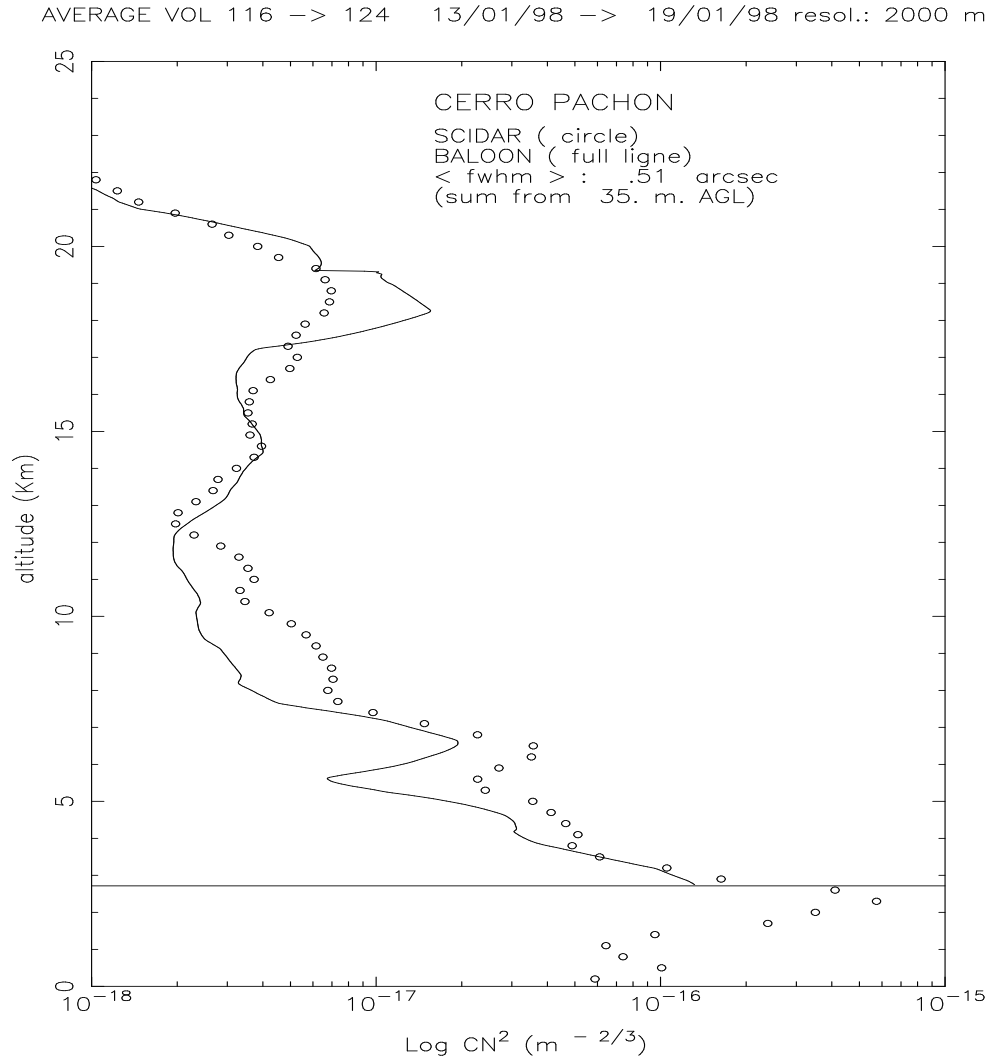


FIGURE 4.22: Comparison G-Scidar/Balloon over first run.

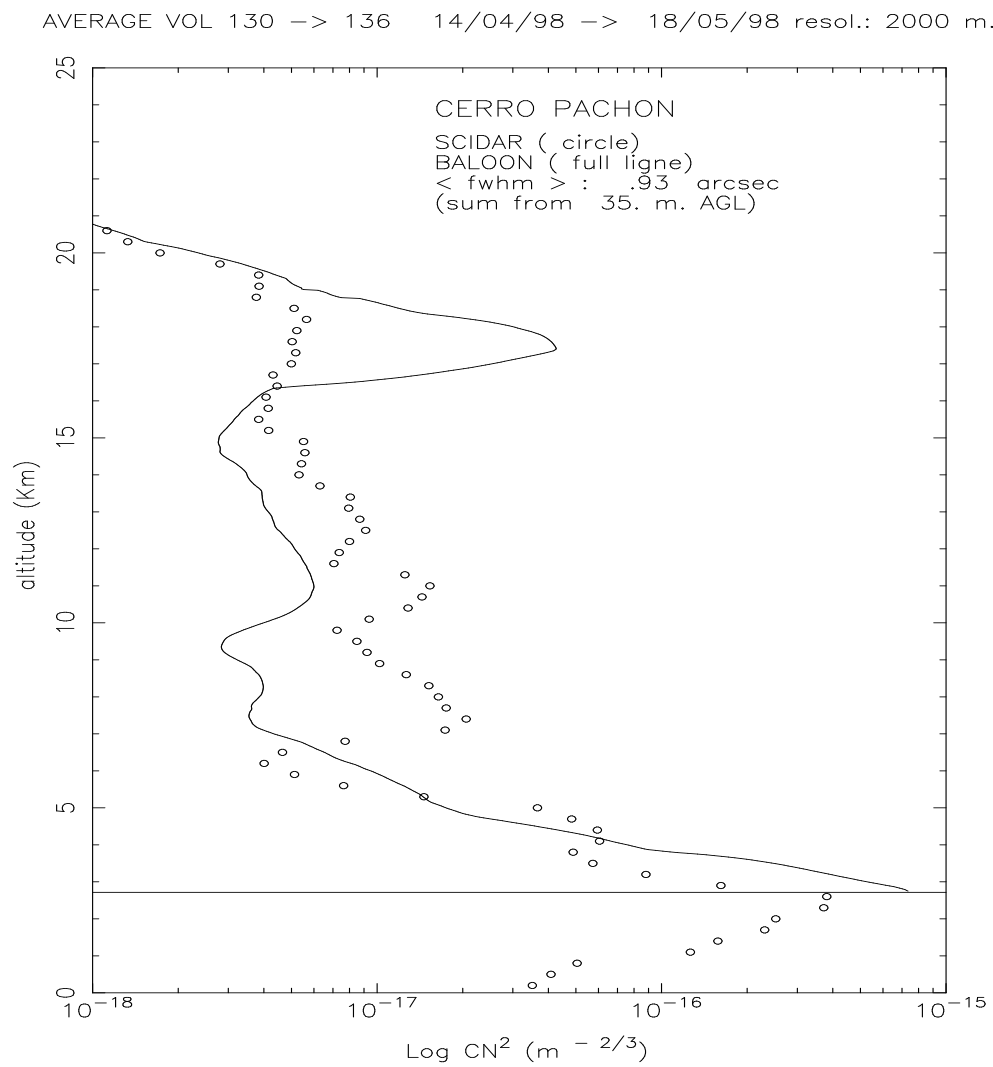


FIGURE 4.23: Comparison G-Scidar/Balloon over second run.

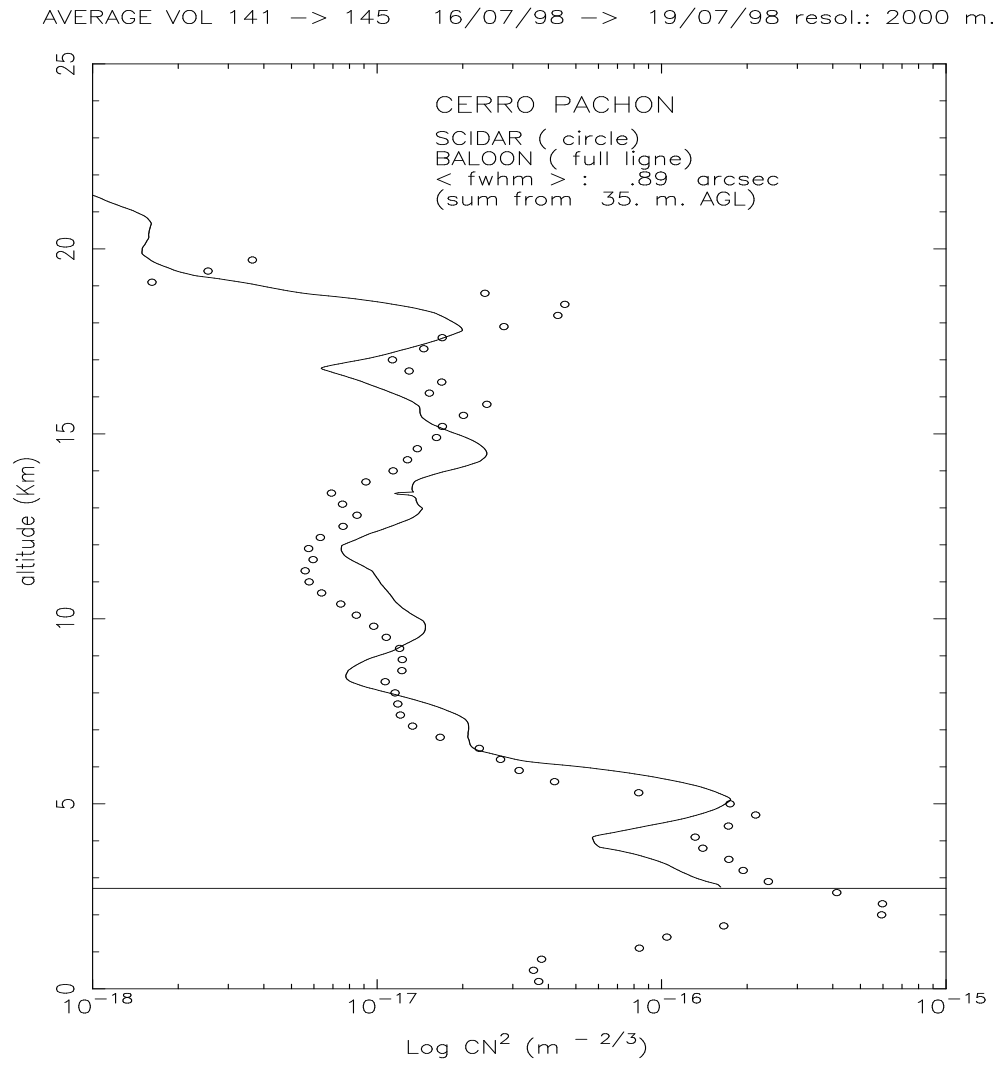


FIGURE 4.24: Comparison G-Scidar/Balloon over third run.

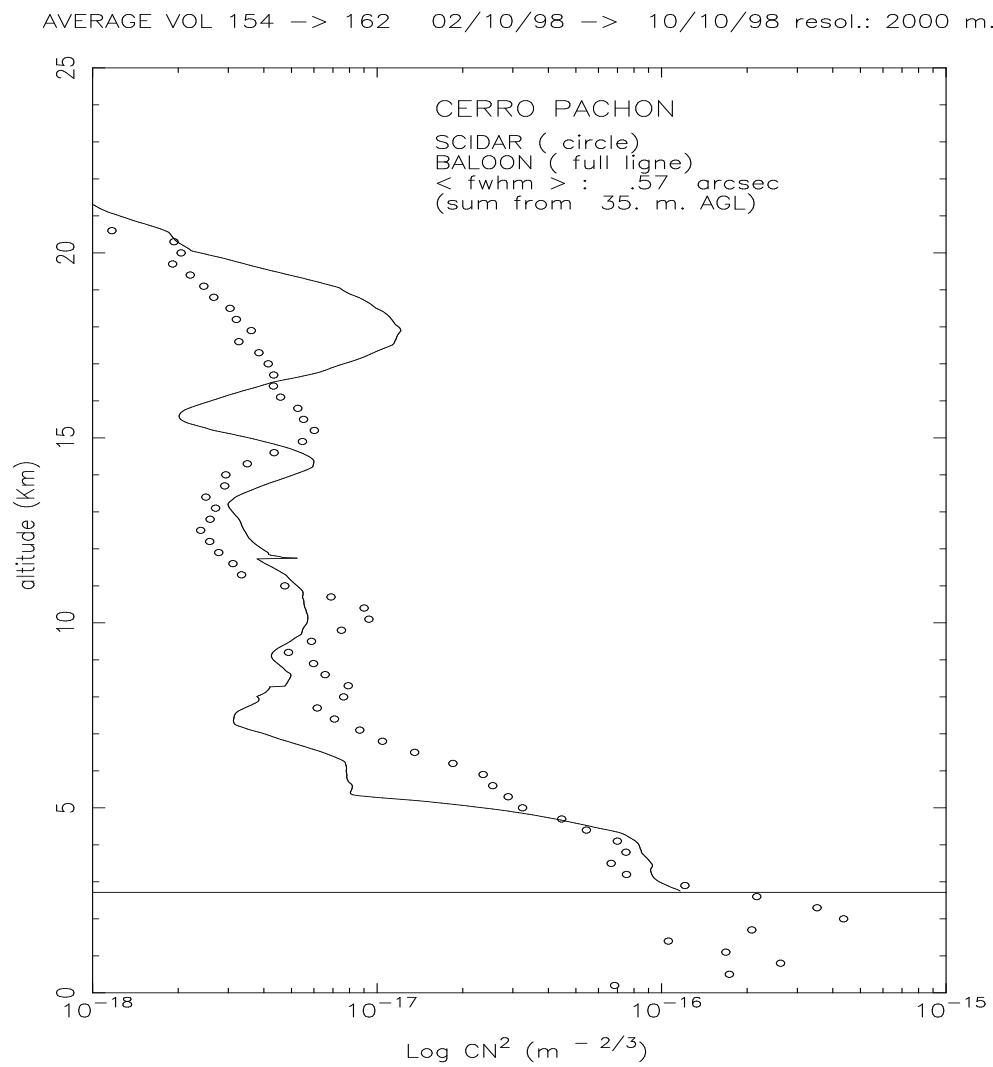


FIGURE 4.25: Comparison G-Scidar/Balloon over fourth run.

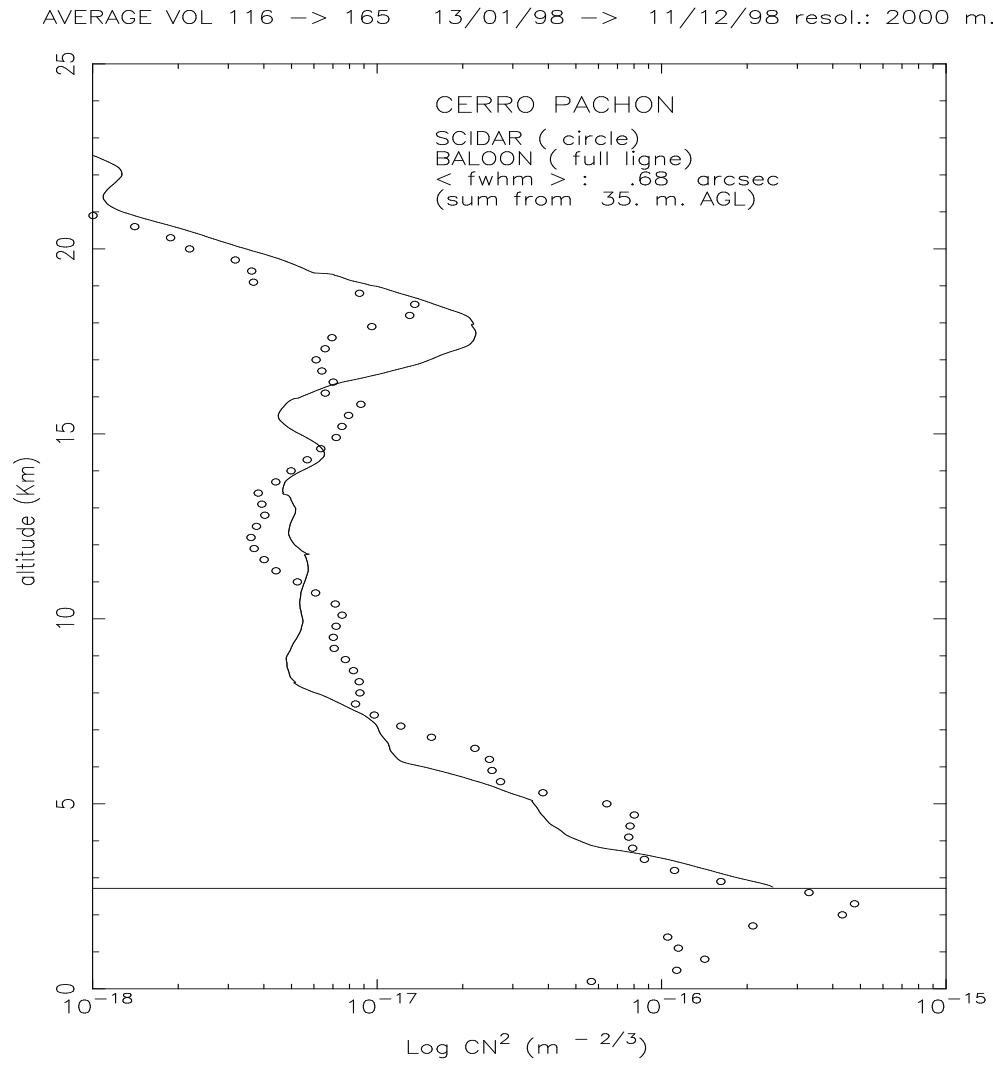


FIGURE 4.26: Comparison G-Scidar/Balloon over the whole year.

TABLE 4.5: Comparison between G-Scidar and balloon technique ($h > 20m$) for integrated variables, on a night by night analysis. Adaptive optics case.

Date	Fl.	ε	ε	θ_{AO}	θ_{AO}	τ_{AO}	τ_{AO}	v_{AO}	v_{AO}
		GS	Bal	GS	Bal	GS	Bal	GS	Bal
13/01	116/7	0.55	.38/.32	2.9	2.1/4.0	9.9	5.8/8.6	4.2	14.2/11.2
14/01	118	0.69	.53	1.5	1.1	2.4	3.7	14.4	16.2
15/01	119	0.67	.41	2.9	2.5	10.7	5.3	4.1	14.5
16/01	120	0.86	.89	2.6	2.6	9.9	6.1	3.5	5.8
17/01	121	0.88	.60	1.9	2.0	7.3	7.5	3.3	7.0
18/01	123	0.66	.37	2.6	2.9	16.1	10.6	2.4	8.1
19/01	124	0.95	.75	1.6	1.4	4.3	3.1	7.3	13.5
15/04	132/3	0.88	.72/1.82	2.1	1.6/1.1	2.9		9.3	
16/04	134/5	0.72	.77/.52	1.9	1.8/2.6	4.1		7.1	
16/07	141	1.00	1.02	2.0	1.0	1.9	1.1	12.8	27.7
17/07	142/3	1.10	.68/1.06	1.0	3.4/1.2	1.7	1.5/1.0	14.7	32./29.
18/07	144	1.54	0.71	1.4	1.4	2.3	2.3	5.7	19.2
19/07	145	1.64	0.88	1.2	1.5	1.4	1.7	11.6	21.8
20/07		0.80		1.8		2.6		11.6	21.8
21/07		1.14		1.2		1.1		19.5	
03/10		0.76		2.5		3.3		8.2	
04/10	155	0.69	0.49	2.5	1.5	3.7	4.5	6.9	14.6
05/10	156	0.69	0.50	2.9	1.7	4.8	5.0	5.5	12.6
06/10	158	0.51	0.27	3.4	3.4	9.0	11.8	2.3	10.0
07/10	159	0.65	0.32	2.4	3.0	4.6	7.1	5.5	13.7
08/10	160	0.57	0.39	3.6	2.5	6.5	6.5	4.2	12.7
09/10	161	0.67	0.55	2.1	2.4	2.3	3.5	10.6	16.5
10/10	162	1.13	1.26	1.6	1.3	2.7	1.6	7.4	16.2

4.3 G-Scidar/Balloon integrated parameters: θ, τ

We present here two tables. In Table 4.5 and 4.6 is given the comparison between G-Scidar and balloon on a night by night basis, for adaptive optics and speckle interferometry. and in Table 4.7 on a run by run basis and over the entire campaign.

In next Table 4.7 is presented a résumé of the previous tables, but averaged over each four runs, and, at last, over the whole campaign.

- **Seeing:** It is visible that the G-Scidar technique find more optical turbulence than the balloon technique. Four reasons might be imagined:

1. **Ground boundary:** G-Scidar and balloon do not begin the C_n^2 integral from the same lower boundary: $I_{G-Scidar} = \int_{0_{Tololo}}$ and $I_{Balloon} = \int_{20m_{Pachn}}$.

TABLE 4.6: Comparison between G-Scidar and balloon technique ($h > 20m$) for integrated variables, on a night by night analysis. Speckle interferometry case.

Date	Fl.	ε	ε	θ_{SI}	θ_{SI}	τ_{SI}	τ_{SI}	v_{SI}	v_{SI}
		GS	Bal	GS	Bal	GS	Bal	GS	Bal
13/01	116/7	0.55	.38/.32	3.1	3.2/4.7	10.8	8.1/10.3	4.8	11.9/11.2
14/01	118	0.69	.53	2.2	2.0	2.8	6.1	13.0	11.3
15/01	119	0.67	.41	3.4	3.8	11.2	9.2	4.4	9.8
16/01	120	0.86	.89	2.8	2.7	12.5	6.6	3.0	6.2
17/01	121	0.88	.60	2.1	2.3	8.8	8.1	3.2	7.5
18/01	123	0.66	.37	2.9	3.4	17.4	13.7	2.5	7.2
19/01	124	0.95	.75	2.0	2.0	5.3	5.3	6.7	9.2
15/04	132/3	0.88	.72/1.82	2.3	1.1/1.9	2.9		9.3	
16/04	134/5	0.72	.77/.52	2.5	2.5/3.6	4.1		7.1	
16/07	141	1.00	1.02	2.3	1.3	2.9	1.9	9.5	18.9
17/07	142/3	1.10	.68/1.06	1.5	6.1/1.7	2.7	3.0/2.1	10.4	17.9/16.5
18/07	144	1.54	0.71	1.6	2.4	3.7	2.8	4.2	18.8
19/07	145	1.64	0.88	1.5	2.2	2.3	2.6	8.2	16.4
20/07		0.80		2.5		3.2		11.2	
21/07		1.14		1.6		2.7		9.4	
03/10		0.76		3.0		4.6		6.6	
04/10	155	0.69	0.49	3.1	2.3	4.4	6.0	6.7	12.5
05/10	156	0.69	0.50	3.4	2.5	5.6	7.8	5.2	9.3
06/10	158	0.51	0.27	4.1	4.9	9.9	15.8	2.4	8.6
07/10	159	0.65	0.32	3.5	4.6	5.5	10.0	5.5	11.3
08/10	160	0.57	0.39	3.9	3.2	6.7	7.6	4.6	12.6
09/10	161	0.67	0.55	2.6	2.7	3.1	5.6	9.1	12.1
10/10	162	1.26	1.26	1.9	1.5	3.5	2.6	6.7	11.3

2. **Theoretical calibration:** The G-Scidar is self-calibrated because it measures a dimensionless flux $I / \langle I \rangle$, but is model dependant throughout its Kernel (see 1.18).
3. **Experimental calibration:** Balloon data rely on a coefficient linking temperature and resistor variations in the Wolfram thread, and, as explained above, on the Kolmogorov turbulence theory.
4. **Different places:** Of course, Pachón and Tololo are not at the place, and there is a 500m altitude difference, which can account for this seeing difference.

This campaign was so expensive, that we can tranquilize the tax payer saying that we made our best to use the best turbulence theory along with the most expensive thermistor wire! Which is not true, because Wolfram is much cheaper than gold, but is much more solid and have a much better temperature- Ω

TABLE 4.7: Résumé of each G-Scidar integrated variables compared with the balloons for $h > 20m$, for each run and for the whole campaign. Normal Dome seeing processing (D).

Run	ε	ε	θ_{AO}	θ_{AO}	τ_{AO}	τ_{AO}	θ_{SI}	θ_{SI}	τ_{SI}	τ_{SI}
Instr.	GS	Bal	GS	Bal	GS	Bal	GS	Bal	GS	Bal
01 Jan	0.80	0.53	2.1	2.3	8.2	6.3	2.5	3.0	9.3	8.4
02 Apr	0.76	0.96	2.0	1.8	3.9		2.5	2.3	5.1	
03 Jul	1.22	0.87	1.4	1.7	1.8	1.5	1.8	2.7	2.8	2.5
04 Oct	0.72	0.54	2.5	2.3	4.2	5.7	3.1	3.1	5.0	7.9
All	0.85	0.67	2.1	2.1	4.6	4.9	2.6	2.9	5.6	6.8

coefficient!

Non-simultaneity in space and time is also an “old” argument which has been used since decades to explain atmospheric-related discrepancies! Again, we think that the overall good agreement between both techniques, which seems obvious from all the plots and tables, leads to the conclusion that seeing at Pachón is expected to be better than at Tololo.

- Adaptive optics and speckle interferometry techniques: Conditions at both sites look like to be very similar, with a weak advantage to Pachón site.

4.4 G-Scidar/GSM/Balloon comparison during last run, October 1998

In Table 4.8 is given the comparison of integrated variables between the three instruments, G-Scidar, GSM and balloon. It appears that GSM account for the highest optical turbulence, and the wider isoplanatic angle since it was installed at 3m above the ground.

TABLE 4.8: Résumé of each G-Scidar integrated variables compared with the balloons for $h > 20m$, for each run and for the whole campaign. Dome seeing processing (D).

Run	ε	ε	ε	θ_{AO}	θ_{AO}	θ_{AO}
Instr.	GS	GSM	Bal	GS	GSM	Bal
04/10	0.69	0.83	0.49	2.5	2.8	1.5
05/10	0.69	0.88	0.50	2.9	2.8	1.7
06/10	0.51	0.59	0.27	3.4	3.8	3.4
07/10	0.65	0.75	0.32	2.4	2.9	3.0
08/10	0.57	0.74	0.39	3.6	4.1	2.5
09/10	0.67	0.91	0.55	2.1	2.1	2.4
04 Oct	0.72	0.98	0.54	2.5	2.9	2.3

Chapter 5

CONCLUSION

We will here comment the overall campaign putting emphasis on the instruments which have been used and summarize, on a qualitative basis, the main scientific results. It is not our intention to compare Cerro Pachón site with other main observatories, since it is the first time that such an amount of site-testing results have been accumulated during such a long period. To our knowledge, only Cerro Paranal, La Silla and Roque de los Muchachos have been thoroughly investigated for what concern the seeing. Then many other places were analysed with deeper insight, using Scidar, G-Scidar, G.S.M, balloons, mast, insolately, or together, but for a short period of time, of the order of one or two weeks. Among these sites we can cite the above mentioned sites and South Pole, Mauna Kea, Mount Locke, San Pedro Mártir, Izaña.

5.1 Instruments: methods, coherence, reliability

- **Coherence.** First of all, one notices the overall good coherence between all our instruments which have been settled at Cerro Pachón and Cerro Tololo: Generalized Scidar, generalized seeing monitor, balloons and mast. This is a proof that our equipment is now mature and give quantitative measurements. All along this report, optical turbulence profiles and integrated variables have been cross-checked with success. Few rapid comparisons between velocities given by G-Scidar fit well with velocity of the wind speed issued by the meteorological balloons. The relatively short distance between those two site is not an argument to prove an eventual discrepancy in the measures. More, we have proven that low altitude layer appearing in the 3 to 6km range exist above both sites.
- **Reliability.** No entire night has been lost for a failure occuring either with the G-Scidar or G.S.M. At the begining of each run we had to re-install our equipment, make some optical adjustment during a short period of time, one or two hours. Very few payloads were lost, due to technical failure, or due to bad launching conditions. We recall that, especialy during winter, launchings were decided, even with low temperature and strong wind (more than 15m/s). This comfort us in our launching procedure.

- **Database.** To our knowledge, it is the first time that such a long campaign, with such an amount of instruments took place. Throughout 50 balloons, only 5 were lost, mainly during July and August. 29 nights were allocated at the 1.5m telescope, from which we observed during 22 nights, the other being lost due to bad weather. Almost 7000 C_n^2 profiles have been given by the G-Scidar, and more than 600 estimations of the outer scale of turbulence by the G.S.M. All these informations are stored on magnetic medias, raw measurements as well as processed data, tables, postscript plots and this report.

Most of the data have been analysed, but the comparison between \mathcal{L}_0 deduced from G.S.M and balloon is to be done, as well as the processing of wind detection with the G-Scidar analysing the scintillation of a single star.

A huge investment were devoted to develop new programs to assess the wind velocity in each turbulent layer, analysing the spatio-angular-temporal evolution of the scintillation of a double star, leading to a large database of wind/ C_n^2 profiles which has never been obtained before. A large amount of code was written to process and compare the processed data each one with the other.

5.2 Scientific conclusions

Most of the scientific conclusions are commented and detailed in figures and tables of last chapter 4, and will not be commented again. They gave a whole set of quantitative measures of $C_n^2(h)$ and $\mathbf{V}(h)$ profiles as well as major parameters for adaptive optics and interferometry such as ε , r_0 , θ , τ , d_0 , h_{opt} .

- **Horizontal extension.** It is particularly clear that optical turbulent layers span over the two observatories, as visible, for exemple, in Fig. 4.7 and 4.12. Most of the layers were detected between 3 to 7km and around 19km. Their horizontal extension might be larger than the distance between the two sites since the balloon, during its ascent, is blown away toward Andes.

To have a better insight on the origin of these layers, the only way would be to use a numerical predicting meteorological model, as shown by Masciadri et al., 1999. It could be verified that those layers are generated by gravity waves triggered by the wind general circulation over the orography.

- **Winter high altitude strong layers.** For exemple, in Figs 4.11, 4.12 and 4.15 one notices the presence of high altitude layers with strong contribution to optical turbulence. This is a very bad situation for adaptive optics, since it lowers the isoplanatic angle and the coherence time, due to the fact that high altitude layers propagates at more rapid velocities.
- **Dome seeing at the 1.5m.** In Table 4.2 is shown that the dome participate for a little bit less than one third of the overall seeing at the focus of the 1.5m telescope. With the data in our possession, it is not possible to know why the dome seeing is minimum in winter time.

- **Seeing at Pachón.** From Table 4.7, and if we assume, as already noticed, that G–Scidar and balloons are well calibrated, one can hope that the seeing at Pachón, 0.67", will be better than the seeing at Tololo, 0.85", on average. This is not a small gain, when one bears in mind that the limiting flux, in speckle interferometry, follows the expression:

$$\Phi_{lim} \propto \frac{\varepsilon^n}{D^m} \quad (5.1)$$

with $2 \leq n \leq 4$ and $0 \leq m \leq 1$, depending upon the interferometry technique, as explained in Vernin and Muñoz, 1992.

In Tables 3.6 and 3.7 one notices that balloon–seeing can be as low as 0.3", the isoplanatic angle more than 3", the coherence time larger than 10ms and finally the water vapor content lower than 1mm.

- **Seasonal effect.** For most of the integrated variables, summer is the best season, except for the 1.5m dome seeing which seems to be better during winter.
- **Dynamical range.** In Table 4.4 integrated variables span over a wide dynamical range, which makes complicate to fix an optimum for field of view, time exposure and light–wave bandwidth for adaptive optics and interferometry. For exemple, if one takes a conservative exposure time of 1ms, he would miss the oppotunity to enlarge it by a factor of 15 which corresponds approximately to a gain of 3 magnitudes! **Thus, the permanent presence of a G–Scidar seems mandatory to monitor the main integrated variables for adaptive optics and interferometry.**
- **Summary of the AO results.** In last Table 5.1 is given the average of the main parameters relevant to Adaptive Optics and Speckle Interferometry, for the entire campaign, instrument by instrument.

TABLE 5.1: Résumé of mean parameters for entire campaign, at Cerro Tololo and Cerro Pachón, 1998. “n.a” means “not available” with this instrument, “n.c” means “not calculated”. For subscripts N, D and A, see discussion in section 1.3.2. Balloon data have been integrated above 20m, corresponding to Gemini mirror height above the ground. Scintillation given by the GSM is affected by pupil averaging ($D = 10\text{cm}$). GSM was operated only during the last run in October.

	GS_N	GS_D	GS_A	<i>Balloon</i>	<i>GSM</i>
Seeing(arcsec)	1.06	0.85	0.89	0.67	0.83
$\theta_{AO}(\text{arcsec})$	2.1	2.1	2.1	2.1	2.8
$\theta_{SI}(\text{arcsec})$	2.3	2.6	2.5	2.9	n.a
$\tau_{AO}(\text{ms})$	n.a	4.8	5.4	4.9	n.a
$\tau_{SI}(\text{ms})$	n.a	5.7	6.2	6.8	n.a
$d_0(\text{m})$	3.8	3.7	3.8	n.c	n.a
$h_{opt}(\text{km})$	1.8	2.7	2.5	n.c	n.a
$\mathcal{L}_0(\text{m})$	n.a	n.a	n.a	n.c	36
<i>Scintillation (%)</i>	17.5	17.3	17.2	15.7	1.9

5.3 Acknowledgments

All this work would never have been possible without the help of the **staff** of Tololo Observatory, during the daytime, as well as during nighttime. One needs to know that we had to coordinate the balloon launching with Scidar measurement and communicate with the Airplane Traffic control in Santiago airport. We express our thanks to Marc Chun for his implication in all the phases of this site testing campaign, from carrying the crates to correcting this report, from launching balloons to climbing on top of the mast, for his infinite patience with the “french connection”. We are indebted with the skills and professionalism of Pablo Blayer and Bernhard Lopez, from the *Departamento de Geofísica de la Universidad de Santiago de Chile* who launched many balloons “*au péril de leur vie*”. Many thanks are dedicated to Malcolm Smith, Director of CTIO, for his unconditional help. We acknowledge E. Gizard and the french *Centre National de la Recherche Météorologique* for the complimentary operation and loan of their balloon tracking system. Finally we are indebted to Doug Simon who trusted in our skills to plan this site testing campaign to its end.

Chapter 6

BIBLIOGRAPHY

Bibliography

- [1949] OBUKHOV A.M "Structure of the temperature field in turbulent flow", Izv. Akad. Nauk SSSR, Ser. Geogra. Geophys, 13, 58
- [1949] YAGLOM A.M, Dan. SSSR, 69, 743
- [1961] TATARSKI, V. I. *Wave propagation in a turbulent medium* traduit du russe, Dover Publications
- [1966] FRIED, D.L. "Optical resolution through a random inhomogeneous medium for very long and very short exposures" J. Opt. Soc. Am. **56**, 1372
- [1974] BARLETTI R., CEPPATELLI G., MORODER E., PATERNO L., RIGHINI A. "Vertical profile of turbulence in the Atlantic air mass measured by balloon borne radiosonde", J. Geophys, 79, 4545–4549
- [1974] ROCCA A., RODDIER F., VERNIN J. "Detection of atmospheric turbulent layers by spatiotemporal and spatioangular correlation measurements of stellar-light scintillation" J. Opt. Soc. Am. **64**, 1000
- [1979] LOOS G.C, C.B. HOGGE, "Turbulence of the upper atmosphere and isoplanetism", Applied Optics, V. 18, 2654-2661.
- [1981] RODDIER, F. "The effects of atmospheric turbulence in optical astronomy" in Progress in Optics (ed E.Wolf) **XIX**, 281 (1981)
- [1982] RODDIER, F. GILLI, J.M. LUND, G. "On the origin of speckle boiling and its effects in stellar speckle interferometry" J. Optics **13**, 263
- [1982] RODDIER, F. GILLI J.M. VERNIN, J. "On the isoplanatic patch size in stellar speckle interferometry" J. Optics **13**, 63
- [1983] VERNIN J. , AZOUIT, M. "Traitement d'image adapté au speckle atmosphérique.II Analyse multidimensionnelle appliquée au diagnostic à distance de la turbulence" J.Optics(Paris), 14,131–142
- [1985] COULMAN, C., "Fundamental and applied aspects of astronomical seeing" Ann. Rev. Astron. Astrophys., 23,19
- [1987] CACCIA JL, AZOUIT M., Vernin J. Wind and C_N^2 profiling by single-star scintillation analysis Appl. Opt. **26**, 1288

- [1988] COULMAN C. et al., *Appl. Opt.*, 27, 155
- [1990] CACCIA J.L, VERNIN J. Wind fluctuation measurements in the buoyancy range by stellar scintillation analysis" *J. Geoph. Res.* **95**, 13683
- [1991] VERNIN J., WEIGELT G., CACCIA J.L and MULLER M. "Speckle life time and isoplanicity determinations: Direct measurements and derivation from turbulence and wind profiles", *A&A*, 243,553–558
- [1992] VERNIN, J. and MUNOZ–TUNON, C. "Optical seeing at La Palma Observatory. I-General guidelines and preliminary results at the Nordic Optical Telescope" *Astron. & Astrophys.* 257, 811-816
- [1992] VERNIN, J. "Atmospheric turbulence profiles" in *Wave propagation in random media (scintillation)* Univ. of Washington, Seattle, USA. SPIE and Inst. of Physics publishing, Bristol and Philadelphia.
- [1993] ZIAD A., "Estimation des échelles limites de cohérence spatiale des fronts d'onde et Optimisation des observations à Haute résolution Angulaire en Astronomie". Thesis, Nice University.
- [1994] VERNIN, J. and MUNOZ–TUNON C. "Optical seeing at La Palma Observatory. II Intensive site testing campaign at the Nordic Optical Telescope" *A&A*, 284, 311–318
- [1994] MARTIN F., TOKOVININ A., AGABI A., BORGNINO J., ZIAD A., *Astron. Astrophys. Suppl. Ser.*, V. 108, p. 1.
- [1995] FUCHS A., VERNIN J., TALLON M. "Laboratory simulation of a trubulent layer – Optical and in situ characterization" *Appl. Opt.*, 35, 1751–1755
- [1995] Lloyd–Hart et al., *ApJ*, 439, 455
- [1996] MARTIN F., BORGNINO J., ZIAD A., AGABI A., AVILA R., Tokovinin A., Grating Scale Monitor (GSM)." Un moniteur des paramètres de la turbulence intervenant en HRA tout particulièrement dédiée à la mesure de l'échelle externe de cohérence spatiale des fronts d'onde".(ESO Report).
- [1997] AVILA R., VERNIN J., MASCIADRI E. "Whole atmosphere turbulence profiling with generalized scidar" *Appl. Opt.*, 36, 7898–7905
- [1997] AVILA R., ZIAD A., MARTIN F., AGABI A., TOKOVININ A., "Theoretic spatiotemporal analysis of angle of arrival induced by atmospheric turbulence as observed with the grating scale monitor experiment" *J. Opt. Soc. Amer.*, V. A14, p. 3037.
- [1998] AVILA R., VERNIN J., CUEVAS S., "Turbulence profile with generalized scidar at San Pedro Mártir Observatory and isoplanatism studies", *P.A.S.P.*, 110, 1106–1116

-
- [1999] MASCIADRI E., VERNIN J., BOUGEAULT P., "3D mapping of optical turbulence using an atmospheric numerical model. I A useful tool for the ground based astronomy", A & A Suppl. Ser., 137, 185–202
- [1999] MASCIADRI E., VERNIN J., BOUGEAULT P., "3D mapping of optical turbulence using an atmospheric numerical model. II First results at Cerro Paranal", A & A Suppl. Ser., 137, 203–216